Study of Gas Flow Dynamics in Porous and Granular Media with Laser-Polarized ^{129}Xe NMR

by

Ruopeng Wang

Submitted to the Department of Nuclear Science and Engineering
in partial fulfillment of the requirements for the degree of
Doctor of Philosophy
at the
MASSACHUSETTS INSTITUTE OF TECHNOLOGY
February 2005

Author . . . .
Department of Nuclear Science and Engineering
Feb 1, 2005

Certified by . . . .
Ronald L. Walsworth
Senior Lecturer, Harvard-Smithsonian Center for Astrophysics
Thesis Supervisor

Certified by . . . .
David G. Cory
Professor, Department of Nuclear Science and Engineering, M.I.T.
Thesis Supervisor

Read by . . . .
Donald Candela
Professor, Department of Physics, University of Massachusetts
Thesis Reader

Read by . . . .
Alan P. Jasanoff
Associate Professor, Department of Nuclear Science and Engineering,
M.I.T.
Thesis Reader

Accepted by . . . .
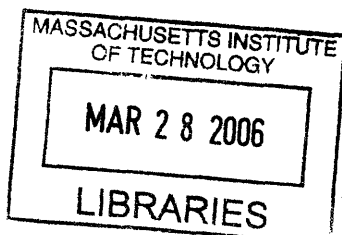Jeffrey A. Coderre
Associate Professor, Department of Nuclear Science and Engineering,
Chairman, Department Committee on Graduate Students

Study of Gas Flow Dynamics in Porous and Granular Media with Laser-Polarized ^{129}Xe NMR

by

Ruopeng Wang

Abstract

This thesis presents Nuclear Magnetic Resonance (NMR) studies of gas flow dynamics in porous and granular media by using laser-polarized ^{129}Xe. Two different physical processes, the gas transport in porous rock cores and the mass exchanges between different phases in fluidized granular systems, were investigated and new experimental methods were designed to measure several important parameters characterizing the two systems. Methods for measuring the parameters had been either unavailable or significantly limited previously. The research involved modeling the gas flow in porous and granular media by relating the dynamics of spin magnetization to the interesting parameters, as well as correspondingly designing new measurement methods and verifying them on the laboratory test beds.

We proposed a simple method to measure two important parameters of reservoir rocks, permeability and effective porosity, by probing the flow front of laser-polarized xenon gas inside the rock cores. The method was thoroughly tested on different categories of rocks with permeability values spanning two orders of magnitude, and the results were in agreement with those from the established techniques. The uniqueness in the work is that the fast method developed is capable of measuring the two parameters simultaneously on the same setup.

Bubble-emulsion exchange and emulsion-adsorption exchange in a fluidized bed are two processes crucial to the efficiency of many chemical reactors working in bubbling regime. We used differences in T_2 and chemical shift to contrast the three phases in the xenon spectra, and designed methods to measure the inter-phase exchange rates. The measured results of the bubble-emulsion and emulsion-adsorption exchange rates agreed well with predictions based on available theory. Our approach is the first to non-invasively probe natural bubbles in a three-dimensional bed, and to measure the exchange rate between the emulsion phase and multiple bubbles.

Thesis Supervisor: Ronald L. Walsworth
Title: Senior Lecturer, Harvard-Smithsonian Center for Astrophysics

Thesis Supervisor: David G. Cory
Title: Professor, Department of Nuclear Science and Engineering, M.I.T.

Acknowledgments

This thesis would not have come into being without the help from the many colleagues and friends during my recent acdemeic years. I want to take this chance to express my deep gratitude to those who helped me.

First I want to thank my thesis supervisor, Ronald Walsworth, for his support, guide and encoragement. He provided me an excellent research environment, left me enough freedom to do things the way I thought they should be done, and was always available to discuss ideas and problems. I am very grateful for the opportunity to have learned from and worked with him. Thank also goes to my advisor, David Cory, who has been an excellent mentor providing me insightful directions and the discussions with him have always been very helpful. I thank Ross Mair for his patience and commitment in teaching me every aspect of NMR technology and guiding me through the scientific practices. I owe a debt of gratitude to Matthew Rosen, who has spent lots of time in helping design and build parts essential for the fluidized bed experiments, and also in proofreading this thesis. I am fortunate to have an outstanding colaborator and montor, Donald Candela at UMass. I offer my appreciation to him for the useful discussion and guide in the field of fluidized granular media.

I also want to thank Tina Pavlin for the discussions on my research and the helpful comments on my thesis draft. John Ng has been a friend and colleage great to work with, and generously helped in running the experiments, as well as proofreading my thesis. Leo Tsai and Mason Klein have lent me great ideas and experimental apparatus from their work on vibro-fluidized bed. I am also indebted to David Phillips and Glenn Wong for their help and inspiring guidance.

Finally I want to acknowledge the support and love from my family. The encoragement and understanding across the ocean from my parents has been crucial for my completion of Ph.D. My wife Qing deserve my deepest thanks, for all that she has done for me during these years. The accomplishment belongs to both of us.

Contents

---

[1]This chapter is based on the material published in *Phys. Rev. E* **70** 026312 (2004)

List of Figures

11

12

13

14

15

16

17

18

List of Tables

Chapter 1

Introduction

This thesis describes the application of Nuclear Magnetic Resonance (NMR) techniques to laser-polarized noble gases in order to study the dynamics of fluid flow in porous and granular media. The results quantify several important parameters in the two types of systems, revealing important structural and hydrodynamic information. Porous and granular media are ubiquitous in nature, pharmaceuticals, as well as industrial fields such as oil-drilling and food processing. The complex fluid flow through porous and granular media brings about many theoretically and experimentally challenging problems, with difficulties arising from the random arrangements and opaque nature of the solid phase; and the large number of degrees of freedom which make simulation difficult. Research on these materials has fundamental significance in both physical and chemical sciences, in addition to its contributions to the improvements of wide-ranging engineering practices.

The research concentrated on experimental investigations of the physical processes by using gas-phase NMR. NMR has become a powerful, non-invasive probe of non-metallic materials. The deep penetration of radio frequency energy (RF) into these materials, which contain nuclear spins capable of resonant absorptions and emissions at specific frequencies in the presence of an external magnetic field, permits this study of materials in different physical and chemical states. The resultant signals are rich with information relevant to different fields of study, and the technology has spread from physics to chemistry, material research, bioscience and clinical diagnosis.

Researchers continue to expand the scope of NMR to new fields and applications.

Gas-phase NMR has traditionally suffered from poor signal-to-noise ratio, mostly due to the low spin density of gases. The development of the spin-exchange optical pumping technique, which enhances the spin polarization of certain noble gases by up to 5 orders of magnitude, can provide gas-phase spin magnetization comparable to that of the liquid phase in magnetic fields ~ 1 T. The pumping process involves the indirect transfer of photon polarization to the nuclear spins of the noble gas species, and is most efficient in ^{129}Xe and ^{3}He, which have a nuclear spin number of $\frac{1}{2}$. The laser-polarization technique, first pioneered in 1950's [3], has matured and platforms capable of delivering large volumes of laser-polarized gas are now available. We developed a home-built polarization system for polarizing natural-abundance xenon and providing a continuous flow of laser-polarized gas into the NMR samples located in the NMR magnet.

Chapter 2 summerizes the basics of the NMR technique. Starting with a description of the quantum-mechanical picture of a single nuclear spin in the presence of a magnetic field, the chapter lists important aspects of NMR experiments, including chemical shifts, magnetic susceptibility and nuclear relaxation phenomena - due to the interactions of the spin system with its environment, as well as among the spins themselves. This chapter also covers two established applications of NMR, in which the spatial density maps of a material and information about the dynamic displacement of spins are obtained.

Chapter 3 covers both the principles underlying the spin-exchange optical pumping process and the specifics in applying NMR techniques to laser-polarized noble gases. The two stages of transferring photon polarization to nuclear spins are discussed, together with primary measures for optimizing the pumping efficiency. This chapter also explains differences between laser-polarized noble gas NMR and its conventional thermally-spin-polarized counterpart, followed by several examples demonstrating special modifications necessary in such experiments.

In Chapter 4, the methodology and experimental details for simultaneously measuring gas permeability and effective porosity of reservoir rocks are described. We

introduce these two important parameters, which characterize the fluid transport processes in porous media; relate the flow properties to each parameter based on the fluid dynamics describing flow in porous media; present the experimental schemes and measurement results; and compare the results to those available from established methods.

Chapters 5 through 7 present the model, experiments, results, and relevant discussions on experimental studies of gas dynamics in a gas-fluidized bed.

Chapter 5 introduces the basic aspects of a system of gas-fluidized granular particles and covers the definition and importance of the exchange behavior in such a system. The first half of this chapter describes the different fluidization regimes, the classification of particles, and two distinct exchange behaviors. In addition, the chapter discusses in detail a model governing the dynamics of different phases in terms of nuclear spin magnetizations, providing a context for the experiment design and data analysis.

Chapter 6 details the measurement of gas exchange rates experimentally by using specifically designed NMR methods. The description of the experimental apparatus includes the design of the fluidized bed setup, choice of particles and design of the RF probe. Also discussed are the methods used to obtain contrast between different phases in the fluidized bed, as well as the NMR pulse sequences designed to perform the measurement. This chapter concludes by presenting the experimental data and the measurement results.

Chapter 7 re-evaluates the assumptions made in building the experimental model for the fluidized-bed study by using the quantitative estimations and actual experimental results. This chapter also covers the significance of this research in the context of the granular media field, together with the universality and limitations of the method.

Chapter 2

Nuclear Magnetic Resonance

2.1 Introduction

Nuclear magnetic resonance (NMR) has been one of the most successful technologies in modern science. The beauty of NMR lies in the fact that it is sensitive to spins hosted by nuclei of size 10^{-15} m, and is able to effectively manipulate these spins to yield a wide variety of information. The dynamics of a single nuclear spin are affected by the spin's local magnetic field, which is generated by a combination of effects from nearby nuclei, electrons, or external magnets. The resultant NMR signals are rich with structural and dynamical information on molecules or atoms in objects ranging in size from a rock pore or biological cell up to human brains. In only a few decades of development, this technology has spread from physics, to chemistry, to material research, bioscience and clinical diagnosis [4].

Researchers are still extending the technology to dramatically different new fields such as implementation of quantum computation, soft-matter physics, and cellular metabolism.

2.2 History

In 1945, the magnetic resonance phenomenon was first observed by two independent groups, led by Ed Purcell (Harvard University) and Felix Bloch (Stanford Univer-

sity), who shared the Nobel Prize in physics in 1950. The availability of commercial magnets in the late 1950's significantly promoted development of both NMR theory and technology. The year 1966 saw a major breakthrough, when Richard Ernst discovered that the sensitivity of spectra could be enhanced $\sim$ 100 fold if the slow frequency sweep was replaced by intense radiofrequency (RF) pulses. He went further to introduce the Fourier Transform into data analysis, from which different frequency components were immediately separable. This revolutionary work, along with seminal developments in two-dimensional NMR spectroscopy, earned him the Nobel Prize for chemistry in 1991. In the decades after 1970, the improvements in super-conducting magnets and concurrent advances of computer technology lead to the rapid development of experimental techniques involving multiple frequency dimensions. Another milestone in the history of magnetic resonance technology occurred in 1973, with the application of a linear field gradient to generate frequency encoding with spatial dependence, which opened the door for the enormously successful magnetic resonance imaging technologies, now known as MRI. Paul Lauterbur and Peter Mansfield shared the 2003 Nobel Prize in Physiology or Medicine for their original work in the building foundations for MRI.

2.3   Spin Dynamics

Spin is an intrinsic quantum-mechanical property of a nucleus, and its measure is determined by the number of protons and neutrons existing in each nucleus. The majority of NMR studies utilize spin-1/2 nuclei because of the ease in manipulation, observation and analysis. The magnetic moment $\vec{\mu}$ of a nucleus is proportional to its spin $\vec{J}$ by

$$\vec{\mu} = \gamma \vec{J}, \tag{2.1}$$

where γ is the gyromagnetic ratio of the nucleus. Table 2.1 lists properties of several nuclear species commonly used.

NMR technology has been mostly applied in the liquid or soft-condensed matter

28

Table 2.1: Properties of Selected Spin-$\frac{1}{2}$ Nuclei

Isotope	Lamor Frequency (MHz/T)	Natural Abundance (%)	Magnetic Moment (μ_N)
^{1}H	42.577	99.984	2.79270
^{3}He	32.434	1.3×10^{-4}	-2.1274
^{13}C	10.705	1.108	0.70216
^{129}Xe	11.78	26.24	-0.7726

phase, with ^{1}H being the most common "working nucleus", as it is ubiquitously found in aqueous, organic and biological samples. Being gaseous at room temperature, ^{3}He and ^{129}Xe were not favored as candidates since they contributed very low NMR signal intensity due to their significantly lower spin density. However, gas-phase NMR studies on these species are made possible by laser-polarizing, or enhancing the spin polarization of the gas beforehand. Additionally, Xe atoms have a large electron cloud which easily deforms and interacts with other atoms. As a result, ^{129}Xe spins are very sensitive to their chemical environment, and a chemical shift range as large as 300 ppm has been observed [5, 6]. Different ^{129}Xe resonances have hence been used to label different chemical or physical states in the study of transport and exchange behavior [7, 8].

When a single spin-1/2 nucleus is placed in a static magnetic field B_0, the Hamiltonian describing the Zeeman interaction between the spin and field is

$$H = -\vec{\mu} \cdot \vec{B}_0 = \mu_z B_0, \qquad (2.2)$$

if we use a laboratory coordinate frame such that the z-axis is along the applied magnetic field direction. The interaction breaks the nuclear energy-level degeneracy for I_z, and the Hamiltonian H results in two levels $\pm \gamma \hbar B_0 / 2$, dependent on whether the spin is parallel ($I_z = \hbar/2$) or anti-parallel ($I_z = -\hbar/2$) to the B_0 direction. The energy difference between the two levels is $\gamma \hbar B_0$, with lower energy in $\hbar/2$ state. The resonance or transition frequency ω between the two levels, also known as the Larmor

frequency, is

$$\omega = \gamma B_0. \qquad (2.3)$$

and the equation of motion for the spin state is given by the Schrödinger equation

$$-i\hbar \frac{\partial |\psi\rangle}{\partial t} = H|\psi\rangle. \qquad (2.4)$$

In practice, we always look at a sample with a large number (10^{19}) of spins of the same species, each of which may occupy different states. The system may be conveniently described if we introduce the density matrix

$$\rho = \sum_{\psi} p_{\psi} |\psi\rangle \langle \psi|, \qquad (2.5)$$

where $|\psi\rangle$ is one of the spin states, which are usually chosen to be the eigenstates of Hamiltonian given in Eqn. (2.2). p_{ψ} is the probability of finding a spin in the state $|\psi\rangle$. Measurement of spin on the system yields an ensemble average $\sum_{\psi} p_{\psi} \langle \psi | \vec{J} | \psi \rangle$ or simply $Tr(\rho \vec{J})$. The dynamics of the density matrix follows Liouville equation

$$i\hbar \frac{\partial \rho}{\partial t} = [H, \rho]. \qquad (2.6)$$

The equation of motion for an ensemble average with magnetic moment $\vec{\mu}$ is then given by

$$\frac{\partial \langle \vec{\mu} \rangle}{\partial t} = \frac{1}{i\hbar} Tr([H, \rho]\vec{\mu}) = \frac{\gamma}{i\hbar} Tr(\rho[\vec{J}, H]) = \gamma^2 B_0 \langle \vec{J} \rangle \times \hat{z} = \langle \vec{\mu} \rangle \times \gamma \vec{B}_0. \qquad (2.7)$$

This is equivalent to the classical description for the movement of a magnetic moment in an external field [9]. Therefore, it is justified to treat the spin ensemble classically, if we ignore the interaction between the spins, which is not included in Eqn. (2.2) [10]. The ensemble average of the magnet moment may be simply depicted as a vector, with its time-dependence given by Eqn. (2.7).

Under thermal equilibrium, the spin populations on the two energy levels are determined by Boltzmann distribution

$$n_\pm = \frac{e^{\pm \frac{\gamma B_0 \hbar}{2kT}}}{e^{\frac{\gamma B_0 \hbar}{2kT}} + e^{-\frac{\gamma B_0 \hbar}{2kT}}}, \tag{2.8}$$

and the spin polarization of the system is

$$p = n_+ - n_- = \frac{e^{\frac{\gamma B_0 \hbar}{2kT}} - e^{-\frac{\gamma B_0 \hbar}{2kT}}}{e^{\frac{\gamma B_0 \hbar}{2kT}} + e^{-\frac{\gamma B_0 \hbar}{2kT}}}. \tag{2.9}$$

Typically the energy splitting is much smaller than the thermal energy ($\frac{\gamma B_0 \hbar}{2kT} = 1.6 \times 10^{-5}$ for $B_0 = 4.7$ T and at room temperature); hence $p \approx \frac{\gamma B_0 \hbar}{2kT}$ is a good approximation under most circumstances. The nuclear magnetization in a sample placed in an external field B_0 is defined as the total net magnetic moment per unit volume, or the single spin moment multiplied by the polarization and atom number density N:

$$M_0 = \frac{\hbar}{2}\gamma p N = \frac{\gamma^2 \hbar^2 N B_0}{4kT}. \tag{2.10}$$

This is the magnetization along the B_0 field direction at thermal equilibrium, and is also the state of the spin system where all liquid and solid-phase magnetic resonance experiments start. Magnetization at any other instant is given by $\vec{M} = N\langle \vec{\mu} \rangle$, and its time-dependence is governed by the famous Bloch equation [11],

$$\frac{d\vec{M}}{dt} = \gamma \vec{M} \times \vec{B}_0 - \frac{M_z - M_0}{T_1}\hat{z} - \frac{M_x \hat{x} + M_y \hat{y}}{T_2}. \tag{2.11}$$

T_1 and T_2 are included to phenomenologically account for longitudinal and transverse spin relaxations respectively.

2.4 Relaxation

Assuming a homogeneous externally-applied field B_0, relaxation of an ensemble's spin polarization is caused by local magnetic fields experienced by the nuclear spins,

which arise from interactions between the spins and their surrounding environments, including electrons and other nuclei, in the form of dipolar or other higher order interactions. Due to random motions, the local field is not static, but rather undergoes large fluctuations in both magnitude and orientation. Typical examples of these motions include rotation and translation of molecules that bind the nuclei together. Not only the strength but also the rate of the fluctuations significantly affect the spin behavior, which manifests itself as the relaxation parameters: the longitudinal and transverse relaxation rates.

2.4.1 Longitudinal Relaxation T_1

Suppose a spin ensemble, or NMR sample, is originally placed at zero field. The net magnetization is zero because there is no energy split and the spins assume no preference in their orientation. If a magnetic field $\vec{B}_0$ is turned on at $t = 0$ and Zeeman split generated, the nuclear spins tend to be rotated towards an equilibrium Boltzmann distribution of populations. The process for the system to reach equilibrium, in which the spin populations satisfy Eqn. (2.8), is called the longitudinal relaxation. If the relaxation of spin magnetization follows a single exponential curve, we designate its time constant as T_1. Longitudinal relaxation is also referred to as spin-lattice or spin-polarization relaxation, as the process involves energy exchange between the spins and their surrounding thermal environment.

T_1 relaxation is the result of spins reversing (flipping) their orientation, with absorption or emission of an amount of energy equal to $\gamma \hbar B_0$, the energy difference between the two Zeeman levels. This corresponds to a frequency value of $\omega_0 = \gamma B_0$, or the Larmor frequency. If the fluctuation frequency of a local magnetic field has a frequency component at ω_0, then this local field contributes to the longitudinal relaxation. The larger the magnitude of field fluctuations at ω_0, the shorter the T_1 relaxation time.

T_1 is measured by observing the return of the spin system to equilibrium after it is initially disturbed by an RF pulse. As an example, we next describe the inversion-recovery method for measuring T_1. A 180° RF pulse may be used to invert the

spin magnetization from $+z$ direction (equilibrium state) to $-z$ direction. The effect of T_1 relaxation is to gradually restore magnetization M to $+z$ direction, with a time-dependence given by $M = M_0(1 - 2\exp(-t/T_1))$ where M_0 is the magnitude of magnetization at thermal equilibrium. After a delay time t following the 180° pulse, M is measured by flipping the spins onto the transverse plane with a 90° pulse and then acquiring the free induction decay (FID). Multiple such measurements are needed with different lengths of the delay time t, in order to get complete information on the time-dependence of magnetization, from which T_1 value is available by fitting the data to an exponential.

2.4.2   Transverse Relaxation T_2

It is routine to rotate spin magnetization from the longitudinal direction onto the transverse plane, to initiate an NMR experiment. These spins start with the same phase and undergo coherent Larmor precession, but dephase gradually because the spin-spin interactions result in different local magnetic fields for different spins, even in a perfectly homogenous external field. Phase coherence is lost over the characteristic timescale T_2 and the transverse magnetization diminish to zero. Various names have been used to refer to this phenomenon: transverse relaxation, decoherence spin-spin relaxation and T_2 relaxation.

In a heterogeneous external magnetic field, such as that due to susceptibility contrast between different materials or an intentionally applied imaging gradients, the decay time constant for the transverse magnetization is shorter than T_2 and is known as T_2^*. The spin-echo is a powerful NMR technique invented to regain spin coherence lost due to invariant external field inhomogeneities, by applying an appropriately timed phase-inverting 180° RF pulse [12]. The Carr-Purcell sequence extends this idea by using multiple 180° pulses, and the resultant echo train forms an envelope that decays with the time constant T_2. Spin dephasing caused by T_2 relaxation is inherently random and cannot be refocused with RF pulses[1], which is

---

[1]This applies to interactions between "like" spins of the same nuclear species. It is possible to refocus coherence loss due to invariant interactions between different types of nuclear spins.

Table 2.2: Different Types of Relaxation Mechanisms

Relaxation Mechanism	Description
Dipole-Dipole Relaxation	Interaction of the spin with the magnetic field generated by another nearby nuclear spin. Most popular for spin 1/2 nuclei.
Quadrupolar Relaxation	Relaxation due to the asymmetric electric field around a quadrupolar nucleus, usually from a spin of half integer but larger than 1. e.g. ^{27}Al, ^{59}Co.
Chemical Shift Anisotropy	The value of chemical shift varies as a function of molecule orientation with respect to $\vec{B}_0$ field. e.g. ^{31}P and solid state samples.
Paramagnetic Relaxation	The large fluctuating field generated by unpaired electrons in paramagnetic materials, such as Gd^{2+}.
Spin Rotation Relaxation	Coupling of spin and angular momentum in a bi-molecule collision. Usually occurs in gas-phase systems.
Scalar Relaxation	Interaction between two nuclei mediated by electrons, also called J-coupling.

usually called homogeneous broadening of the NMR spectrum, while inhomogeneous broadening refers to recoverable (T_2^*) coherence loss.

2.4.3 Relaxation Mechanisms and Quantum-Mechanical Results

Spin relaxation originates from spatially varying local fields, modulated by molecular motions. Many different types of interactions can lead to these field variations, and hence to spin relaxation. Different relaxation mechanisms are listed in Table 2.2.

Of all the relaxation mechanisms, dipole-dipole relaxation is the most important in liquid state NMR with spin-1/2 nuclei.

The relaxation problem can be treated quantum-mechanically by solving the Liouville equation (2.6) describing the dynamics of the density matrix for the spin system. The Hamiltonian of the system is the Zeeman energy plus interaction terms, which is typically decomposed into a superposition of spin operators with time-dependent
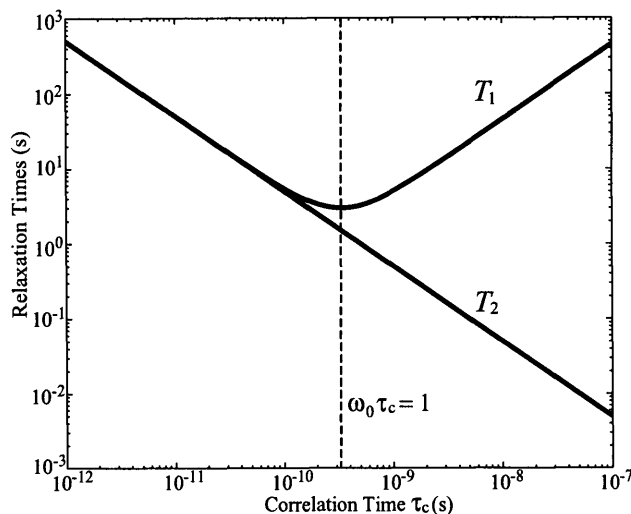
Figure 2-1: Dependence of relaxation times on correlation time τ_c. Two different motion regimes are identified.

prefactors $F(t)$ that describe the molecular rotational and translational motions. The time-varying modulations are best described by the spectral density function, $J(\omega)$, the Fourier transform of the auto-correlation function of $F(t)$, which describes the intensity of the motion-modulated interactions in the frequency domain. For the dipole-dipole interactions in a spin-1/2 system, the calculated relaxation rates are linearly related to values of $J(\omega)$ at discrete frequencies [13]:

$$\frac{1}{T_1} = J(\omega_0) + 4J(2\omega_0), \tag{2.12}$$

$$\frac{1}{T_2} = \frac{3}{2}J(0) + \frac{5}{2}J(\omega_0) + J(2\omega_0).$$

The above two equations clearly demonstrate that longitudinal relaxation is sensitive to motions with large spectral components at the Lamor frequency and harmonics of the spins in question, while transverse relaxation is also dependent on the static field. Assuming the auto-correlation function of $F(t)$ is an exponential with respect to time, the spectral density function can then be written as [13]

35

$$J(\omega) = \frac{2\tau_c}{1 + \omega^2 \tau_c^2}, \qquad (2.13)$$

where τ_c is the interaction correlation time, i.e., the duration between two molecular configurations; e.g., tumbling or translational time. For a very large τ_c so that $\omega_0 \tau_c \gg 1$, $J(\omega_0) \approx 0$ and $J(0) \approx \tau_c$; while in the case that $\omega \tau_c \ll 1$, $J(\omega_0) \approx J(0) = 2\tau_c$. A maximum of $J(\omega_0)$ is found when $\tau_c = 1/\omega_0$. Fig. 2-1 shows typical T_1 and T_2 values as functions of τ_c. In liquid or gas systems with fast molecular or atomic motions, $\omega \tau_c \ll 1$ is easily satisfied and we have $T_1 \simeq T_2$, and the spectral line is very narrow. On the other hand, motions are very slow in solids, and T_2 has hence been observed to be much shorter than T_1. Moreover, $T_2 \leq T_1$ in all circumstances.

This straightforward formalism explains a wide array of spin relaxation phenomena very successfully. It may be applied in many situations where the dipole-dipole interactions are the dominating contributor to relaxation.

2.5 Chemical Shift

A nuclear spin interacts with the spin and angular momentum of nearby nuclei and their electron clouds, making NMR a sensitive tool for probing its local chemical environment. A nuclear spin surrounded by electrons experiences magnetic shielding in an external field due to the rearrangement of the electron cloud. This leads to slight changes in the spin's Larmor frequency, or a "chemical shift", where the magnitude of shift is highly dependent on the type of atoms the nucleus is bonded to or in close proximity to. Detailed chemical shift measurements have been used to determine the structure of organic molecules. In chemical shift imaging (CSI), separate NMR images of a single sample may be acquired from protons in different chemical environments, providing spatial distribution of different chemical components.

^{129}Xe is well-known for sensitivity to its chemical environment due to the large xenon atomic number and hence its very large electron cloud, which is readily perturbed by external magnetic fields, and hence very large ^{129}Xe chemical shifts have been observed in different situations. For example, a spectrum of ^{129}Xe dissolved

into blood showed a chemical shift of 200 p.p.m [14] up field from the gas peak while liquid and solid xenon have chemical shift of 250 and 300 p.p.m. respectively from the gas peak [15]. Laser-polarized ^{129}Xe is well suited as a tracer of blood flow, allowing the detection of exchange and transport phenomena between gaseous and dissolved phases in the lung, where gas exchange occurs [4].

2.6 Susceptibility-Induced Shift and Line Broadening

When placed in an external field, B_0, any homogeneous material is magnetically affected such that the resulting actual field strength inside the material is given by

$$B = (1 + \chi)B_0, \tag{2.14}$$

where χ is the material's magnetic susceptibility. χ for different categories of materials varies in both amplitude and sign, with most substances being either paramagnetic ($\chi > 0$) or diamagnetic ($\chi < 0$). Paramagnetism arises from the net atomic angular momentum due to unpaired electrons in partially filled orbits. χ values for paramagnetic materials are therefore positive and can be very large. Conversely, diamagnetism, which is found in most compounds, is the result of small disturbances of filled electron orbits, and as such has the same origin as the chemical shift[2]. Diamagnetic materials have negative χ values, since the effect of the orbit disturbance tends to cancel the external field. The absolute value of χ in diamagnetic materials is typically 2 - 4 orders smaller than that for paramagnetic materials. Table 2.3 lists values of susceptibility, χ, multiplied by molar volume V_m (volume per mole) for several substances often used in NMR experiments.

χ as defined in Eqn. (2.14), is the volume susceptibility, and is proportional to the density for a given type of material. The magnetic susceptibility for solids and liquids

---

[2]The major difference between chemical shift and susceptibility is in the range of interactions. Chemical shift affects the nucleus in the same molecule while field due to susceptibility extends far outside the molecule.

Table 2.3: Magnetic Susceptibility of Selected Substances

Material	Formula	$\chi V_m(\times 10^{-6} \text{ cm}^3/\text{mol})$
Helium	He	-2.02
Carbon (graphite)	C	-6.0
Water	H_2O	-12.63
Silicon Oxide	SiO_2	-29.6
Sodium Chloride	NaCl	-30.2
Aluminum oxide	Al_2O_3	-37
Xenon	Xe	-45.5
Copper chloride	$CuCl_2$	+1080
Gadolinium Chloride	$GdCl_3$	+27930

is hence three orders of magnitude larger than that for gases. In porous and granular media where gas and solid phases coexist in the same external field, there exist large variations in magnetic susceptibility. The susceptibility variations are especially high at the boundary between a solid and gas phase. The local magnetic field $\vec{B}^l$ in the void space surrounding the solid grains or particles can be considered to be due to susceptibility in the solid phase, if the much smaller counterpart from gas phase is neglected. $\vec{B}^l$ is highly heterogeneous, with direction and magnitude dependent on both the size and shape of particles, as well as their packing conditions. Audoly *et al.* found that in a tight random pack of spherical beads, the local field at a spatial point that is scaled by the bead size d (i.e., $\frac{\vec{r}}{d}$), is independent of d, and the field gradient decreases inverse linearly with particle size [16]. The case of irregularly shaped particles is very complicated and the field distribution is much broader.

The z-projection of the local field is important when studying fluid flow in porous and granular media using NMR techniques, and is characterized by its average value $\overline{B_z^l}$ and variation $\overline{(\Delta B_z^l)^2}$. $\overline{B_z^l}$ affects the average Lamor frequency and determines the shift of the center of the spectral peaks, while $\sqrt{\overline{(\Delta B_z^l)^2}}$ is the broadness of the field distribution and is related to the peak line width.

2.7 Diffusion and Measurement with NMR

2.8 Diffusion

Diffusion is a process arising from the random Brownian motions of molecules driven by thermal energy. Frequent collisions with neighbors randomize the molecular (or atomic) velocity, and as such the trajectory followed by each molecule may be described by a random walk. The signature of diffusion is that the r.m.s displacement of molecules is linearly dependent on time, with a proportionality constant named the self-diffusion coefficient. The macroscopic manifestation of diffusion is intermixing and transport of mobile substances. The random motion of the molecule makes this process non-reversible, and therefore in NMR experiments with fluids, the result is a spin magnetization pattern that can not be recovered by any means. If spatial variations exist in concentration of the diffusive substance, the diffusion process tends to induce a net flux of molecules towards the region of lower concentration. The magnitude of flux is related to the concentration gradient in a similar manner to other gradient-induced flows, such as Darcy's Law for flow through porous media and Fourier's Law for heat transfer. The diffusion coefficient D is defined in Fick's First Law [17],

$$J = -D\nabla c, \tag{2.15}$$

where c is the molecular concentration, and J is the molecular flux. Diffusion is prominent and fast in gases and liquids, but ionic diffusion in solid crystals also has been observed. At atmospheric pressure and room temperature, typical gas diffusion coefficients are on the order of 10^{-6} m^2/s, which is three orders larger than that in most liquids and 25 orders larger than solid-phase diffusion.

According to the continuity condition, at each spatial point, the material derivative of concentration should be equal the net incoming flux. We therefore have Fick's Second Law

$$\frac{\partial c}{\partial t} = D\nabla^2 c. \tag{2.16}$$

in which a spatially homogeneous diffusion coefficient is assumed.

In NMR and MRI of liquids or gases, the diffusion phenomenon has significant implications. It adversely causes NMR signal attenuation due to molecular diffusion in the presence of a background field gradients by B_0 inhomogeneities or magnetic susceptibility contrast. Conversely, diffusive attenuation of NMR signal also yields useful information about molecular transport, fluid properties and the geometry of solid boundaries, if appropriate NMR methods are used to perform the measurements.

2.8.1   NMR Technique for Measuring Diffusion and Flow

In order to study transport phenomenon with NMR, a quantity called the propagator is introduced, which is the ensemble-averaged probability for a molecule to displace a distance $\vec{R}$ during time t. We denote the propagator by $\bar{P}(\vec{R}, t)$, which is effectively another presentation of the fluid concentration and its dynamics following Fick's Law [18].

$$\frac{\partial P(\vec{R}, t)}{\partial t} + \vec{u} \cdot \nabla P(\vec{R}, t) = D\nabla^2 P(\vec{R}, t). \tag{2.17}$$

Here D is the diffusion coefficient. Assuming a constant coherent flow velocity $\vec{u}$ in a unconstrained system, we have the following solution to Eqn. (2.17),

$$P(\vec{R}, t) = (4\pi Dt)^{-\frac{3}{2}} e^{-\frac{(\vec{R} - \vec{u}t)^2}{4Dt}}, \tag{2.18}$$

which is a gaussian function with the center moving at velocity $\vec{u}$ and the width ever expanding.

The Pulsed-Gradient Spin Echo (PGSE) sequence has been successfully applied in measuring molecule displacement, by applying a spatial modulation to the magnetization and then observing the time-dependence of the modulation [19]. The sequence is schematically shown in Fig. 2-2.

40
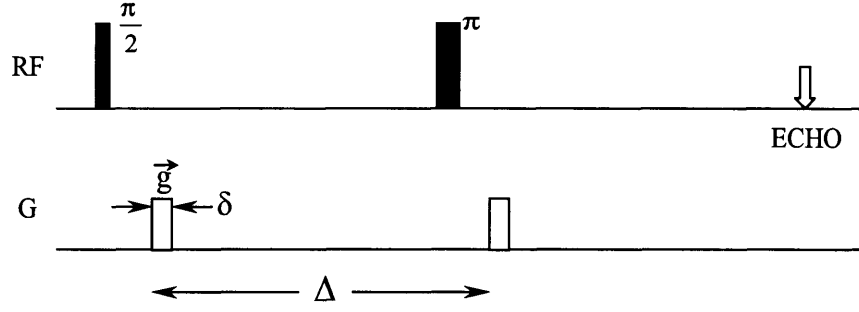
Figure 2-2: PGSE pulse sequence for spin-transport measurement. Two magnetic field gradient pulses are used in combination with 90-180- spin-echo RF pulse sequence. The width of the two gradient pulses is δ, and the separation between them is Δ. The gradient strength $\vec{g}$ is defined as $\vec{g} = \frac{\partial B_z}{\partial x}\vec{i} + \frac{\partial B_z}{\partial y}\vec{j} + \frac{\partial B_z}{\partial z}\vec{k}$.

Two gradient pulses with width of δ are placed after 90° and 180° RF pulses, which produce a spin-echo, to generate and remove the spatial modulation of spin magnetization. If a spin is located at $\vec{r}$ at the time of the first gradient pulse, its transverse moment vector accumulate a phase factor $\phi = \vec{q} \cdot \vec{r}$, in which $\vec{q} = \gamma \delta \vec{g}$. ϕ is inverted after the 180° RF pulse. Suppose the spin moves to $\vec{r}'$ at the time of the second gradient pulse, after which the net phase will be $\phi = \vec{q} \cdot \vec{r}' - \vec{q} \cdot \vec{r} = \vec{q} \cdot \vec{R}$, where $\vec{R}$ is the displacement of the spin during Δ. Since what we observe is the ensemble-averaged displacement made by different spins, the echo amplitude may be written as

$$E(\vec{q}) = \int P(\vec{R}, \Delta) e^{i\vec{q} \cdot \vec{R}} d\vec{R}, \qquad (2.19)$$

which represents the signal strength at the center of echo, and is equivalent to the inverse Fourier transform of the propagator $P(\vec{R}, \Delta)$. If multiple scans are made with incremental $\vec{q}$ values, we may Fourier transform the echo amplitude with respect to $\vec{q}$ to get the transport propagator,

$$P(\vec{R}, \Delta) = \int E(\vec{q}) e^{-i\vec{q} \cdot \vec{R}} d\vec{q}. \qquad (2.20)$$

The PGSE experiment has provided an innovative approach for probing fluid transport either in bulk flow or through porous and granular media. We will see

examples of propagator measurement on gas flow through a fluidized bed in Chapter 6.

The above formulation does not take into account T_2 relaxation, which exists whenever manipulation of the transverse magnetization is performed. But its effect is simply an additional multiplication factor of $e^{-\frac{t_E}{T_2}}$, where t_E is the echo time, or duration between the 90° pulse and the time of the echo center.

There is an upper limit on the measurable molecule displacement. Since $\vec{q} \cdot \vec{R}$ may not exceed the maximum phase angle 2π, and the maximum measurable displacement along the gradient direction is

$$R \leq \frac{2\pi}{\gamma \delta g_m},$$
(2.21)

in which g_m is the maximum strength of gradient pulses applied in the measurement. If Eqn. (2.21) is not satisfied, phase-wrapping occurs yielding incorrect displacement values.

2.9 Imaging

2.9.1 Principle

In the presence of an applied linear field gradient, the magnetic field strength at spatial coordinate $\vec{r}$ varies according to

$$B(\vec{r}) = B_0 + \vec{G} \cdot \vec{r},$$
(2.22)

where $\vec{G} = \nabla B_z$ is the field gradient. The resonance frequency is hence also dependent on $\vec{r}$. In a frame that rotates at the Lamor frequency $\omega_0 = \gamma B_0$, spins with spatial coordinate $\vec{r}$ then rotate at a frequency of

$$\omega(\vec{r}) = \gamma \vec{G} \cdot \vec{r}.$$
(2.23)

The NMR signal is from all spins in the sample covered by the RF coil, and may

thus be written as, aside from a proportionality constant,

$$S(\vec{k}) = \iiint \rho(\vec{r})e^{i\vec{k}\cdot\vec{r}}d^3\vec{r}, \qquad (2.24)$$

where $\vec{k} = \gamma\vec{G}t$, and $\rho(\vec{r})$ is the spatial distribution of spins in the sample. $\vec{k}$ has the units of the reciprocal space. We then have a Fourier-conjugate relationship, now between the NMR signal and the static spatial spin distribution, and a map of spin density is provided by

$$\rho(\vec{r}) = \iiint S(\vec{k})e^{i\vec{k}\cdot\vec{r}}d^3\vec{k}. \qquad (2.25)$$

In magnetic resonance imaging (MRI) experiments, we use different field gradients to vary the value of the three dimensional vector $\vec{k}$, and thus to span the so-called k-space. Molecule density information in real space are retrieved by Fourier transformation on the acquired NMR data. Due to the ubiquity of protons in nature, MRI is now a powerful and well-developed tool widely applied in bioscience, clinical diagnosis and many industrial fields.

2.9.2 One-Dimensional Imaging

One-dimensional imaging, also called the 1D profile measurement, is performed by scanning k-space only along a single direction. The field gradient applied is $G = dB_z/dx\vec{i}$ if a spin density map along the x-direction is desired, which is related to the NMR signal $S(k)$ by

$$\rho(x) = \int S(k)e^{ikx}dk, \qquad (2.26)$$

where $k = \gamma G t$. This measurement could be simply implemented by applying a 90 degree pulse, and then immediately turning on the gradient and starting data acquisition of the NMR FID. However, such image data start from $t = 0$ and are not symmetric along the k-axis. Its Fourier transform hence contains both absorptive and dispersive parts, and the data needs to be phased to remove the dispersive part before
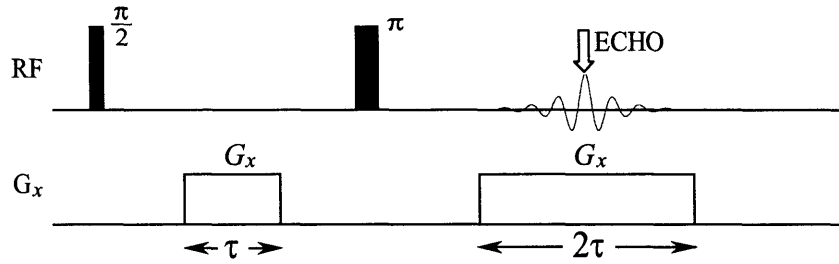
Figure 2-3: Pulse sequence for one-dimensional image acquisition. Read gradient is applied in a standard spin-echo sequence.

reconstructing the image. To circumvent this inconvenience, a pulse sequence based on the spin echo has been designed, by using a refocusing process in the first half of the echo signal as the negative-time part so that the whole signal is symmetrical in k-space. An additional benefit of using the spin echo instead of FID for imaging is that the amount of signal is doubled, which helps to improve the signal-to-noise ratio. Fig. 2-3 shows a typical sequence for measuring one-dimensional images.

The first gradient pulse shifts the starting point in k-space to $k = -k_m = -\gamma G\tau$, while the second gradient pulse, called the read gradient since acquisition takes place at the same time, sweep k-space from $-k_m$ to k_m. Then Eqn. (2.26) can be used to reconstruct the one-dimensional image, by using an appropriate range of k values as integration limits. The field of view for this image acquisition is determined by

$$FOV = \frac{SW}{\gamma G},$$ (2.27)

where SW is the spectral width, equivalent to the sampling frequency for digitization. The optimal resolution in the resulting image is

$$RES = \frac{SW}{\gamma GN},$$ (2.28)

where N is the number of points used for digitization. The actual resolution might be worse than that expected in the above equation, with the two primary reasons being T_2 relaxation and molecule diffusion during the acquisition. T_2 relaxation results in a

44
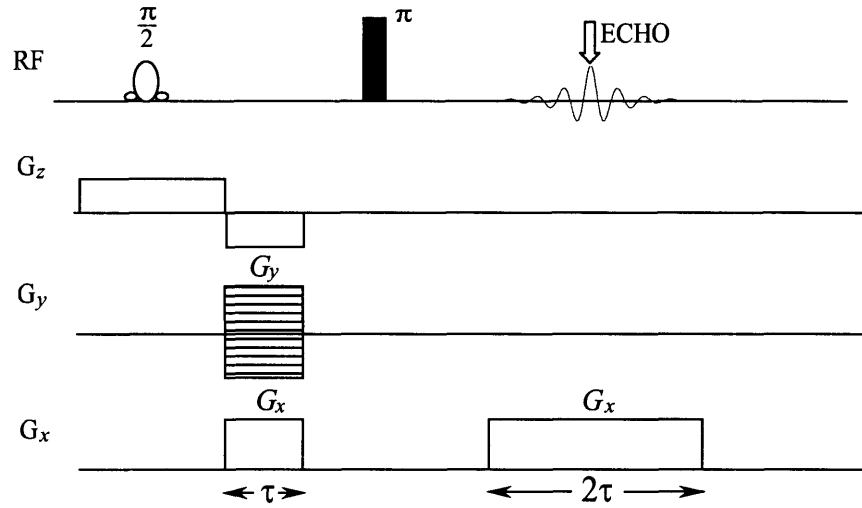
Figure 2-4: Pulse sequence for two-dimensional slice selective image acquisition. A longer, SINC-shaped pulse with reduced power is used to selectively excite a certain slice within the sample. Phase-encoding gradient G_y and frequency-encoding gradient G_x scan the entire k-space.

finite spectrum linewidth equal to $1/\pi T_2$, and no features narrower than that could be identified in the frequency domain. Therefore, T_2-limited resolution may be estimated to be $1/\pi T_2 \gamma G$. Molecular diffusion in the presence of field gradients will cause decay of the transverse magnetization, which equivalently broadens the line by an amount [18]

$$\Delta f_D = 0.6(\gamma^2 G^2 D/3)^{\frac{1}{3}}, \qquad (2.29)$$

and results in a resolution no better than $\Delta f_D/\gamma G$.

2.9.3 Two-Dimensional Imaging

Figure 2-4 shows a typical pulse sequence for obtaining slice-selective two-dimensional images. A SINC-shaped soft RF pulse is used to excite spins only in a particular slice, whose spatial location and thickness are determined by the bandwidth and central frequency of the pulse, together with a simultaneously applied z-gradient G_z. The

45
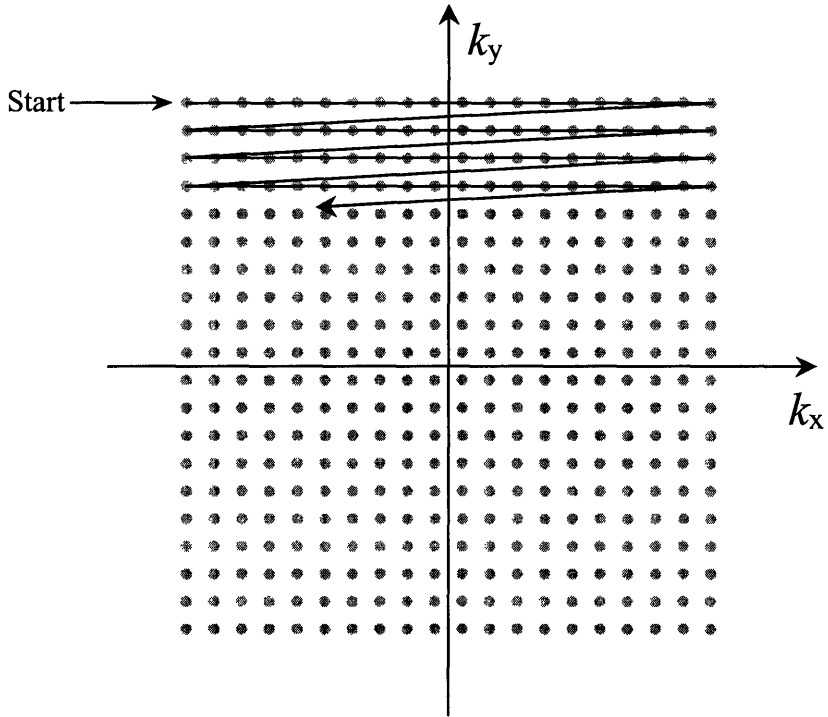
Figure 2-5: Trajectory followed by the two-dimensional image acquisition to scan k-space.

result of the selection is a square profile along the z direction since the shape of the excited magnetization is the the Fourier transform of the pulse shape [18]. Phase-encoding is performed by adding a G_y gradient before the 180°-pulse. Multiple values of G_y are needed in order to sweep through the two-dimensional k-space completely. Fig. 2-5 shows the trajectory for sweeping through k-space, if the pulse sequence shown in 2-4 is applied.

Chapter 3

NMR with Laser-Polarized ^{129}Xe Gas

3.1 Introduction

Traditionally, gas-phase NMR has been difficult primarily because the typical gas density is three orders smaller than that in the liquid phase. Even though the spin polarization achievable at thermal equilibrium in a tesla-scale magnetic field is comparable for gases and liquids, the magnetization - effectively the product of density and polarization - is a thousand times weaker. Therefore, the signal-to-noise ratio (SNR) is extremely poor for gas-phase NMR, and tens of thousands of signal averages are necessary to compensate for the low signal intensity.

This problem has been mitigated by the development of spin-exchange optical pumping, in which the polarization of noble gas species, typically ^{3}He and ^{129}Xe, can be enhanced by up to a factor of 10^5. The implementation and operation of the optical pumping apparatus is well developed now, and the technology is widely applied in biology and medical studies, as well as in material science.

For example, laser-polarized (i.e., hyperpolarized) ^{129}Xe and ^{3}He has been applied to make pratical gas-space MRI at low magnetic fields. In a magnetic field above 1 T in strength, the background field gradient due to susceptibility contrast in the presence of both solid and liquid phases is very large (as large as 100 G/cm in porous

47

media) and results in significant difficulties in both spectroscopy and imaging experiments. In order to effectively reduce the background gradient that scales with the the main field, a low field such as ~ 20 G may be used, which helps reducing line broadness and removing susceptibility-induced artifacts in images. Since the noble gas spin polarization is generated using optical pumping techniques, the available magnetization is unaffected by operating at low magnetic field. Both the signal and tissue noise are reduced at low-field because the e.m.f. is detected at lower Lamor frequency, such that the SNR at low-field is not greatly degraded for polarized noble gas in lungs, and good images can be acquired [20].

Laser-polarized xenon NMR also has important application in the study of interphase exchange of complex media, as xenon is sensitive to its chemical environment. Mair *et al.* observed the exchange dynamics of xenon between gas and liquid phases by a spectroscopy method [21]. The chemical-shift-resolved exchange between the xenon in aqueous and organic environments was also studied [22]. Laser-polarized xenon also enabled observation of penetration into red blood cells from plasma due to the sensitivity of xenon atoms to the two different chemical environments [14].

In this thesis, new techniques have been developed to use laser-polarized noble gas NMR to probe porous and granular media. Conventionally, liquid-phase NMR has been used to study the internal structures of porous media [23, 24] by probing molecular diffusion in the pore spaces. This technique is limited in that the maximum detectable spin displacement is on the order of 100 μm, due to the short T_1 relaxation time of water. Obtaining structural information with longer length scales is therefore not possible, including important transport characteristics such as pore-connectivity, tortuosity and permeability of the porous media, since the typical pore size of many interesting samples is on the order of 100 μm. However, these types of studies may be easily performed with gas-phase NMR since the diffusion coefficient of gas molecules is orders larger than that in liquid phase. Moreover, the interaction between noble gas species and the solid surface is much weaker, resulting in much slower T_1 relaxation rate. The detectable length scale is thus extended up to 2 mm [25]. Gas-phase NMR is also a powerful tool to probe gas dynamics in a gas-fluidized bed, in which solid

particles are suspended in an upflowing gas. The mass exchange between different phases in such a granular system is directly measurable by using susceptibility and chemical-shift contrasts between the phases, as described in Chapter 6.

In this chapter, the spin-exchange optical pumping process is briefly described. Interested readers are referred to relevant publications [26, 27, 28] and a thesis [29] for details. We also describe a home-built polarization and gas delivery system for ^{129}Xe which we used in the rock and fluidized bed studies described in the remainder of the thesis. Specialties in NMR experiments with hyperpolarized gas are also discussed.

3.2 Laser-Polarization of ^{129}Xe

3.2.1 Spin-Exchange Optical Pumping

Laser-polarization of ^{129}Xe is the indirect transfer of angular momentum of polarized photons to the noble gas nuclear spins. High polarization (close to 100%) of laser beams is easily attainable with regular optical components. The critical process is to transfer the photon polarization to ^{129}Xe nuclear spins, which comprises two stages: first the polarization is transferred to electronic angular momentum of Rb atoms (72% abundant ^{85}Rb and 28% abundant ^{87}Rb) by resonant absorption of the photons; second, the polarization is transferred from Rb to ^{129}Xe nuclear spins by Fermi-contact interaction between the two. We will discuss the two processes in this section separately.

Polarization of Rb

The device for generating laser-polarized gas is usually a sealed or valved glass cell containing rubidium, noble gas and small amount of nitrogen gas. Such a cell is typically cylindrically shaped, and a magnetic field with strength of tens of gauss is applied along the direction of the axis in order to provide Zeeman splitting and orientation of quantization. The wavelength of the laser sources used in the polarization process is 794.7 nm, corresponding to the rubidium D1 transition from the
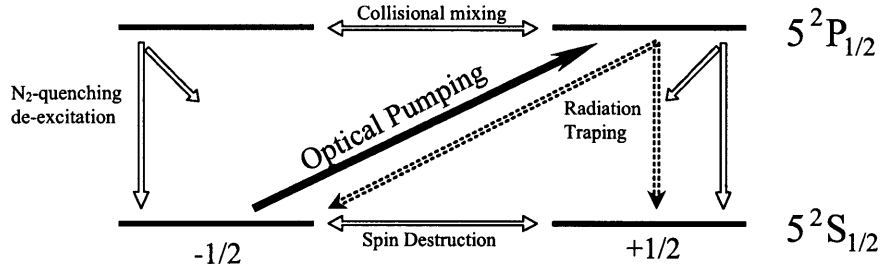
Figure 3-1: Polarization of Rb by depopulation pumping. Various types of transitions are shown between the ground state $5^2S_{1/2}$ and the excited state $5^2P_{1/2}$.

ground state $5^2S_{1/2}$ to the excited state $5^2P_{1/2}$. Rubidium vapor ($\sim 10^{13}$ cm^{-3} at a temperature of ~ 130 °C) is used to effectively absorb the laser energy. The process of rubidium polarization is schematically shown in Fig. 3-1.

Suppose the incident beam is right-circularly polarized (σ^+), which by angular momentum conservation only induces transitions from sublevel $m = -1/2$ of $5^2S_{1/2}$ to $m = +1/2$ of $5^2P_{1/2}$. The populations on the two sublevels in excited state $5^2P_{1/2}$ are rapidly equilibrated due to collisions between rubidium and buffer gas atoms in the system. The basis for this collisional mixing is the fact that the Zeeman energy is orders of magnitude smaller than the thermal energy. Two mechanisms are possible for de-excitation from the excited $5^2P_{1/2}$ state. The first is through radiation of resonance photons that have random angular momentum. These photons are readily reabsorbed by rubidium atoms since the mean free path of the photons in the rubidium vapor is much smaller than the cell dimension. The absorption of unpolarized photons, namely radiation trapping, adversely depolarizes rubidium atoms, which can be significantly alleviated by adding nitrogen buffer gas. The second de-excitation mechanism is nitrogen collisions, which absorbs the rubidium excited-state energy efficiently due to the internal degrees of freedom in the nitrogen molecules. Nitrogen of ~ 100 torr pressure is sufficient in de-exciting rubidium with little radiation trapping. The atoms return to the two sublevels $m = \pm 1/2$ with equal probabilities. Therefore, if two σ^+ photons were absorbed to excite two Rb atoms from $m = -1/2$, only one of which returns to $m = -1/2$ and the other to $m = +1/2$. In the absence of spin destruction or relaxation, this process will eventually deplete atoms in $m = -1/2$

state, resulting in 100% polarization in $m = +1/2$.

However, ground state spin depolarization always occurs due to interaction of rubidium with different atoms in the pumping cell, such as xenon, nitrogen, other rubidium atoms and paramagnetic impurities on cell wall. For the typical conditions of the experiments reported in this thesis, the interactions between rubidium and xenon has been identified to be the predominant spin-destruction contributor. Two types of Rb-Xe interaction exist: spin-rotation and spin-spin, with calculated rates of 2.2×10^5 Hz and 2×10^4 Hz respectively [30, 31]. All other interactions have destruction rates less than 100 Hz and are thus neglected here. If we designate the spin destruction rate by Γ_{SD}, the time-dependence of rubidium polarization P_{Rb} in the optical pumping process may be written as

$$\frac{dP_{Rb}}{dt} = \gamma_{opt}(1 - P_{Rb}) - \Gamma_{SD}P_{Rb}, \tag{3.1}$$

where γ_{opt} is the pumping rate per rubidium atom, which is defined by

$$\gamma_{opt} = \int \Phi(\nu)\sigma(\nu)d\nu, \tag{3.2}$$

where $\Phi(\nu)$ is the incident photon flux per unit frequency and $\sigma(\nu)$ is the absorption cross section per rubidium atom. Therefore the power of the laser source significantly affects γ_{opt}. Assuming time-independent γ_{opt}, and with initial condition $P_{Rb}(t = 0) = 0$, Eqn. (3.1) has a simple solution

$$P_{Rb} = \frac{\gamma_{opt}}{\gamma_{opt} + \Gamma_{SD}}(1 - e^{-(\gamma_{opt} + \Gamma_{SD})t}), \tag{3.3}$$

assuming time-independent γ_{opt} and Γ_{SD}.

Polarization of ^{129}Xe

Exchange of polarization from Rb atoms to ^{129}Xe nuclear spins occurs primarily via the Fermi-contact interaction. There are two scenarios in which the interaction may happen. One is through formation of weakly bounded van der Waals molecules, and

the other is during binary collisions between Xe and Rb atoms. The spin exchange was considered as a spin destruction process in polarization of Rb, but is now the source of polarization for ^{129}Xe. The rate of spin exchange, γ_{SE}, is calculated and measured to be between 10^{-3} and 10^{-2} Hz for Rb density typical for our experiments [32].

The relaxation of ^{129}Xe spin polarization, on the other hand, is primarily due to the presence of paramagnetic impurities on the wall of the cell. A relaxation rate of 10^{-2} Hz was found in Pyrex glass cells, while a special coating technique, which basically attaches long-chain chemicals such as octadecyltrichlorosilane (OTS) [33] onto silicon atoms on the cell wall to prevent approach of xenon, is able to effectively reduce the rate by an order of magnitude. Xenon relaxation will be discussed in more detail in the next section.

We can therefore describe the accumulation of ^{129}Xe polarization similarly by

$$\frac{dP_{Xe}}{dt} = \gamma_{SE}(P_{Rb} - P_{Xe}) - \Gamma P_{Xe}, \tag{3.4}$$

where Γ is the relaxation rate. Given that the Rb pumping rate is seven orders faster than the spin-exchange rate of Xe, Rb polarization is considered to stay at steady state all the time. With the initial condition of $P_{Xe}(t = 0) = 0$, we have the following solution

$$P_{Xe} = \frac{\gamma_{opt}}{\gamma_{opt} + \Gamma_{SD}} \frac{\gamma_{SE}}{\gamma_{SE} + \Gamma}(1 - e^{-(\gamma_{SE}+\Gamma)t}). \tag{3.5}$$

Spin-up time, the time constant for this process to reach steady state is $T_{SpinUp} = \frac{1}{\gamma_{SE}+\Gamma}$. To increase spin polarization, we need to maximize γ_{opt}, which increases with more laser radiation in the spectral width for Rb absorption, and minimize Γ, which can be done by finding better cell material and coating the cell properly. Enormous efforts have been made in reducing the Xe relaxation rate, which was able to improve steady-state Xe polarization by a factor of ~ 5. The typical value of Xe polarization achieved so far is about 10% for Xe gas pressures above 1 bar.
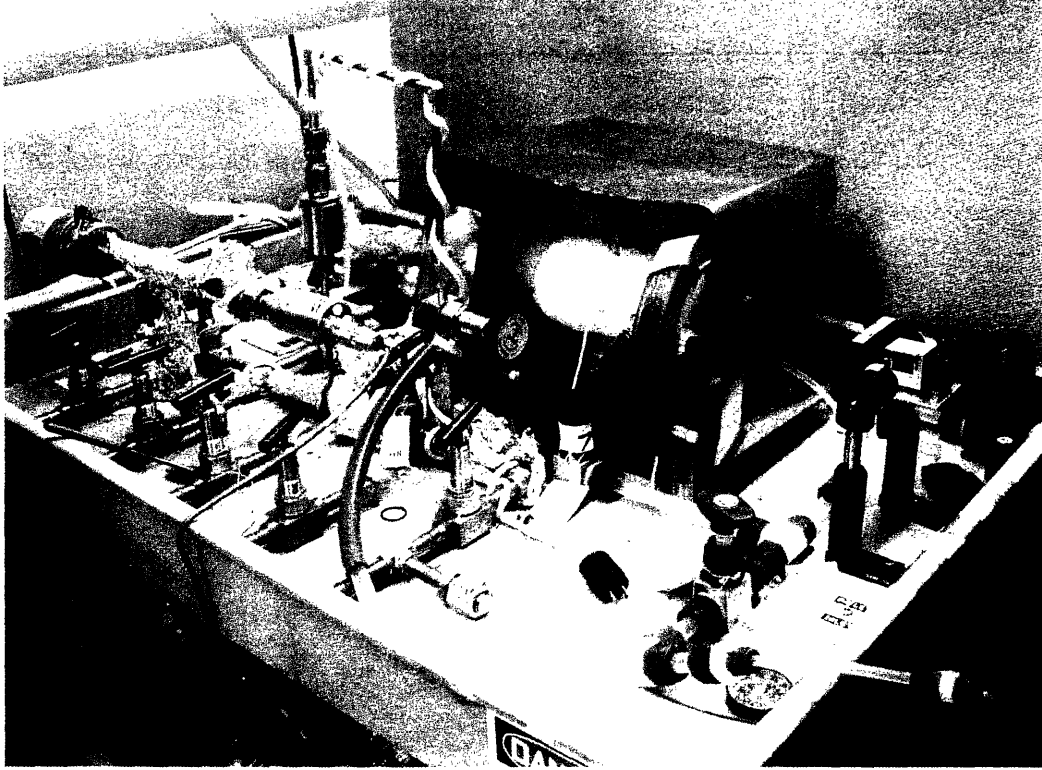
Figure 3-2: ^{129}Xe polarization and delivery system.

3.2.2 ^{129}Xe Polarization and Delivery System

Fig. 3-2 shows a ^{129}Xe polarization and delivery system developed for teh experiments reported in this thesis. The whole system is placed on a cart for easy relocation, and is surrounded by opaque shielding curtains to prevent laser beams from scattering outward.

Fig. 3-3 shows a schematic diagram of different components of the system and their inter-connections. A cylinder (Prexair, pre-mixed specialty gas) provides xenon gas for the polarizer, with 95% natural abundance xenon and 5% nitrogen. A gas purifier (Aeronex, Model SS-35KF-I-4R) is installed to clean any gas species that would potentially oxidize Rb in the cell, such as oxygen, water vapor or any other oxides. The valve labelled V1 is useful for bypassing and protecting the purifier from contacting excessive impurities, especially after the manifold is exposed to the atmosphere when replacing the gas cylinder. The valves V4 and V5 control the inlet

and outlet of the optical pumping cell. V6 and V8 select different regions to be pumped, with V6 leading to the cell and a manifold (which should be cleaned from time to time), and with V8 connecting to the inlet of the back loop for continuous-flow operation. We polarize Xe in the cell and let it flow through a sample. The gas leaving the sample can be looped back onto the polarizer through valve V8 to a vacuum pump (a combination of a turbo pump, model TPU 170 manufactured by Pfeiffer, and a rough pump, model 2QK56B17F5558A by Marathon), which provides the pressure potential for the flow. The flow rate is regulated by a mass flow controller manufactured by MKS (Type 246), with an adjustable range from 20 to 1000 SCCM[1]. In addition, the polarizer allows for attaching a valved cell at its outlet, which can be moved into the magnet after being filled with polarized gas. This is the second operation mode, namely the batch mode, especially useful for calibrating polarization, measuring T_1 and imaging a sealed cell.

The polarization system employs a 30 W broad-spectrum light provided by a laser diode array (LDA) to optically pump Rb vapor ($\sim 10^{13}$ cm^{-3}) induced by heating the cell to 130 °C. The beam out of the source is coupled via a fiber cable to a convex lens through which the divergence of beam and hence its projected size on the cell are adjustable. The beam is first linearly polarized and split into two beams by a polarizing beam-splitter cube (to increase the cross-sectional area of the beam traversing the cell), and then each of the two beams passes through a quarter-wave plate to generate circularly polarized light of the same helicity.

The pumping cell is a two-chambered container built from Pyrex glass, with front side made optically flat to minimize light scattering on the surface. The inner space is for enclosing Xe and Rb, and the outer space works as an oven, heated up by flowing hot air. Before entering the oven, the inflow compressed air first flows through a resistive heater to attain a high temperature (~ 150°C). We use a RTD to monitor the air temperature in the oven and then control the current supply to the heater by comparing the temperature to a set point. The model number of the temperature controller is CN8500, manufactured by Omega Inc.

---

[1]Standard cubic centimeter per minute at STP.

⊗ Valve

Laser Diode Array (LDA)

Optical fiber

Lens

Polarizing
beam-split
cube

Gas
Purifier

OPSE Cell

Mirror

λ/4 Plates

V4

V5

Polarized
gas output

V2

V3

V10

V11

Pressure
Gauge

V13

V1

V6

V9

V12

Mass Flow
Controller

Back loop

V7

V8

Gas Supply

Mixture of 95% xenon
and 5% nitrogen

Vacuum
Pump
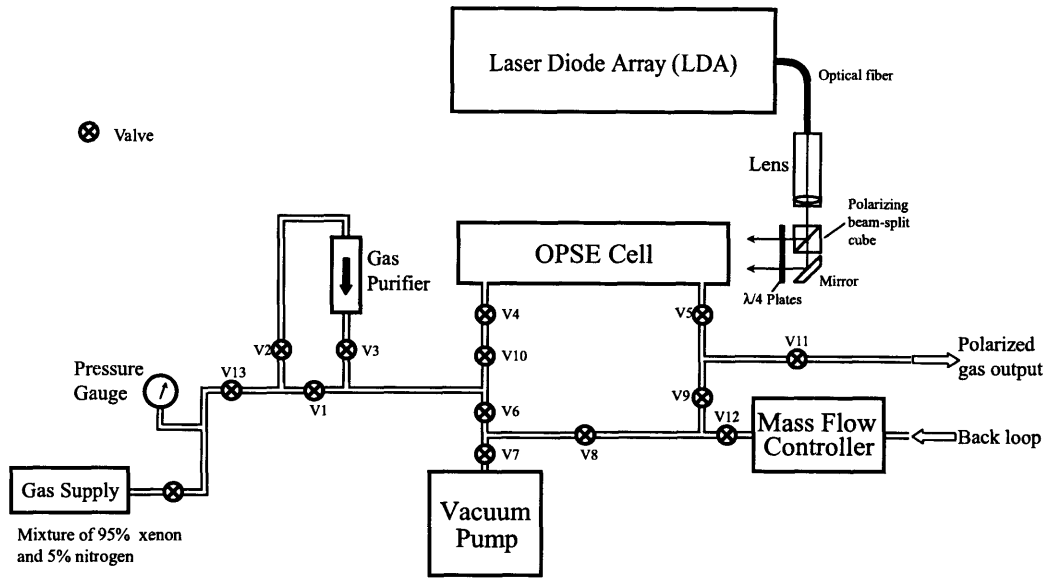
Figure 3-3: Schematic diagram for ^{129}Xe polarization and delivery system.

The pumping orientation field is provided by a pair of Helmholtz coils operating at ~ 18 gauss. However, the fringe field from the 4.7 T magnet at the location where the polarizer is placed is about 6 gauss and vertically oriented, which is perpendicular to the orientation of the pumping cell. The field non-parallel to the angular momentum of the incoming photons will impair the pumping efficiency. In order to reduce the vertical field strength, we wrapped around the cell a thin foil of Mu-Metal that has high magnetic permeability and allows field lines to bypass the cell. The resultant field strength from the fringe field is measured to be less than one gauss.

The inner surface of the pumping cell is uncoated, in order to reduce the spin-up time to about 1 minute. When xenon is polarized at 2.5-bar pressure and flows at 100 SCCM set by the mass flow controller, the dwell time of xenon atoms in the cell with a volume of 84 cc is about 1.6 minutes. Thus the achievable polarization is about 80% of the maximum available from the steady state. This design is optimized for the continuous flow regime. A flexible Teflon tube, instead of metal one, is used to transfer polarized gas into samples sitting inside the magnet, in order to slow down surface relaxation during delivery. T_1 in the tube was measured to be 2 minutes, which is much

longer than the delivery time (~ 10 seconds) for flow at 100 SCCM. The polarization loss due to the varying magnetic field, resulting from the bent tube, is calculated to be minimal [29] and can be ignored. Polarized gas is therefore transferred to the samples with negligible polarization loss. If the polarizer works in batch mode, on the other hand, the pumping process takes about 4 - 5 times spin-up time so that steady-state polarization is attainable.

3.3 Spin relaxation of Gas-Phase ^{129}Xe Polarization

3.3.1 T_1 Relaxation

Three T_1-relaxation mechanisms exist in gas-phase ^{129}Xe samples: bulk, diffusion and surface. Bulk relaxation occurs due to the binary collisions between xenon atoms and other atoms (xenon, buffer gas, etc.), during which nuclear spin interacts with the angular momentum of the molecule formed temporarily by the two atoms. In the absence of Rb vapor, this interaction is relatively weak. For example, for xenon-xenon collisions, the bulk relaxation time is estimated to be $T_1^B = 56/P$ hour [34], where P is the xenon pressure measured in bars. For the typical gas pressure of 2 bar in our experiments, the bulk relaxation time is ~ 28 hours. T_1 relaxation due to xenon-nitrogen collisions is even smaller for our experimental conditions [32].

The second relaxation mechanism originates from diffusion of xenon atoms through an inhomogeneous field, which effectively generates a varying field for the moving atom and can thus induce Zeeman transitions. The relaxation rate in this case is given by

$$\frac{1}{T_1^D} = D\frac{|\nabla B_\perp|^2}{B_0^2},\qquad (3.6)$$

where D is xenon diffusivity, and $\nabla B_\perp$ is the transverse field gradient. For experiments involving xenon flow through interstitial spaces in a particle bed, the field

56

gradient is roughly 1 kHz over a length scale of 0.1 mm, estimated from the line width in the ^{129}Xe spectrum. Xenon diffusivity is 3 mm^2/s, and the Larmor frequency equals 55.4 MHz at 4.7 T. The resulting relaxation time is calculated to be $\sim$ 1000 hours.

The dominant T_1 relaxation mechanism for our experiments is from the interaction of spins with paramagnetic impurities on the surface of the gas container. Adsorption of xenon atoms onto the surface is significant due to the large xenon polarizability. Two stages exist in the surface relaxation process: first, atoms diffuse through the gas space and approach the solid surface, next they get adsorbed and interact with the surface impurities and then re-enter the bulk gas. Multiple collisions of atoms onto the surface may happen before the spins are flipped, dependent on the strength of the surface interaction. Hence an estimation of the spin lifetime is to multiply the average diffusion time before spins approach the surface by the number of collisions necessary to depolarize ^{129}Xe. A typical T_1 value in polarization cells is $\sim$ 5 minutes.

3.3.2 T_2 Relaxation

In a spin system where atoms are bounded to an immobile lattice frame such as in the solid state, T_2 relaxation and the spectrum line reflects the local field experienced by the spins. In liquid and gas systems, however, the molecules are free to move and the magnetic field each spin sees is no longer static but exhibits large fluctuation. We are interested in the relaxation of gas-phase ^{129}Xe spins in the void spaces surrounded by solid phase in porous or granular media, with the variation in the susceptibility-induced local field labelled by $\overline{(\Delta B_z^l)^2}$. The corresponding variation in the resonance frequency is hence given by

$$\overline{(\Delta \omega)^2} = \overline{(\gamma \Delta B_z^l)^2}. \tag{3.7}$$

Bloembergen, Purcell and Pound (BPP) discovered that fast molecule motions can significantly reduce the T_2 relaxation rate, which is often referred to as motional averaging [35]. The time scale of motions is specified by correlation time τ_c, and "fast

motions" occur when the following condition is satisfied

$$\overline{(\Delta\omega)^2}\tau_c^2 \ll 1, \qquad\qquad (3.8)$$

and the resultant line width is $\overline{(\Delta\omega)^2}\tau_c$, which is in accordance with results given by Eqn. (2.12). This conclusion is of great significance because it successfully explains the narrowing of lines in the presence of molecular motions. The BPP theory applies well in the case of T_2 relaxation of gaseous xenon flowing through porous and granular media.

For example, in one of the granular beds studied in our experiments, xenon gas was forced to flow through the interstitial space of spherical glass beads of diameter ranging from 45 to 70 μm and pores on the order of 50 μm. The diffusive correlation time τ_c is ~ 0.2 ms, and the measured line width ($\overline{(\Delta\omega)^2}\tau_c$) is about 100 Hz. Note that $\overline{(\Delta\omega)^2}\tau_c^2 \sim 0.02$ in this case, and condition (3.8) for fast motions is satisfied. We estimate the field variation to be $\sqrt{\overline{(\Delta\omega)^2}} \sim 700$ Hz.

The second bed consisted of irregularly shaped alumina particles sized around 85 μm, corresponding to a correlation time of ~ 0.5 ms. The line width was measured to be 700 Hz in this case, and the value of $\overline{(\Delta\omega)^2}\tau_c^2$ is 0.35, fairly close to unity. The field variation is estimated to be $\sqrt{\overline{(\Delta\omega)^2}} \sim 1.2$ kHz, which is 70% larger than that with spherical glass beads. The magnetic field of larger heterogeneity is due to both the irregular particle shape and the 25% larger magnetic susceptibility of alumina.

3.4   Magnetic Resonance with Laser-Polarized ^{129}Xe

The same principles of proton-NMR theory and technologies apply to ^{129}Xe. However, the details in implementing the experiments may vary since the Lamor frequency of this nuclear species is different from that of protons, and more importantly, the spin polarization of laser-polarized gas is not recoverable with inflow of newly polarized gas. The first issue requires electronics capable of detecting, generating and amplifying radio-frequency oscillations at the correct resonance frequency for ^{129}Xe. The non-recoverable ^{129}Xe polarization results in many modifications on proton-version NMR,

especially in the implementation of pulse sequences and the way data analysis is performed.

3.4.1 Batch Mode

As mentioned in the previous section, the batch mode involves storing polarized gas in a valved cell and manually delivering the gas into the RF coil and the magnet. With a sufficient polarization in the cell, we hope to maximize the number of experiments that can be performed on the finite polarization in the cell. Therefore, RF pulses of low flip angles are extensively used, instead of 90° pulses that consume the entire polarization in a single run. The following are several examples of running NMR experiments in the batch mode.

Polarization Measurement

A common diagnostic experiment is determining the ^{129}Xe polarization in the cell. The procedure is optically pumping ^{129}Xe gas, filling it into a valved cell and checking the signal by acquiring FID after a low-flip-angle pulse. Then the cell is left in the magnet overnight for the polarization to reach the thermal equilibrium, a time-consuming process since bulk T_1 in the 4.7 T field is on the order of hours. On the second day, another FID is acquired after a 90° degree pulse on the thermal polarization. The difference in the amplitudes of the two signals can be used to calculate the polarization by taking into account the different flip angles used.

Fig. 3-4 shows two spectra measured for laser- and thermally-polarized ^{129}Xe in a 20 c.c. valved cell. The flip angle of the RF pulse used to measure the laser-polarized signal is 5°. The ratio between the two polarizations is given by

$$P_{laser} = \frac{I_{laser}/\sin(5°)}{I_{thermal}/\sin(90°)} P_{thermal}, \tag{3.9}$$

where I_{laser} and $I_{thermal}$ are integrals of the two spectra respectively. Thermal polarization was calculated by Eqn. (2.9) to be 4.4×10^{-6} at 4.7 T field strength. The resultant laser-polarization is 3%, which is almost 4 orders of magnitude larger than
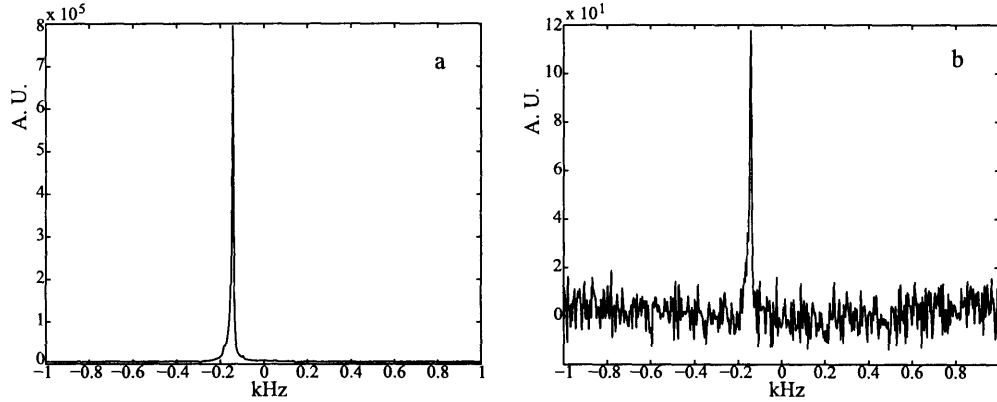
Figure 3-4: Experimental NMR spectra at 4.7 T measured for laser- and thermally-polarized ^{129}Xe in a 20 c.c. cell containing $\sim$ 1 bar ^{129}Xe. a) Signal after steady-state polarization and 5° RF pulse. b) Signal from thermal polarization and 90° RF pulse. These measurements indicate a ^{129}Xe polarization $\sim$ 3% in a).

that achievable under thermal equilibrium in a superconductive magnet.

Flip Angle Calibration and T_1 Measurement

Suppose we are making an FID measurement after a RF pulse of flip angle α. If the delay time before the scan is set to be τ, the longitudinal and transverse spin magnetizations immediately after the pulse are given by

$$
\begin{aligned}
M_z &= M_0 e^{-\frac{\tau}{T_1}} \cos\alpha, \\
M_+ &= M_0 e^{-\frac{\tau}{T_1}} \sin\alpha,
\end{aligned}
$$

where M_0 is the initial magnetization. If this measurement is repeated n times, the magnetization after the nth pulse is

$$
\begin{aligned}
M_z(n) &= M_0 e^{-\frac{n\tau}{T_1}} \cos^n\alpha, & (3.10) \\
M_+(n) &= M_0 e^{-\frac{n\tau}{T_1}} \cos^{n-1}\alpha \, \sin\alpha.
\end{aligned}
$$

60
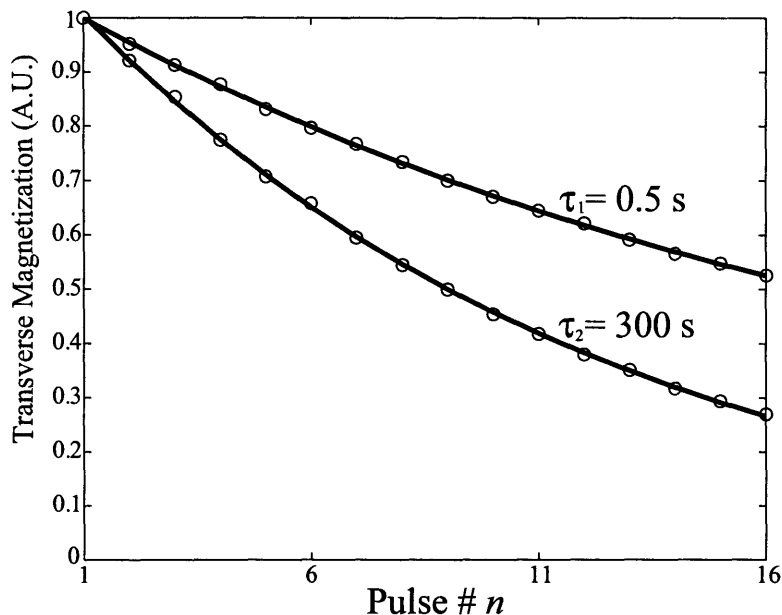
Figure 3-5: Transverse magnetizations as a function of pulse number. Two measurements were done with different τ values as marked in the figure. The flip angles used in the two measurements are the same (10 μs pulse width).

If we perform two of these measurements with different pre-scan delay times and fit the magnetization as a function of n to an exponential, both the flip angle and T_1 values are available.

Fig. 3-5 shows results measured on a valved cell filled with freshly polarized ^{129}Xe. Exponential curve-fitting yields

$$\log\frac{1}{\cos\alpha} + \frac{\tau_1}{T_1} = 0.0521, \text{ and } \log\frac{1}{\cos\alpha} + \frac{\tau_2}{T_1} = 0.0840,$$

from which we determined $\alpha = 23.2°$ and $T_1 = 9.4 \times 10^3$ s $= 2.6$ hr.

Two-Dimensional Imaging with Laser-Polarized ^{129}Xe

Two-dimensional imaging acquisitions require multiple scans for a complete sweep through k-space. Hence a single batch of polarized gas needs to survive all the scans,

RF   α   ⬇ECHO

G_y G_y

G_x G_x $-G_x$

τ 2τ
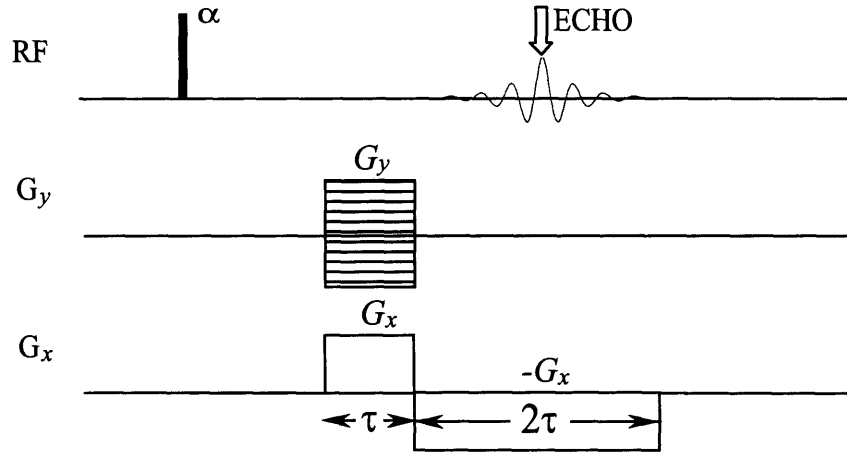
Figure 3-6: Two-dimensional imaging sequence implemented with gradient echo. RF pulse with a low flip angle α is used. Not appropriate if T_2^* is short.

which requires that destructive 90° hard pulses not be applied in the sequence. 180° pulses should also be avoided since magnetization in a noticeable volume of the cell would be destroyed due to the imperfection in these pulses as well as heterogeneity in the RF field. We are therefore not able to use spin echoes in the acquisition sequence. Instead, a gradient echo is used, requiring T_2^* relaxation time in the cell to be longer than that required for phase and frequency encoding with gradient pulses ($\sim$ 5 ms). Shown in Fig. 3-6 is such a sequence for 2D imaging.

The primary issue with this sequence lies in the decay of longitudinal magnetization during the complete scan process, as shown in Eqn. (3.10). The exponential decay in signal intensity in k-space is equivalent to pixel *broadening*, or loss of resolution in the final image, similar to the relationship between FID and spectral linewidth. We can therefore find out the maximum flip angle that won't affect the resolution.

The decay exponent is $n\log\frac{1}{\cos\alpha}$. And $n = \frac{k_y N}{2k_y^m}$, where k_y is the current $\vec{k}$ value along y direction corresponding to scan number n, N is the total number of phase-encoding scans, and k_y^m is the maximum k_y value. Phase-encoding goes from $-k_y^m$ all the way to $+k_y^m$ by incremental steps with a length of $k_y^m/2N$. The resulting loss of resolution is the full width at half maximum (FWHM) of the Fourier transform of

the decay curve, i.e.

$$R_l = \frac{N \log \frac{1}{\cos\alpha}}{2\pi k_y^m}. \tag{3.11}$$

For optimal image acquisition, R_l should be less than the resolution specified by the sequence, and we have

$$\frac{N \log \frac{1}{\cos\alpha}}{2\pi k_y^m} < \frac{1}{2 k_y^m}, \tag{3.12}$$

or

$$\alpha < \cos^{-1}(e^{-\pi/N}). \tag{3.13}$$

The above discussion ignored T_1 relaxation effects since the period between different scans is always much shorter than T_1. But it may be easily included if the assumption is not true. If 64 phase-encoding scans are needed in a two-dimensional image acquisition, the maximum flip angle is therefore 17.8°. This might not provide sufficient SNR if the total initial magnetization is not large enough. In that case, variable flip angle may be used so that the consumption and decay of the longitudinal magnetization is compensated by later larger flip angles. If we designate the flip angle for pulse n to be α_n, the transverse magnetization after the n-th pulse is then

$$M_+(n) = (\prod_{i}^{n-1} \cos\alpha_i) \sin\alpha_n. \tag{3.14}$$

The variable flip angle technique requires $M_+(n) = M_+(n-1)$, or

$$\sin\alpha_n = \tan\alpha_{n-1}. \tag{3.15}$$

Eqn. (3.15) guarantees that the magnetization rotated to the transverse plane is constant each time with the cost of increased complexity in pulse sequence implementation. Given the high spin polarization produced by OPSE technology, it suffices to use constant flip angles for most situations.

3.4.2 Continuous Flow

NMR experiments with the polarizer working in the continuous flow mode are very similar to conventional proton magnetic resonance. Both 90° and 180° pulses may be applied since the spin polarization is replenished by inflow of freshly polarized gas. Instead of a *relaxation* delay before starting each scan, a certain amount of time is needed to allow to pass until gas in the entire volume to be refreshed with polarized ^{129}Xe, with the delay dependent on the flow rate and the sample volume.

In particular, any experiment involving slice-selection, e.g., two-dimensional imaging, can be implemented neatly under continuous flow mode. The magnetization in a thin slice is consumed completely for NMR detection, and the gas flow will quickly replenish that slice so that the delay time between different scans is very short. The advantage is obvious when compared to slice selection on a static sample, where renewal of magnetization is dependent on the slower diffusion.

We used the continuous flow mode in most experiments on investigation of gas flow in porous and granular media. Batch mode was only used when calibration and maintenance of the system were needed.

Chapter 4

Simultaneous Measurement of Rock Permeability and Effective Porosity using Laser-Polarized Noble Gas NMR[1]

4.1 Introduction

Porous media are ubiquitous in nature. Examples include granular materials, foams, ceramics, animal lungs and sinuses, and oil- or water-bearing "reservoir" rocks. Diagnosing the structure of these materials is relevant to a wide range of scientific and technological problems. For example, knowledge of the fluid transport properties of reservoir rocks is important for the monitoring of contaminant percolation and for oil extraction. Similarly, knowledge of the evolution of the porous structure of materials subjected to large thermal or mechanical stress may help characterize the dynamics of cracking and material failure. There is a continuing need for the development and application of new techniques that characterize complex systems such as fluid flow in porous media.

Two of the most important parameters used to characterize porous media are permeability and effective porosity [36]. Permeability is a measure of the ability of a porous material to transmit fluid, and is defined by Darcy's law as the proportionality constant relating the volume flow rate, $\vec{q}$, for an incompressible fluid of viscosity μ, to the pressure gradient, ∇P, driving the flow [37]:

$$\vec{q} = -\frac{kA}{\mu}\nabla P, \qquad (4.1)$$

where k is the permeability and A is the total cross-sectional area of the porous material. (Note that Darcy's law is valid only for linear laminar flow where the Reynolds number (Re), based on average pore diameter, does not exceed 1.0 [36]. In the experiments reported here, Re $\sim 10^{-5}$.) Permeability is determined by measuring the fluid pressure difference across a sample, and the resulting flow rate through it. There are various techniques that realize this basic scheme, including measurements of gas flow [38].

In one class of porous media of great practical interest, reservoir rocks, permeability can vary greatly. For example, in sandstones, where the pores are large and well connected, the permeability is large: $k \sim 1$ D [39], where 1 D = one darcy = 0.978 μm^2 [36]. Impermeable rocks, such as siltstones, consist of fine or mixed-sized grains, and hence have smaller or fewer interconnected pores with $k \sim 1$ mD [39].

The total or absolute porosity, ϕ, is simply the fractional volume of all void space inside a porous material, whether or not the voids are interconnected and make a continuous channel through the sample. More useful, when considering fluid flow, is the effective porosity ϕ_e: the volume fraction of pore spaces that are fully interconnected and contribute to fluid flow through the material, excluding dead-end or isolated pores that are not part of a flow path. Effective porosity also relates the average fluid velocity, or Darcy velocity $v_d = \vec{q}/A$, to the mean velocity of a tracer flowing through the pore space, v_s, according to the simple relation [40]:

$$\phi_e = \frac{A_f}{A} = \frac{v_d}{v_s} = \frac{\vec{q}A}{v_s} = \frac{-k\nabla P\mu}{v_s}, \qquad (4.2)$$

where A_f is the effective cross-sectional area of the sample where flow occurs. Although effective porosity can be defined in a number of ways, absolute porosity is always larger than or equal to the effective porosity for a given sample [40]. An accurate measure of effective porosity is important for understanding fluid flow in porous media, and phenomena such as the diffusion, dispersion and deformation of the solid phase due to stress resulting from the applied pressure.

Absolute porosity and permeability are readily measurable with existing techniques [41], although the two parameters generally need to be measured separately with different methods, and many of the techniques (e.g., mercury intrusion porosimetry), are either invasive, toxic, or both [41, 42]. Moreover, effective porosity, the more informative porosity parameter for fluid transport in porous media, cannot generally be measured directly with current standard techniques [40, 43].

In this chapter we demonstrate the simultaneous measurement of permeability and effective porosity in reservoir rocks using laser-polarized noble gas NMR imaging, a powerful, non-invasive probe of the spatial distribution and motion of fluid inside a porous sample. NMR of gas-phase samples has traditionally been hampered by low nuclear spin density, ~ 3 orders smaller than for solid or liquid samples, which results in a much lower signal to noise ratio for thermally spin-polarized samples at the same magnetic field strength. Here, we use the spin-exchange optical pumping method [44] to enhance the nuclear spin polarization of ^{129}Xe gas by 3 - 4 orders of magnitude, producing a magnetization density which can be as high as water samples at magnetic fields of ~ 1 tesla. An additional benefit of using a laser-polarized gas, especially for tracer studies like those used here, is the ability to induce a step-change in the magnetization with a train of saturating RF and gradient pulses [15, 45]. As the gas polarization has been produced external to the main applied magnetic field, such a saturation train essentially sets the xenon magnetization to zero – with the only replenishment being from polarized gas that flows into the sample after magnetization saturation. The thermal (Boltzmann) polarization that re-establishes itself after the saturation train is so small by comparison as to be negligible. The ability to manipulate the xenon magnetization in this way is a key component in

these measurements.

To determine permeability and effective porosity, we monitored the movement of ^{129}Xe spins through each rock sample by measuring the one-dimensional NMR signal profile, yielding a one-dimensional image of the spatial distribution of spin magnetization that is dependent on the characteristics of the porous medium. We measured steady-state ^{129}Xe NMR profiles with the polarized gas flowing through the sample; we also measured penetration profiles for different inflow times. These 1D images were analyzed in terms of a well-known application of Darcy's Law to porous media that are homogeneous on large length scales ($\geq$ 100 μm in the present case) [39, 46].

4.2 Experimental Procedure

Xenon gas (26.4% abundance of ^{129}Xe) was spin-polarized in a glass cell which contained a small amount of Rb metal and a total gas pressure of $\sim$ 4 bar, with $\sim$ 92% xenon and the remainder N_2. We heated the cell to 105°C to create an appropriate Rb vapor density and induced spin polarization in the Rb vapor via optical pumping on the Rb D1 line ($\sim$ 795 nm) using $\sim$ 12 W of broad-spectrum ($\sim$ 2 nm) light provided by a fiber-coupled laser diode array [44, 47]. In about 5 minutes Rb-Xe collisions boost the ^{129}Xe spin polarization to $\sim$ 1%, and a continuous output of polarized xenon gas was then provided to a porous sample in an NMR instrument at a controlled flow rate of 50 cm^3 per minute. Fig. 4-1 shows a schematic of the experimental apparatus.

We employed five rock samples with a range of permeability spanning three orders of magnitude in our demonstration measurement. The high permeability rock was Fontainebleau sandstone, a simple, homogeneous rock type that is largely free of paramagnetic impurities and has a regular and fairly narrow distribution of pore sizes ($\sim$ 10 to 100 μm) [46]. We also studied a low permeability rock, Austin Chalk, a very fine grained, spatially homogeneous rock with high porosity but very small ($<$ 10 μm) and poorly connected pores. We performed similar measurements on three other types
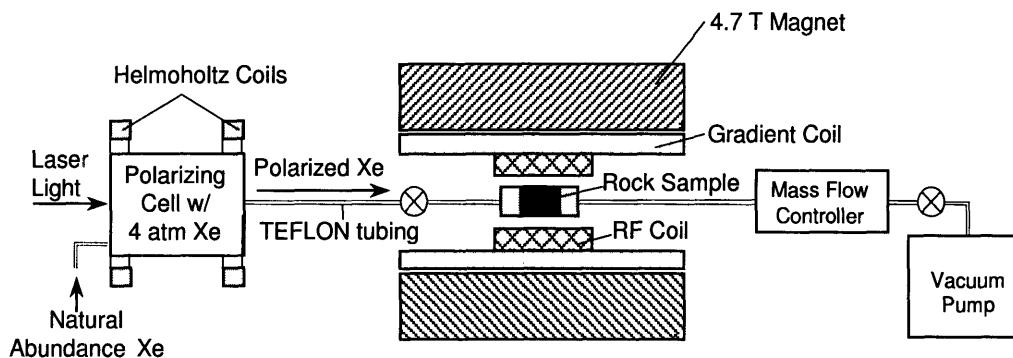
Figure 4-1: Schematic diagram of the experimental apparatus. The 4.7 T magnet resides in a small RF shielded room. The remaining equipment was placed outside the room, beyond the 5 gauss line of the magnet. Narrow 1/8 inch ID Teflon tubing connected all pieces of the apparatus. The tubing length was approximately 2.5 m from the polarizer to the sample, and 5 m from the sample to the mass flow controller.

of rock cores with varying permeability and porosity values; Bentheimer sandstone, Edwards limestone and Indiana limestone. All rock samples were cylindrically shaped, with a diameter of 1.9 cm and a length of 3.8 cm. We baked the samples under vacuum before use to ensure absorbed water in the pore space was removed. The rock being probed was held in a sample cell primarily built of machined Teflon, inside of which the ^{129}Xe spin relaxation time is $T_1 \sim 2$ minutes without rock samples, much larger than the values previously measured in the pores of rock samples (^{129}Xe $T_1 \sim 1 - 10$ seconds) sealed in a glass cell. The rock cell was connected to the xenon polarization chamber via 1/8 inch ID Teflon tubing, and the entrance to the rock cell also contained a diffuser plate made of 5 mm thick Teflon, with 46 holes each of diameter 1.2 mm, to distribute flowing xenon gas evenly into the sample. The exit side of the sample was connected via similar Teflon tubing to a vacuum pump that induced gas flow through the rock sample. The gas flow rate was regulated by a mass flow controller, placed just before the vacuum pump, which provided steady flows ranging from 10 to 1000 cm^3/s. In continuous flow mode, the gas moved from the supply bottles, through the polarization chamber and then the rock sample, and finally through the mass flow controller and on to the vacuum pump.

The rock sample was positioned in a 4.7 T horizontal bore magnet, interfaced to a
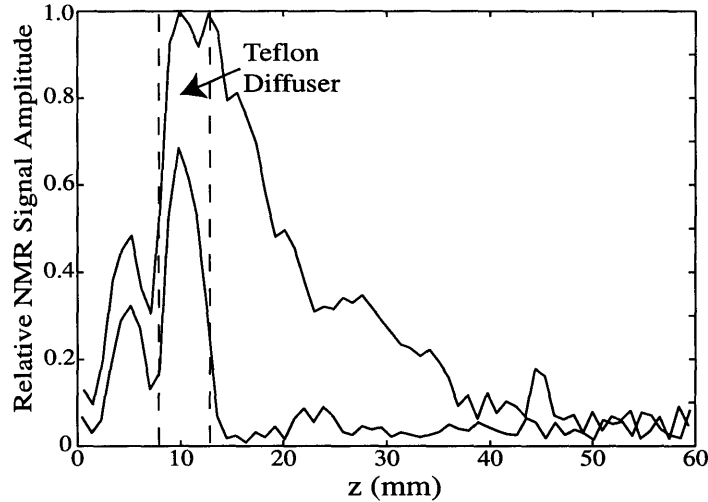
Figure 4-2: Example NMR profiles (i.e., 1D images) of laser-polarized xenon gas flowing through the Austin Chalk sample while applying a CPMG sequence before the image acquisition. The profiles include the regions occupied by the rock sample ($z \geq 13$ mm) and the Teflon diffuser plate (indicated by the dashed lines). The unattenuated profile ($t_E = 2.1$ ms) was obtained after only a single spin-echo before image acquisition. The attenuated profile ($t_E = 33.6$ ms) was acquired after sixteen $180°$ pulses, and is thus heavily T_2-weighted. In this profile, the ^{129}Xe signal from the rock has completely dephased and is very small, while the ^{129}Xe NMR signal from the diffuser plate remains significant. NMR profiles such as these allow $T_2(z)$ to be determined, and also permit unambiguous identification of the position of the rock core in the experimental apparatus.

Bruker AMX2-based NMR console. We employed an Alderman-Grant-style RF coil [Nova Medical Inc., Wakefield, MA] for ^{129}Xe observation at 55.4 MHz. All NMR imaging experiments were non-slice-selective one-dimensional profiles along the flow direction employing a hard-pulse spin echo sequence with echo time, $t_E = 2.1$ ms and an acquired field of view of 60 mm. A spin echo sequence was applied to preserve the full echo signal with determined center of k-space, which is necessary in later data acquisition. Steady-state flow profiles were obtained by this method without pre-saturation. The ^{129}Xe polarization penetration depth was measured by preceding the echo sequence with a saturation train of RF and gradient pulses to destroy all ^{129}Xe magnetization inside the rock sample; and then waiting a variable time, τ, to allow inflow of ^{129}Xe magnetization before acquiring 1D NMR profiles.

In addition to single spin-echo experiments, we used the CPMG technique [48] to

measure the ^{129}Xe spin coherence relaxation time (T_2) in the rock sample and diffuser plate, with $t_E = 2.1$ ms and one to sixteen 180 ° RF pulses prior to echo acquisition. For each point in the profile, we fit the amplitude decay, as a function of the number of echo loops before acquisition, to an exponential to yield $T_2(z)$. Fig. 4-2 shows example T_2 weighted profiles from such an acquisition sequence. After sixteen 180° pulses (33.6 ms), the xenon magnetization in the rock has completely dephased, but is clearly visible in the inflow tube and diffuser, thereby allowing us to define the start of the rock with an accuracy of about 1 mm (equivalent to the spatial resolution of the 1D NMR images).

To confirm the NMR experiments, three of the five rock samples (Fontainebleau sandstone, Austin chalk and Edwards limestone) were also characterized independently using standard techniques by a commercial company [New England Research, White River Junction, VT]. This company used a gas pycnometer to determine absolute porosity from gas pressure changes via Boyle's Law [49]. They measured permeability via the steady-state gas flow method with a standard gas permeameter [37, 38]. In these standard measurements, the accuracy of the absolute porosity value is generally accepted to be $\sim 1\%$, and that of the permeability value $\sim 10 - 20\%$.

4.3 Effective Porosity Measurement and Results

To determine the effective porosity, we measured ^{129}Xe NMR spin echo profiles from each sample under the condition of steady-state polarized gas flow. Fig. 4-3 shows profiles acquired for all the rock samples. The amplitude of the profile at each point along the sample is proportional to the ^{129}Xe gas density and spin polarization, the void space volume participating in gas flow, and the effect of spin coherence relaxation. As discussed in the next section, we corrected for gas density and polarization variation along the rock (see Fig. 4-3), such that the ratio of profile amplitudes in the diffuser plate (a medium of known porosity) and the rock was proportional to the ratio of the average void space volumes contributing to fluid flow in the two regions, with weighting factors accounting for T_2 relaxation. Our measurements of T_2

71

a) FontaineBleau Effective porosity = (11.3 ± 0.7)%

Teflon Diffuser

b) Austin chalk Effective porosity = (18.4 ± 0.9)%

c) Edwards limestone Effective porosity = (15.1 ± 1.1)%

d) Bentheimer Effective porosity = (11.2 ± 1.2)%

e) Indiana limestone Effective porosity = (7.10 ± 0.6)%

Relative NMR Signal Amplitude

z (mm)
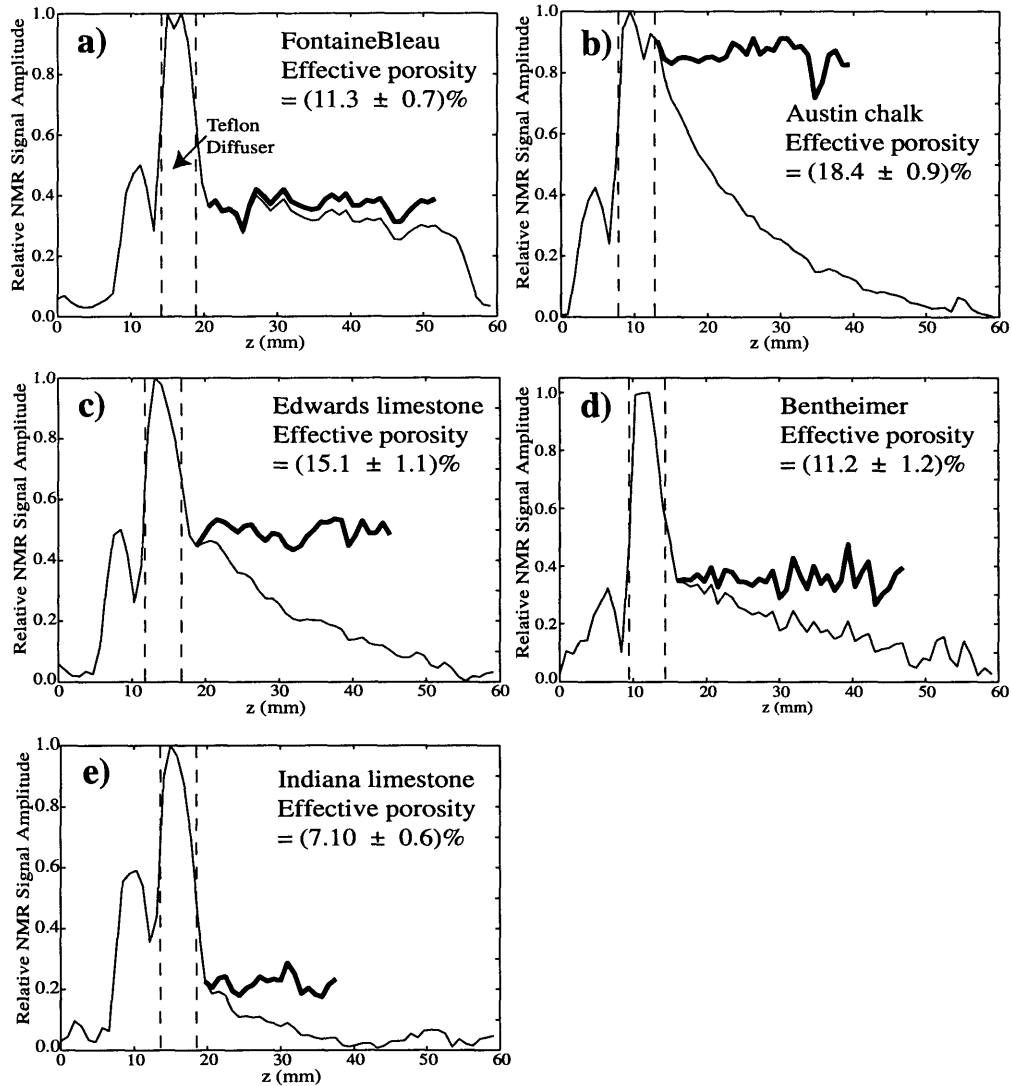
Figure 4-3: NMR profiles (i.e., 1D images) of laser-polarized xenon gas flowing through samples of (a) Fontainebleau sandstone, (b) Austin Chalk, (c) Edwards limestone, (d) Bentheimer and (e) Indiana limestone, with both the gas flow rate and xenon magnetization in steady state. The profiles include the regions occupied by the rock sample and the Teflon diffuser plate (indicated by dashed lines). The bold lines show the profiles corrected for gas density and polarization variation in the rock. For such typical NMR profiles, we averaged 32 signal acquisitions, each made with $t_E = 2.1$ ms, and achieved a 1D spatial resolution of approximately 1 mm.

as a function of position along the sample yielded distinct values corresponding to ^{129}Xe in the diffuser plate ($T_2^{dif} = 76.8$ ms) and the rock cores ($T_2^{rock} = 4.59$ ms in Fontainebleau sandstone and 12.3 ms in Austin Chalk). (These differences in T_2 arise from differences in magnetic susceptibility and hence background magnetic gradients, as well as differing wall interactions.)

Hence, we determined the effective porosity of the sample from the relation:

$$\phi_e = \frac{A_{dif}}{A_{rock}} \frac{S_{rock}}{S_{dif}} \frac{\exp(-t_E/T_2^{dif})}{\exp(-t_E/T_2^{rock})}, \tag{4.3}$$

where A_{dif} is the cross-sectional area of void space in the diffuser; A_{rock} is the rock sample cross-sectional area; S_{dif} and S_{rock} are the NMR profile amplitudes in the diffuser and the rock respectively; and t_E is the echo time used to acquire the profile. ^{129}Xe spins located in isolated or dead-end pores larger than the one-dimensional gas diffusion length during t_E (~ 50 μm for our experimental conditions) contributed no significant NMR signal to the effective porosity measurement. We determined the rock profile amplitude (S_{rock}) at a distance of 1 mm from the diffuser-rock interface on the upstream side of the gas flow. This 1 mm offset was chosen so that no ^{129}Xe in the diffuser contributed to S_{rock}, and so that insignificant depolarization had occurred for the ^{129}Xe in the well-connected pores that contribute to the rock's effective porosity and permeability. We also used the 1 mm offset point in the rock profile to calculate the correction for gas density and polarization variation along the rock. For additional 1 mm offsets, we found that the effective porosity derived from our measurements varied by less than other sources of uncertainty: the fractional variations for all the rock samples are less than 7%. Table 4.1 lists the effective porosities we determined for the Fontainebleau sandstone, Austin Chalk and Edwards limestone, as well as the absolute porosities determined using the gas pycnometer. Results on the two other rock cores are also included, but without comparison measurements using the standard method.

4.4 Permeability Measurement and Results

The permeability of a porous medium is generally determined from the volume flow rate of fluid under a given pressure gradient [38]. Here, we employed NMR imaging to determine the flow rate of laser-polarized ^{129}Xe gas through reservoir rocks, using the pre-saturation method described above to image only xenon spins that flow into the rock during a defined period.

A one-dimensional NMR profile acquired with a spin-echo sequence provides a good representation of the spatial distribution of spin magnetization per unit length, $M(z)$, which can be expressed as [18]:

$$M(z) = A \cdot \phi_e \cdot n(z) \cdot \lambda \cdot p(z) \cdot (\gamma \hbar I), \qquad (4.4)$$

where A is the cross-sectional area of the sample; ϕ_e is the effective porosity; $n(z)$ is the gas number density along the direction z of gas flow; λ is the isotopic abundance of ^{129}Xe nuclear species in the Xe gas; $p(z)$ is the ^{129}Xe spin polarization; and $\gamma \hbar I$ is the spin magnetization per polarized ^{129}Xe atom (nuclear spin $I = 1/2$). On length scales > 1 mm, where ϕ_e is spatially uniform for the rocks we studied, only the number density, n, and polarization, p, are spatially dependent. The parameters, n and p, as well as the gas velocity, v, and spin relaxation time, T_1, fluctuate greatly within the pore length-scale, due to the complicated pore structure in reservoir rocks. Our experiment was only sensitive to cross-sectional averages of these parameters, resulting in a z-dependent measurement on a scale $\sim$ two orders larger than the typical pore size.

Assuming uniform laminar flow (a reasonable assumption for the very low Reynolds number, Re $\sim 10^{-5}$, of these experiments), the 1D distribution of the gas number density inside the rock sample is given by [50]:

$$n(z) = \frac{1}{k_B T} \sqrt{P_i^2 - (P_i^2 - P_o^2)\frac{z}{L}}, \qquad (4.5)$$

where P_i and P_o are the inlet and outlet gas pressures across the sample; L is the

sample length; k_B is Boltzmann's constant; and T is the gas temperature.

The relaxation of xenon spins in the rock is dominated by surface interactions with paramagnetic impurities at the grain surfaces. Bulk xenon spin relaxation due to xenon-xenon collisions is several orders of magnitude slower [34]. Therefore, T_1 for xenon infused in a porous rock can be well-approximated as a mono-exponential decay of magnetization. The ^{129}Xe spin polarization decreases along the flow path due to spin relaxation in the rock; the attenuation over a spatial displacement dz being $\frac{dp(z)}{dz} = \frac{-1}{v(z)T_1(z)}$, where $v(z)$ is the spatially-dependent gas flow velocity and $T_1(z)$ is the spatially-dependent mono-exponential relaxation time. While a single Xe atom travels along random tortuous paths defined by the microscopic pore structure, $v(z)$ represents the statistically averaged spin displacement, averaged over all spins in a plane perpendicular to the flow direction. Applying Darcy's Law, for $v(z) = \frac{\vec{q}}{A\phi_e}$, having the gas number density inside the rock (Eq. (4.5)) in mind and assuming that ^{129}Xe gas follows the ideal gas law, one finds:

$$v(z) = -\frac{k}{\phi_e \mu}\frac{dP}{dz} = \frac{1}{2}\frac{k}{\phi_e \mu}\frac{P_i^2 - P_o^2}{LP(z)}. \qquad (4.6)$$

where the spatially-dependent xenon gas pressure, $P(z) = n(z)k_B T$, μ is the xenon viscosity and k is the sample permeability. The spatial dependence of polarization is therefore found to be:

$$p(z) = p_0 \exp(-\int_0^z \frac{dz}{v(z)T_1(z)}) = p_0 \exp(-\frac{2\phi_e \mu}{k\beta}\frac{L}{P_i^2 - P_o^2}z) \quad , \qquad (4.7)$$

where $p_0 = p(z = 0)$ and β relates the ^{129}Xe T_1 to gas pressure via $T_1(z) = \beta P(z)$, assuming T_1 is dominated by wall relaxation and hence by gas diffusion to pore walls [51], a reasonable assumption given the long inherent bulk ^{129}Xe T_1.

Combining Eqs. (4.4) to (4.7), the spatial dependence of the ^{129}Xe spin magnetization per unit length in a porous rock can be written as

75

$$M(z) = A\phi_e\lambda\frac{1}{k_BT}\left(\gamma\hbar I\right)p_0\sqrt{P_i^2 - (P_i^2 - P_o^2)\frac{z}{L}}\exp(-\frac{2\phi_e\mu}{k\beta}\frac{L}{P_i^2 - P_o^2}z) \quad . \quad (4.8)$$

Our permeability experiments were performed with a steady state gas flow, but with a zero initial [129]Xe spin polarization, created by the application of a series of fast RF and magnetic field gradient pulses to spoil any spin polarization in the sample on timescales of 20 ms, which is much faster than the time for gas transport through the sample (on the order of 10 s). During a subsequent delay or propagation time, τ, polarized gas entered the sample, after which we acquired an NMR profile. We repeated this process for different propagation times, thereby revealing the rate of flow of laser-polarized [129]Xe gas through the rock's pore space. Data for all the rock cores are shown in Fig. 4-4. The penetration depth, ξ, was calculated at each τ by dividing the total [129]Xe NMR signal in the rock, determined from the MRI profile integrated over the rock length, by the signal amplitude at $z = 0$. We measured the inlet and outlet pressures P_i and P_o with bridge pressure sensors. (For example, $P_i \approx$ 3.73 bar and $P_o \approx 0.78$ bar for the low-permeability Austin Chalk, and $P_i \approx P_o \approx$ 4.33 bar for the high permeability Fontainebleau.) Also, we used the xenon viscosity $\mu = 2.324 \times 10^{-5}$ Kg/m-s, for the typical experimental temperature of 25 °C [52]. (Gas viscosity is essentially independent of pressure and only minimally temperature dependent [52].) Using Eqs. (4.5) and (4.6) as well as the ideal gas law ($P(z) = n(z)k_BT$), we derived a relation between the propagation time τ and penetration depth ξ:

$$\tau = \int_0^\xi \frac{dz}{v(z)} = \frac{4}{3}\frac{\phi_e\mu}{k}\frac{L^2}{(P_i^2 - P_o^2)^2}\left\{P_i^3 - \left[P_i^2 - (P_i^2 - P_o^2)\frac{\xi}{L}\right]^{\frac{3}{2}}\right\} \quad . \quad (4.9)$$

From Eq. (4.9), we determined each rock's permeability, k, using the experimentally measured values for P_i, P_o and L, the known value of μ, and the values of ξ calculated from the NMR profiles.
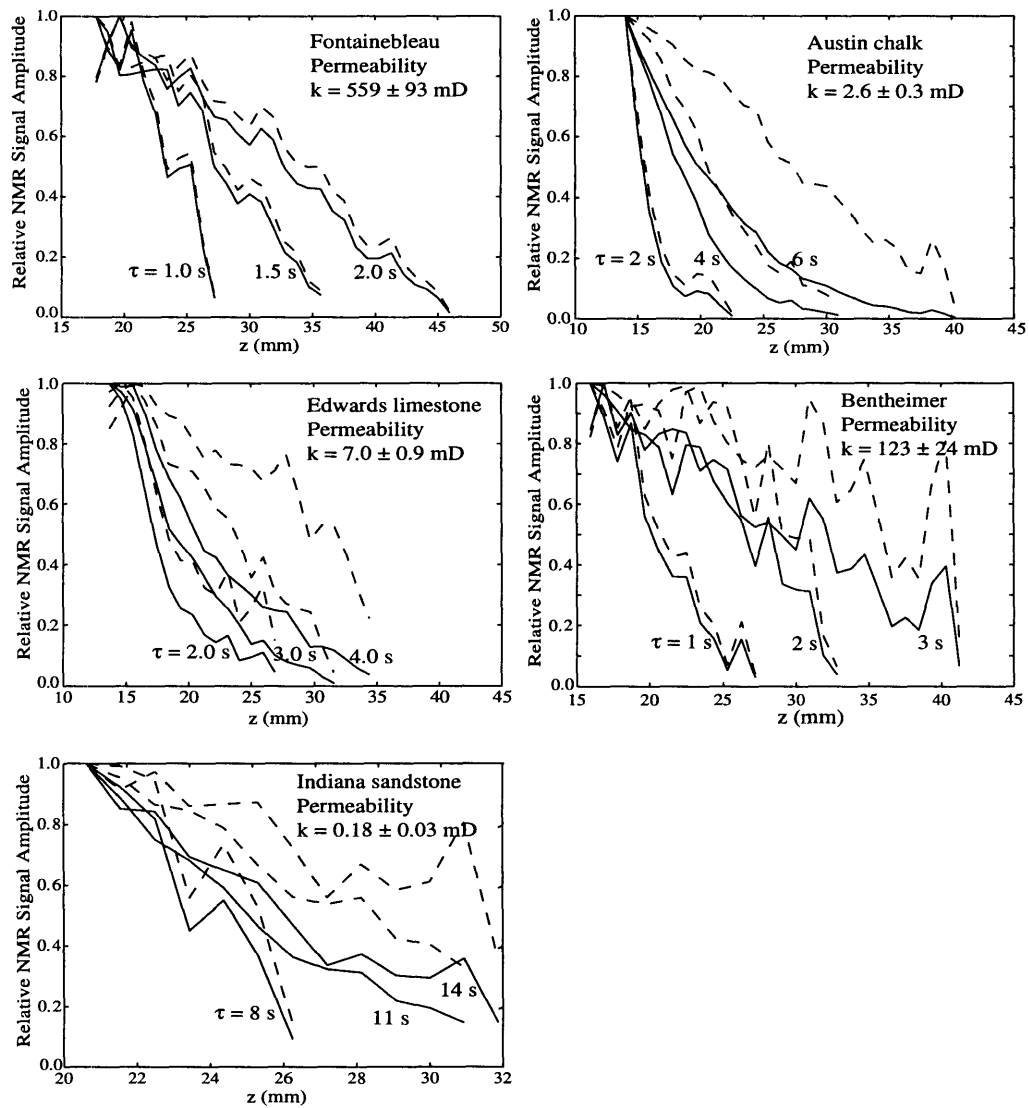
Figure 4-4: ^{129}Xe NMR profiles used in the permeability measurements: (a) Fontainebleau sandstone, (b) Austin Chalk, (c) Edwards limestone, (d) Bentheimer and (e) Indiana limestone. Profiles shown in solid lines correspond to different delay times, τ, following a sequence of RF and gradient pulses to quench all xenon magnetization in the sample. The dash lines are profiles corrected for gas density and polarization variation.

For both the effective porosity and permeability measurements, we corrected for gas density and spin polarization variations as described in the following. We fit the ^{129}Xe NMR profiles from each rock sample, measured with steady-state xenon flow and without prior polarization destruction (e.g., the profiles shown in Fig. 4-3), to Eq. (4.8). From these fits we determined the exponential decay rate, $\frac{2\phi_e\mu}{k\beta}\frac{L}{P_i^2-P_o^2}$. Then, we removed the pressure and spin-relaxation dependence of each profile by dividing S_{rock} (determined at a 1 mm offset from the diffuser-rock interface) by $\frac{1}{P_i}\sqrt{P_i^2 - (P_i^2 - P_o^2)\frac{z}{L}}\exp(-\frac{2\phi_e\mu}{k\beta}\frac{L}{P_i^2-P_o^2}z)$, which is normalized to unity at 1 mm from the entrance of the rock sample. After this correction (see Figs. 3 and 4), profile amplitudes depended only on the fractional volume of the rock occupied by flowing laser-polarized xenon. Table 4.1 lists the permeabilities we determined for the Fontainebleau sandstone, Austin Chalk and Edwards limestone, as well as the permeabilities obtained independently using the gas permeameter. We also include measurement results on the two other rock cores, without comparison measurements with the standard method.

Table 4.1: Permeability and Effective Porosity Results

Sample	Permeability (mD)		Effective Porosity (%)	Absolute Porosity (%)
	LP-Xenon MRI	Gas Permeameter	LP-Xenon MRI	Gas Pycnometer
Fontainebleau	559 ± 93	589 ± 117	11.3 ± 0.7	12.5 ± 0.6
Austin Chalk	2.6 ± 0.3	3.6 ± 0.7	18.4 ± 0.9	29.7 ± 1.5
Edwards limestone	7.0 ± 0.9	4.76 ± 0.95	15.1 ± 1.1	23.3 ± 1.2
Bentheimer	123 ± 24	NA	11.2 ± 1.2	NA
Indiana limestone	0.18 ± 0.03	NA	7.10 ± 0.60	NA

After determining the effective porosity and permeability of each sample, we determined the spin relaxation rate proportionality coefficient, β from the exponential decay rate derived from fitting ^{129}Xe NMR profiles to Eq. (4.8). For the Fontainebleau sample, the ^{129}Xe spin relaxation time (T_1) could therefore be calculated from the nearly constant gas pressure in the sample $(P_i \approx P_o \approx 4.33$ bar), yielding $T_1 = 6.0 \pm 1.0$ s. To test the validity of Eq. (4.8) and the method of profile correction, we measured the ^{129}Xe T_1 directly; we created a sealed container holding a large sample

of Fontainebleau sandstone and thermally-polarized ^{129}Xe at the same gas pressure used in the flowing, laser-polarized gas experiment. The result of 5.6 ± 0.3 s agrees well with the T_1 value derived from the flowing, laser-polarized gas experiment.

As shown in Table 4.1, the permeability values measured with the NMR method are in reasonable agreement with those measured with gas permeameter taking into account the one-standard-deviation uncertainties in these numbers. We therefore conclude that the NMR method provides an accurate measure of permeability.

4.5 Error Analysis

We estimated uncertainties in the NMR measurements of effective porosity and permeability by error propagation of known uncertainties in the directly measurable quantities: NMR signal amplitudes and integrations, gas pressure, dimensions of the samples and diffuser, as well as experimental timings. The uncertainties in rock sample dimensions and NMR experimental timing are on the order of 0.5%, which is negligible compared to that due to the other factors. Here we only consider propagation of errors arising from noise in the NMR signals and uncertainties in the pressure measurements. Next we show as an example the procedure to estimate the uncertainty in the effective porosity.

Eqn. (4.3) describes the calculation of effective porosity value from the cross-sectional area, A, profile signal intensity, S and T_2 in the rock and diffuser, respectively. By ignoring errors in measuring A and t_E, we have the following equation for evaluating error in the effective porosity:

$$\frac{\Delta\phi}{\phi} = \frac{\Delta S_{rock}}{S_{rock}} + \frac{\Delta S_{dif}}{S_{dif}} + \frac{t_E \Delta T_2^{rock}}{(T_2^{rock})^2} + \frac{t_E \Delta T_2^{dif}}{(T_2^{dif})^2}, \qquad (4.10)$$

according to the rule of error propagation [53]. To calculate ΔS, we find n consecutive data points representing pure noise in the profile where no ^{129}Xe signal was present, and ΔS is equal to the standard deviation in the intensity values of the n points. In the same profile, $\Delta S_{rock} = \Delta S_{dif}$. We determine T_2^{rock} by first integrating the portion of the profile corresponding to the rock sample, and then fitting the integral I^{rock} to

79

an exponential. Suppose the length of the rock sample is N, measured in the number of data points in the profile. We then have

$$\Delta I^{rock} = \sqrt{N} \Delta S_{rock}, \qquad (4.11)$$

for the uncertainty in the integrals since the noise-induced fluctuations are not statistically correlated. I is related to time t by the exponential function $I = Ce^{-t/T_2}$, and T_2 is available by least-squares fitting to the following linear relation,

$$\ln\frac{I}{C} = -\frac{t}{T_2}, \qquad (4.12)$$

and the uncertainty in the fitting result is given by (see Appendix E or [53])

$$\Delta T_2 = T_2^2 \sqrt{\frac{1}{\Delta} \sum_{i=1}^{n} \frac{1}{\sigma_i^2}}, \qquad (4.13)$$

where σ_i and Δ are

$$\sigma_i = \frac{\Delta I_i}{I_i}, \qquad (4.14)$$

$$\Delta = \sum_{i=1}^{n} \frac{1}{\sigma_i^2} \sum_{i=1}^{n} \frac{t_i^2}{\sigma_i^2} - \left(\sum_{i=1}^{n} \frac{t_i}{\sigma_i^2} \right)^2,$$

in which I_i are integrals of the profiles measured at time t_i.

Uncertainty in the permeability k is obtained by first estimating errors in the penetration depth, ξ, and the pressure values[2], and then arranging Eqn. (4.9) into a linear relationship between τ and ξ, from which uncertainty in k can be determined through a similar linear-fitting technique to that shown above for the effective porosity.

---

[2]According to the specifications for the pressure sensor, the uncertainty in measured pressure is 0.5 psi.

4.6 Discussions and Conclusions

The laser-polarized noble gas NMR measurement of permeability agrees well with measurements made using the standard gas permeameter technique, for the representative high and low permeability rocks studied so far. For values above 500 mD and below 5 mD, the NMR method yields permeability results that are well within the uncertainty range of the values measured using the gas permeameter, and shows that large variations in the parameters used to determine k, (e.g., output pressure, P_o), do not detract from the measurement. In addition, the effective porosity simultaneously measured by the NMR technique shows that as permeability decreases, the effective porosity measured is a decreasing fraction of the absolute porosity determined by the standard gas pycnometer technique. Effective porosity (i.e., the volume fraction of pore spaces that contribute to fluid flow through the material) is always smaller than the absolute porosity of a sample, and is a parameter that is not easily, nor directly determined with other techniques. The Fontainebleau sandstone has a high permeability due to its well-connected pores with a narrow distribution of sizes, a fact that is consistent with the finding that the sample core has an effective porosity nearly as large as its absolute porosity. Conversely, Austin Chalk and Edwards limestone exhibit effective porosity values that are almost half the values of their absolute porosity, consistent with the knowledge of its very low permeability due to poor pore interconnectivity. The case of Bentheimer sandstone is similar to that of Fontainebleau, where a relatively smaller pore volume, but good pore interconnections are found. The results in Indiana limestone show both low effective porosity and permeability, which could be attributed to a higher resistance to flow due to the narrowed pathways, as well as possible poor inter-pore connections.

To perform NMR imaging of the penetrating inflow of laser-polarized xenon gas, the ^{129}Xe spin decoherence time (T_2) in the rock samples must be sufficiently long ($\sim$ 2 - 5 ms), for a spin echo profile to be obtained without significant signal loss. For the Fontainebleau and Austin Chalk samples, both relatively free of paramagnetic impurities, this condition is easily satisfied, with the measured ^{129}Xe T_2 at 4.7 T

being 4.59 and 12.3 ms in the pores of the Fontainebleau and Austin Chalk, respectively. However, the paramagnetic impurities in many rocks, especially sandstones, will produce large magnetic field gradients when placed in magnetic fields $\geq$ 1 T, these background gradients will significantly shorten the ^{129}Xe T_2. One such example was Berea 100, a macroscopically homogeneous, high-permeability [39] sandstone with a narrow distribution of pore diameters of $\sim$ 100 μm, but with a significant content of paramagnetic particles. In this sample, we were unable to measure a spin echo profile at 4.7 T from inflowing laser-polarized xenon, and hence could not measure the effective porosity or permeability. For such samples, it should be practical to operate at applied magnetic fields $<<$ 1 T for two reasons; (i) the magnetization of laser-polarized noble gas is determined by the optical pumping process external to the applied NMR magnetic field, B_0, i.e., the laser-polarization obtained is independent of B_0, whereas for thermally-polarized samples it is proportional to B_0; and (ii) the magnetic field gradients induced in porous media by magnetic susceptibility variations scale with B_0 and hence are greatly reduced for small B_0. We have previously demonstrated that NMR images of laser polarized noble gas can be acquired at applied field strengths as low as 20 G with resolution and SNR comparable to NMR images obtained at magnetic field strengths $\sim$ 1 T [20, 54]. Low-field NMR of flowing laser-polarized noble gas may allow effective porosity and permeability measurements in a wide array of porous samples using a simple, low-cost electromagnet. In addition to reservoir rocks, this technique may be applicable to ceramics, fluidized beds, filters and partially liquid-saturated porous media [55, 56].

In conclusion, we have demonstrated the simultaneous measurement of permeability and effective porosity of high and low permeability oil-reservoir rock cores using NMR imaging of the penetrating flow of laser-polarized xenon gas. The method is accurate, with permeability results that cover a range of more than two orders of magnitude and agree well with the results from standard techniques. The method is also fast and reproducible: the procedure typically requires about 15 minutes, which is considerably less time-consuming than other NMR-based methods [50] and some standard techniques [41, 42]. The effective porosity measurements are consistent with

expectations: the effective porosity is found to be nearly as large as the absolute porosity for the high permeability Fontainebleau sandstone, and to be significantly smaller than the absolute porosity for lower permeability samples such as Austin Chalk and Edwards limestone.

Chapter 5

Introduction to Gas-Fluidization

5.1 Background

Granular media are collections of small solid particles which are ubiquitous in the food processing industry and nature. These particles are solids, but under certain conditions a collection of them will tend to behave like a liquid. Some examples of granular materials include food products (rice, corn and salt), building materials (sand, gravel and soil) and chemicals (aluminum powder, plastic and pharmaceuticals). Statistics show that in the chemical industry, approximately one half of products and one third of raw materials are granular media [57]. Moreover, it is estimated that tens of billions of dollars are being spent in the industry of particle technology [58]. Diagnosing the dynamics of these materials is relevant to a wide range of scientific and technological problems. Granular chemicals are processed in various kinds of chemical reactors, and the design and performance of these reactors rely significantly on the understanding of the behaviors of the materials under different operating conditions.

Gas fluidization is a process in which solid particles experience fluid-like suspension in a stream of upflowing gas. Five different fluidization may be observed, listed in the order of increasing gas flow rate: fixed bed, homogeneous fluidization, bubbling fluidization, slugging and pneumatic transport [1]. Fig. 5-1 shows the regimes schematically. A fixed bed represents static packed particles, through which gas flows without changing the solid configuration. Homogeneous fluidization is the start of
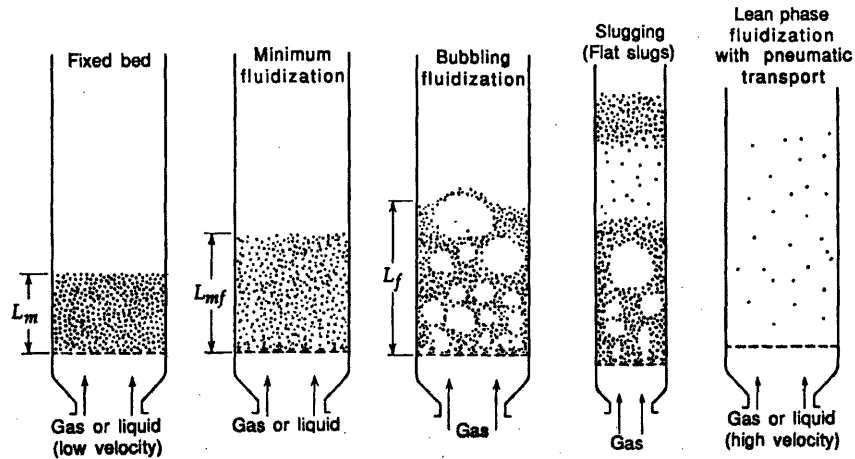
Figure 5-1: Five different fluidization regimes: fixed bed, homogeneous fluidization, bubbling fluidization, slugging and pneumatic transport. Originally found in [1].

particle suspension, initiated when the weight of the particles is balanced by drag forces from the gas, which include viscous drag, inertial drag and buoyancy. Bubbles, or void spaces with volumes much larger than that of single particles, emerge when the gas flow rate is further increased. Two phases exist in a bubbling bed: one is a bubble phase with almost no particles inside, and the other is the remaining solid-gas mixture with a high particle number density, and which is called the emulsion phase. The fast rising bubbles enhance circulation and mixing of particles throughout the bed, in which concentration and temperature gradients can be quickly relaxed. This is the reason why the bubbling regime has been widely applied. Slugging is the term for the regime in which the diameter of the bubbles approaches that of the container, especially for fast flows through a deep particle bed. Pneumatic transport occurs when the flow rate is so high that it continuously pushes the particles along with the gas and out of the bed.

Despite the wide application of fluidization, the understanding of the dynamics of both the solid particles and the gas is far from complete, as such a system is difficult to model numerically, primarily due to the large number of degrees of freedom and inelastic collisions among the particles [2]. Filled up by solid particles, a typical three-

dimensional fluidized granular system is opaque, resulting in difficulties using light scattering or sound waves to experimentally probe the bed behavior deep under its surface [59].

Recently, considerable interest has arisen in studying the behaviors of solid particles in gas-fluidized beds. The question about whether the homogeneously fluidized particles are fluid-like, i.e., they are completely suspended by drag forces from the fluidizing gas or whether they behave like a soft solid in which interparticle stresses exist, has been a matter of debate. Rietema [60] discussed the different types of coherent forces between the solid particles and their effects on the homogeneous bed expansion. Tsinontides and Jackson [61] experimentally determined that the stabilization of homogeneous fluidization was achieved by the presence of yield stresses among the particles. Menon and Durian [62] measured the particle velocity fluctuations by using diffusion-wave spectroscopy (DWS), and observed no particle motions in the homogeneous fluidization regime. They hence concluded that, in this regime, the ensemble of particles was more like a solid, supported by enduring contacts. Valverde *et al.* [63] studied the concentration of fine toner particles ($\sim$ 8.53 μm) under different gas flow conditions, and found that the bed was more solid-like when the gas flow velocity was below a given threshold, while fluid-like behavior such as particle diffusion was observed when the gas flow was above the threshold. However, Foscolo and Gibilaro [64] proposed that the interaction between the particles and the fluidizing gas resulted in the fluid-like suspension of the particles, and they studied the stability of the suspension, as well as its transition into the unstable bubbling regime. In summary, there is no consensus regarding particle motion in the homogeneous fluidization regime, and more experimental evidence, especially with different measurement approaches and different particle sizes and densities, is needed to better understand of the phenomenon. Previous experimental works have investigated the mechanics of the solid particles, but no studies have been conducted to investigate the flow characteristics of the fluidizing gas - which is another crucial factor in the process.

Most commercial fluidized beds operate in the bubbling fluidization regime, in which bubbles emerge at the bottom and expand while rising up along the bed.

Bubbles help to agitate the bed to achieve better mixing, but they also provide a shortcut route for gas to escape the bed without coming in contact with the solid particles [65]. For gas molecules in bubbles to react with the solid phase, they must undergo two processes: transitioning to the emulsion (or interstitial space) from the bubbles, and then migrating to the solid phase, where they are adsorbed. The gas exchange rate is a measure of the efficiency of the contact between the solid and gas phases, and has a significant effect on the operation of the fluidized bed. For example, the reaction rate and yield for a given amount of gas in most chemical reactors is limited by the gas exchange rate; the efficiency of removing moisture in a drying process is also related to the exchange rate. Our aim in this research was to develop a new methodology for measuring gas exchange non-invasively, based on the technologies of NMR and laser-polarization of noble gas.

5.2 Introduction to Fluidized Bed Operations

5.2.1 Components of a Fluidized Bed

A fluidized bed is functionally comprised of four components: the column, gas distributor, particles, and gas flow.

The column is a container that keeps the gas and particles inside its walls and is vertically orientated with openings at both its top and bottom. In industrial practice, the inner surface of the column experiences harsh conditions, and as such it may be either attrited by frequent particle collisions or corroded by reactive species in the bed [1]. In research, the column is often chosen to be transparent so that the bed surface dynamics are easily observed from outside.

A gas distributor is a material with interconnected pores through which the gas flows. Distributors support the particles, and keep the entering gas flow homogeneous in cross-section; they therefore need to be made from a stiff porous material. The criterion for choosing a proper distributor is to make the minimum pore size smaller than the diameter of the smallest particles to prevent the particles from leaking
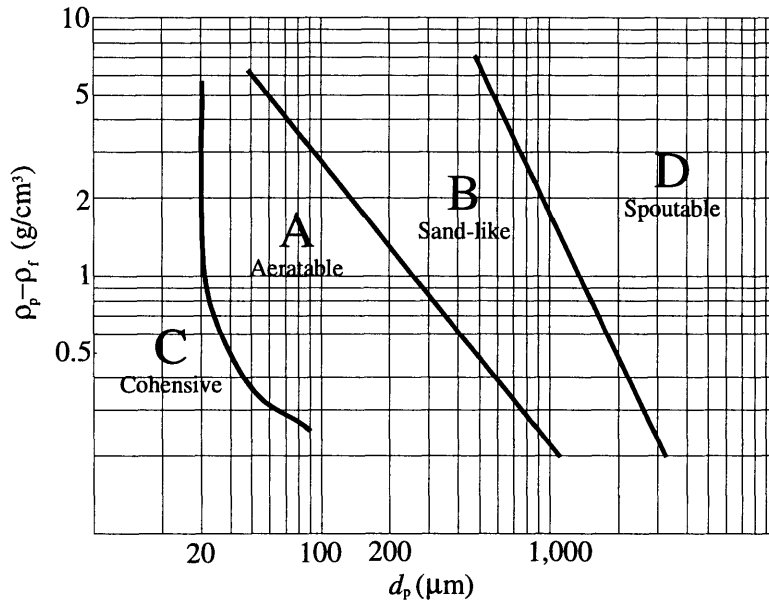
Figure 5-2: Geldart Classification of particles. Four groups of particles are identified according to their fluidization behaviors. d_p is the size of the particles, and ρ_p and ρ_f are density of the particles and gas, respectively.

through. The smaller the pore size, the larger the impedance to gas flow, requiring greater pumping power or back pressure to overcome the pressure drop. The benefit of a high-impedance distributor is a more homogeneous incoming gas distribution, helping to eliminate instabilities and the unpredictability of the bed operations [65].

5.2.2 Particle Classifications

Since the first study of gas-fluidization in 1940's, the focus of research and observation has been on the behaviors of the particles, which are related not only to the way the gas flow is applied, but also to the properties of the particles themselves. D. Geldart systematically studied particle behavior under different fluidization conditions and classified particles into four categories, which are now widely used and referred to as the Geldart Classification [66]. See Fig. 5-2.

Cohesive particles (Group C) cannot be fluidized. Their size is generally less than 20 μm, and the large surface-to-volume ratio leads to strong inter-particle forces,

which originate from various sources such as electrostatic charge, moisture, sticky particle surfaces, soft solid and irregular particle shapes. As a result, the particles move cohesively as the gas flow is aupplied, and the agglomeration of particles is difficult to break. Under certain situations, manual stirring is helpful in slightly fluidizing this category of particles. However, Group C particles are usually not chosen for fluidization.

Areatable particles (Group A) are easily fluidized. They correspond to a relatively small particle size and low density. Homogeneous expansion of the bed is only observed in this category of particles, and considerable bed expansion can occur. Interparticle forces are still large but drag forces from the gas are capable of breaking the particle cohesion. Different fluidization regimes are available and conveniently controlled by adjusting gas flow rate. Most light powders sized below 80 μm belong to this group.

Sand-like particles (Group B), with size between 40 and 500 μm and density between 1.4 and 4 g/cm^3 are widely used for fluidization. The interparticle forces are negligible compared to the larger weight of each particle and stronger interactions with the fluidizing gas. Homogeneous fluidization is not observed with bubbles emerging immediately when the bed is fluidized.

Spoutable particles (Group D) are large and dense, and hence difficult to fluidize. When gas flow is supplied, thin channels appear in the bed, allowing the flow through the particle bed. In the case of strong channelling, erratic particle behavior such as spouting may occur.

Geldart made the phenomenological classification by simply generalizing the bed behavior associated with differences in density and size of the particles. This classification is extremely helpful in choosing the correct type of particles for specific fluidization regimes. However, there is no rigorous theoretical work that quantitatively explains this empirical classification, because of the the complexity of modelling the particle motions and inter-particle forces in such a system.

5.2.3 Homogeneous and Bubbling Fluidization

In this section, the onset of fluidization and particle/gas flow behavior in the two regimes will be covered.

Homogeneous Fluidization

Suppose we have a bed of randomly packed particles belonging to Geldart Group A. Without gas flow, the fixed bed demonstrates no particle motions. If we start to flow gas through at a very slow rate, the particles will not fluidize, but behave like a porous material through which flowing gas flow passes through the interstitial spaces. When the Reynolds number ($Re = \frac{\rho_g U d}{\mu}$) is far less than unity, viscous drag dominates and the relationship between the gas pressure drop, ΔP, and the average flow velocity is linear according to Darcy's law [37]. From the Carman-Kozeny equation [67], which is an extended Darcy equation onto flow through a pack of spherical beads, we have

$$\frac{\Delta P}{H} = \frac{150(1-\epsilon)^2}{\epsilon^3} \frac{\mu U}{d^2},$$

(5.1)

where H is the bed height; ϵ is void fraction, or ratio of interstitial volume to total bed volume (i.e., porosity), which varies between 0.4 and 0.7 with a weak dependence on the size, shape and density of particles; μ is the gas viscosity; U is the superficial or empty tube velocity, the velocity at which the gas would flow in the column if all of the particles were removed while the input flow of gas was kept constant; and d is average particle diameter. [1]

As the gas flow rate increases, the pressure drop ΔP in Eqn (5.1) increases linearly until it equals the total weight of particles divided by the bed cross-sectional area, which is the threshold for incipient fluidization, also called minimum fluidization. This condition can be written as

---

[1]For particles with non-spherical shape, the diameter refers to that of a sphere with the same surface-to-volume ratio as the particles. If mixed-size particles are used, the average diameter is calculated by $1/(\sum_i x_i/d_i)$, in which d_i is the diameter and x_i the weight fraction of particles with such a diameter [65]

$$\rho_p(1 - \epsilon_{mf})g = \frac{150(1 - \epsilon_{mf})^2}{\epsilon_{mf}^3} \frac{\mu U}{d^2}, \qquad (5.2)$$

where ρ_p is particle density; g is gravitational acceleration; and ϵ_{mf} is the void fraction of the bed corresponding to minimum fluidization. The left hand side of represents the weight of the particles divided by total bed volume. The superficial velocity U_{mf} for minimum fluidization is hence

$$U_{mf} = \frac{\epsilon_{mf}^3 \rho_p g d^2}{150(1 - \epsilon_{mf})\mu}, \qquad (5.3)$$

which is useful for estimating the flow velocity needed to start fluidization of spherical particles. In the case of fine powders, Wen and Yu recommended using [68]

$$U_{mf} = \frac{\mu}{d\rho_g} \left[33.7^2 + 0.0408 \frac{d^3 \rho_g (\rho_p - \rho_g)g}{\mu^2} \right]^{1/2} - 33.7, \qquad (5.4)$$

where ρ_g is gas density. This empirical relationship is particularly useful when the particle shape is irregular and void fraction of bed is unknown, but it does not apply to spherical particles.

Homogeneous fluidization starts once the gas velocity is larger than U_{mf}, or when the weight of the particles is completely balanced by the drag forces. If the gas flow velocity increases further, the drag forces will no longer change but be constant and equal to the particle weight. Instead, the particles re-configure, so that the bed of particles does not move. As a result, the interstitial space expands and ϵ_{mf} in Eqn. (5.2) will increase so that the equation still holds.

In homogeneous fluidization, the movement of particles is minimal and such a collection of fluidized particles has been referred to as "weak solid" [62], where enduring inter-particle contacts exist even though the majority of the particle weight is balanced by the gas. The true fluid-like behavior starts only after bubbles are generated.

Bubbling Fluidization

The emergence of bubbles usually starts as a bumpy top surface of the bed, once the flow velocity goes higher than a threshold known as the minimum bubbling velocity, U_{mb}, compared to U_{mf}. It is considerably more difficult to predict U_{mb}, and only empirical relations are available to estimate the value. Geldart and Abrahamsen discovered that U_{mb} is highly dependent on the fraction of particles sized under 45 μm [69].

The shape of a bubble is close to a sphere, except for a concave bottom generated when rising bubbles leave a trailing low-pressure void that is quickly filled by nearby particles. Fig. 5-3 shows a photo of a bubble in a two-dimensional fluidized bed, together with gas flow streamlines calculated from Davidson's bubble model. Note the gas circulation at the two sides, which is caused by the fact that the bubble always rises at a much faster velocity in our experimental conditions (typically 10 times faster) than the gas flow in the emulsion. The volume occupied by the circulating gas is often referred to as a "cloud", in which gas flow is largely impeded by particles. The cloud surrounding the bubble forms a layer between the bubble and the emulsion, which is expected to impede the gas exchange in and out of the bubbles. A cloud layer exists only when the bubble velocity u_b is larger than the gas flow velocity u_f in the emulsion phase. If $u_b < u_f$, no gas cloud will form. In our experiments with fine powders, the flow velocity in the emulsion phase is ~ 1 cm/s while the velocity of any observable bubble (with a diameter larger than the particle size) is above 2 cm/s, resulting in the presence of a cloud layer around any bubble. The ratio of cloud to bubble volume is given by [1]

$$f_c = \frac{2u_f}{u_b - u_f}. \tag{5.5}$$

The calculated cloud volume is 50% of the bubble volume when the bubble size is 0.5 mm, but decreases to 20% as the bubble size increases to 2 mm. For bubbles with a diameter > 0.1 mm, the cloud is much less than the bubble diameter.

The motion of bubbles agitates the otherwise quasi-static homogeneous fluidiza-

93
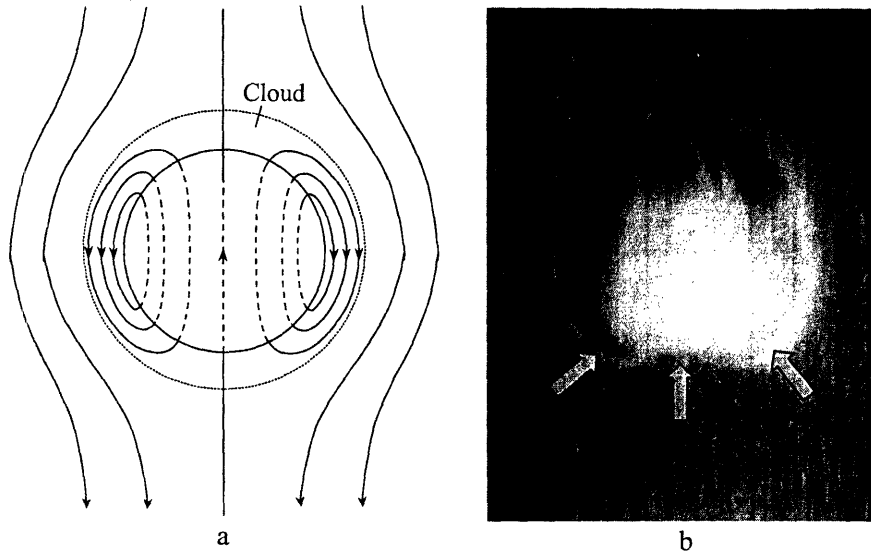
Figure 5-3: Bubble shape and flow streamlines through around bubble. a. Flow streamlines in and out of a bubble (for $u_b > u_f$). The reference frame is that where the bubble is static. b. Photograph of a bubble in a two-dimensional bed, by Davidson and Hurrison in 1971 [2]. The arrows indicate gas flow directions.

tion. The particles are circulated throughout the bed, following the path along which the bubbles rise. Hence most commercial fluidized beds are operated in the bubbling regime in order to achieve better particle mixing.

A list of parameters to characterize the operation of a gas-fluidized bed is given in Table C.1 (Appendix C).

Bubble Rising Velocity

In 1950, Davies and Taylor studied theoretically the velocity of a spherical cap bubble in a Newtonian liquid, and found the bubble velocity, u_b, is related to the bubble radius, r, by [70]

$$u_b = \frac{2}{3}\sqrt{gr},\tag{5.6}$$

where g is the acceleration due to gravity. This equation has been proved to be accurate for gas bubbles rising in a liquid fluid.

However, a similar analysis does not exist for a gas-fluidized bed since the dense

phase may not be considered a Newtonian fluid. Inspired by Eqn. (5.6), Davidson and Harrison [71] recommended the following analogous semi-empirical equation for a bubble in a fluidized bed

$$u_b = 0.711\sqrt{gD_b},\tag{5.7}$$

where D_b is the bubble diameter. Eqn. (5.7) has been widely used to predict the bubble velocity. Experimental results show it provides a reasonably good estimation of u_b [72, 73].

5.2.4 Gas Adsorption

The aluminum oxide particles used in our study are irregularly shaped powders, hence their surface is not smooth solid. Each particle is microporous with the pore sizes ~ 5 μm. The existence of these pores significantly increases the surface-to-volume ratio of the particles, and therefore the contact area between the gas and solid phases is very large. When moving close to the surface of a particle, xenon atoms may temporarily adsorb on the surface [74, 75]. The adsorption results in a chemical shift for the ^{129}Xe spins, and we have observed an adsorption peak about 50 p.p.m. away from the gas peak at room temperature and 2 bar xenon pressure.

Interstitial gas molecules need to diffuse into the micropores located on the particle surface before adsorption occurs. By comparing the length scale of the interstitial space, which is on the order of the particle diameter (~ 100 μm), and that of the micropores (usually < 10 μm), we concluded the exchange between the interstitial gas and microporous gas is primarily limited by the time duration for xenon atoms to traverse the interstitial space. The Peclet number, defined as $Pe = vd/D$ where d is the average size of the particles, v is the interstitial gas velocity, and D is the gas diffusion coefficient, is much smaller than one in our experiments. Therefore, we conclude xenon motion is dominated by diffusion. The diffusive motions are driven by the gradient in chemical potential induced by surface adsorption. The resulting diffusion time may be estimated as $\frac{L^2}{2D}$, in which L is the length scale of interstitial

space, and D is the gas diffusivity. Since L is ~ 100 μm, and D is ~ 3 mm^2/s under our experimental conditions, the exchange time is on the order of 1 ms, and therefore the exchange rate should be $\sim 1,000$ s^{-1}.

The exchange between the microporous gas and adsorbed atoms occurs on a time scale of a few microseconds, which is much faster than the typical NMR time scale[2] [76]. As a consequence, two xenon states exist in the micropores: free gas and adsorbed atoms, and the relative xenon populations of the two determine the observed chemical shift. Mansfeld and Veeman observed the temperature-dependence of the chemical shift of ^{129}Xe adsorbed on Al$_2$O$_3$ fibers [77]. Since the two states are not distinguishable in the NMR experiments, here we name them collectively the adsorption phase.

In conclusion, the exchange rate between interstitial gas and the adsorption phase is primarily limited by how fast gas atoms travel through interstitial spaces and enter micropores. We call this the emulsion-adsorption exchange, with an expected rate of 1000 s^{-1}.

5.2.5 Gas Exchange

A Complete Picture with All Phases

As noted in previous sections, four phases exist in a bubbling fluidized bed: bubble, cloud, emulsion and adsorption. Of these phases, the cloud, emulsion and adsorption are dense, being mixtures of gas and a high density of particles, while no particles exist inside bubbles[3]. Gas exchange between bubbles and the dense phases happens by way of atoms crossing the cloud layer surrounding any single bubble, which is the rate limiting step in the whole exchange process. Diffusion, coherent interstitial gas flow and the circulation of particles promote mixing among the cloud, emulsion and adsorption phases. Fig. 5-4 shows the four phases with possible exchange pathways

---

[2]There could also be strong interaction between xenon and some surface atoms so that the adsorption time is much longer. However, xenon spin magnetization in that state is not replenished, and those atoms are not observable in the experiments.

[3]There is chance that particles may fall into a bubble, but the probability is very low and over 99% of the bubble volume is occupied by gas [1].
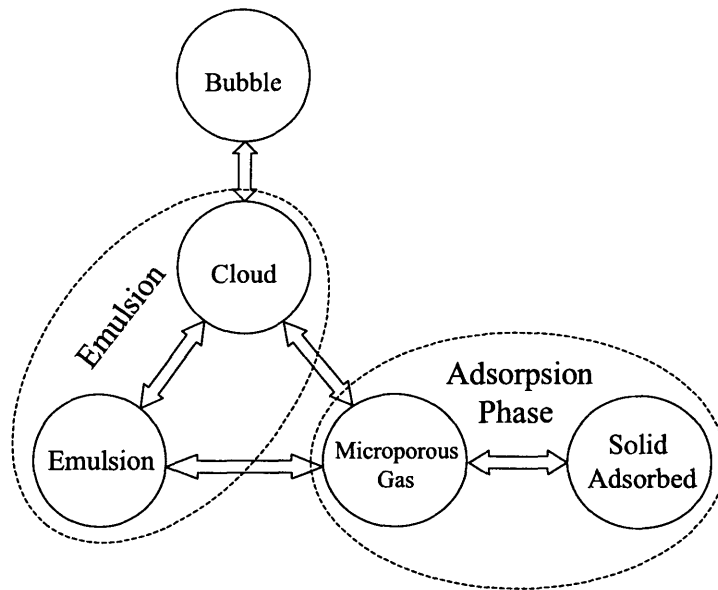
Figure 5-4: Xenon exchange pathways in a bubbling fluidized bed, with all phases included. The exchange between bubble and its encapsulating cloud is the rate-limiting for gas flow from bubble to dense phase.

among them.

As shown in Fig. 5-3, gas flow enters the bubble from the bottom and exits at the top, and the gas flow provides one way for bubble-cloud exchange to occur. Bubble-cloud exchange predominates when the bubble diameter is larger and the particles fluidized are denser and larger. The other mechanism is via random gas diffusion through the bubble boundary. The diffusive exchange is relatively more significant in the case of small bubbles and when highly diffusive gas species are used. Davidson and Harrison recommended that the bubble-cloud exchange rate could be calculated by [71]

$$k_{bc} = 4.5 \left(\frac{U_{mf}}{d_b} \right) + 5.85 \left(\frac{D^2 g}{d_b^5} \right)^{1/4}. \tag{5.8}$$

The first term on the right-hand-side is the contribution from coherent flow, and the second from molecular diffusion. Eqn. (5.8) was derived based on an analogy of mass transfer in and out of a gas bubble rising up in liquids. The shape of the bubble modelled in the calculation is a spherical cap, with a spherical top and a flat bottom. A similar flow stream function to that found for the bubble in a liquid, was used to describe gas flow inside and around the bubble in the fluidized bed. Theoretically, this can be shown by a spatial dependence of tracer concentration in the bubble, which was calculated by balancing the mass transport via diffusion across the streamlines, to that via flow along the streamlines; together with an assumption made about the flow pattern on the spherical bubble top [71]. The exchange rate of gas across the bubble boundary is then equal to the gas flux due to diffusion along the calculated concentration gradient and across the bubble boundary, integrated over the surface of the bubble.

Fig. 5-5 shows the relative contributions from the two exchange mechanisms, calculated from the above equation.

On the other hand, the cloud-emulsion exchange occurs only via gas diffusion through the cloud-emulsion interphase, estimated by Higbie as [78]

98
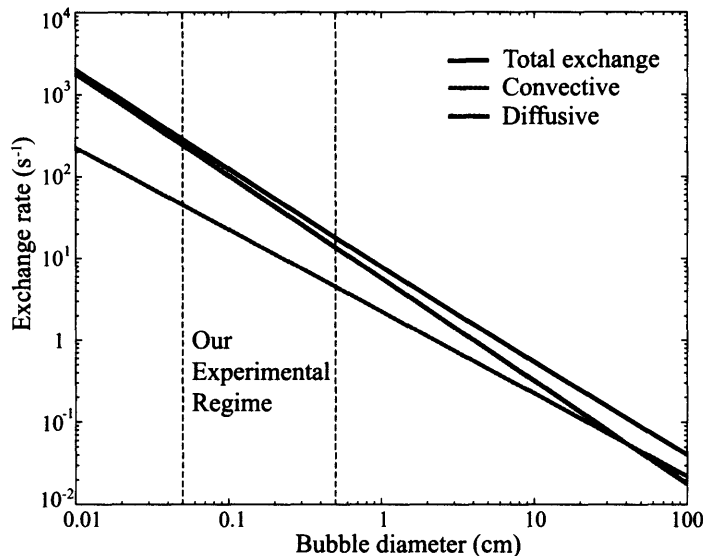
Figure 5-5: Relative contributions to bubble-cloud exchange from the convective and diffusive exchange mechanisms, calculated from Eqn. (5.8) with $U_{mf} = 0.5$ cm/s, and $D = 3$ mm^2/s. Diffusive exchange predominates when the bubble diameter is smaller than 30 cm. In our study, the largest bubble size was 0.5 cm. As a result, we were always observing exchange predominantly due to gas diffusion.

$$k_{ce} = 6.77 \left(\frac{D \epsilon_{mf} u_b}{d_b^3} \right)^{1/2}, \tag{5.9}$$

where u_b and d_b are bubble velocity and diameter, respectively. k_{ce} calculated this way is of the same order as k_{bc} from Eqn. (5.8). The overall exchange rate k_{total}, by considering the two processes together, may be written as [71]

$$k_{total} = 1 / \left(\frac{1}{k_{bc}} + \frac{1}{k_{ce}} \right). \tag{5.10}$$

Experimental mesurements of the bubble-emulsion exchange rate lie between the two values predicted by Eqns. (5.8) and (5.10) [79, 80, 81]. Eqn. (5.9) has been reported to underestimate the cloud-emulsion exchange by ignoring the exchange of gas molecules (or atoms) that move out of the cloud altogether while adsorbed on particles [65]. In clouds, gas flows through the interstitial space with intense contact at the particle surface, where adsorbs significant numbers of molecules are adsorbed which are then carried away from the cloud, as the particles are left behind the faster

rising bubbles. In the case of strong adsorption, this phenomenon enhances the cloud-emulsion exchange to such a degree that the cloud and emulsion phases are effectively indistinguishable [82]. If the cloud-emulsion exchange was nevertheless slower than or on the same order as the bubble-could exchange, a tracer gas concentration in a bubble would demonstrate initial fast decay due to the flow of tracer from the bubble to its cloud, followed by a concentration increase in the bubble since the tracer in the cloud is quickly circulated back into the bubble [83]. As a result, the decay of tracer concentration in the bubble is no longer a simple exponential. From now on, we will treat the cloud and emulsion as a single phase and keep the term "emulsion", and effectively $k_{be} = k_{bc}$ and $k_{ce} = \infty$.

The bubble-emulsion exchange rate was calculated from Eqn. (5.8) to be ~ 100 s^{-1}, for our experimental conditions ($U_{mf} = 0.5$ cm/s, $d_b = 1$ mm, and $D = 3$ mm^2/s). The exchange between adsorbed xenon atoms and the emulsion is much faster than bubble-emulsion exchange, with an estimated time scale of 1 ms. It is therefore legitimate to separate the two processes in studying the exchange phenomenon. When determining the bubble-emulsion exchange rate, the adsorption phase may be included in the emulsion phase since the two are considered to be capable of reaching equilibrium instantly. This effectively means that the emulsion phase has a slightly larger volume to accommodate more xenon atoms due to the addition of micropores on the particle surface. Conversely, when measuring the exchange between the emulsion and the adsorption phase, we consider the bubble-emulsion exchange to be much slower and hence negligible. This separation significantly simplifies the design of the experiments and corresponding rate calculations.

Suppose a bed with particles belonging to Geldart group A or B is fluidized by air flow, and a different tracer gas species, designated as A, is injected from the bottom of the bed as bubbles. The size of the bubbles is controllable by adjusting the bulk flow rate of the injection. Mathematically the exchange rate K between bubbles and the emulsion is defined in the following equation [3]:

$$-\frac{1}{V_b}\frac{dN_{Ab}}{dt} = K\left(C_{Ab} - C_{Ae}\right), \tag{5.11}$$

where V_b is the bubble volume; N_{Ab} is the quantity of injected gas species A inside the bubble; C_{Ab} is gas A concentration in the bubble and C_{Ae} is gas A concentration in the emulsion. The emulsion-adsorption exchange rate is defined in a similar way, being related to the tracer concentrations in the two phases.

5.2.6 Review of Conventional Methods

There have been two types of approaches to quantify the exchange behavior among the different phases in a gas-fluidized bed: numerical simulations and experimental measurements.

The simulation works apply the two-fluid model on the gas-fluidized granular system, by considering the solid phase as the second fluid, in addition to the gas phase, and the hydrodynamical behavior of the two phases are described by the conservation of mass and momentum in each phase, together with the momentum and energy exchange between the two fluids. Additional information about inter-particle stress and internal momentum transfer in the solid phase is not readily available and hence many assumptions are needed in order to solve the problem numerically. The simulation approach is a mathematical challenge due to the large number of degree of freedom in the solid phase, and as a result, the calculations require enormous computational resources. Moreover, the simulation results are ultimately subject to experimental verifications. The most recent simulation work on the bubble-emulsion exchange yielded results in good agreement with Davidson's predictions based on Eqn. (5.8) [71], but it was only able to find the exchange rate between the emulsion phase and a single bubble [83].

During the decade from the late 1960's, there was enormous interest in measuring experimentally the bubble-emulsion exchange rate in three-dimensional beds [80, 81, 84, 85]. In all of these measurements, the bubbles, on which the measurements were performed, were generated by injecting a tracer gas at the bottom of the bed with the rest of the bed in homogeneous fluidization regime, but at a flow rate close to the point where bubbles would emerge. The injected bubbles were isolated from each other and different from the naturally generated ones in another system where the

bed is in bubbling regime, which were small in size at the bottom of the bed and grew bigger as they rose up the bed due to coalescence of multiple adjacent bubbles. The flow patterns of the gas and solid phases induced by the bubble motions differed from that in a regular bed with natural bubbles. Two different methods were used to measure the exchange between these injected bubbles and the emulsion phase. Stephens *et al.* [80] used a sampling tube to probe the tracer concentration in the emulsion phase at different heights along the bed axis, from which they derived the amount of gas exchange while the bubbles rose up in the bed. The procedure did not account for the radial concentration gradient resulting from gas exchange out of the bubbles, and as such, a significant systematic error exists in their results. Moreover, the invasive probe tended to obstruct the flow path of the gas and particles, and inevitably disturbed the bed operations, which may have caused unpredictable effects on the exchange process. The second method was proposed by Chiba *et al.* [81], in which an ultraviolet probe and spectrometer were used to detect tracer concentration in the bubbles. The probe was installed in the bed so that there was a 1 cm gap at the center of the probe to let bubbles pass through. This method was also invasive, since the probe was installed inside the bed, and specifically it obstructed emulsion flow, as well as disturbing bubble motion due to its close proximity to the bubbles. In addition, they only measured the tracer concentration at a single point inside the bubble, which was then assumed to be the tracer concentration in the entire bubble. This assumption has been proved to be incorrect by later simulations [83].

Two additional limitations exist in the these measurements. First, they do not account for the effect of the presence of multiple bubbles on the exchange rate. In a natural bubbling bed, bubbles may interact with each other via frequent coalescence and splitting, which may enhance the bubble-emulsion exchange rate. Secondly, the size of the bubbles and their rising velocity were considered constant, which is generally incorrect. Bubbles provide a pathway for gas to flow through the bed with less resistance, compared to the emulsion phase where large number of particles exist. Consequently, the bubbles tend to expand by taking up emulsion gas, while rising up through the bed [83, 85]. The increased bubble diameter results in a larger bub-

ble velocity. During the subsequent 30 years, no significant improvements have been made on the experimental methodology.

The mass exchange between the gas and the solid particles is the second parameter affecting the performance of a fluidized bed. It characterizes how efficiently the gas molecules contact the solid surface, where the actual reaction happens. From the early 1950's to 1970's, there were several experimental studies that measured the gas-solid exchange rate by using various types of gas and particles [86, 87, 88, 89]. The method used in these studies is to introduce particles containing a removable tracer material into a fluidized bed without any tracer initially. The tracer could leave the solid phase by any of the following ways: sublimation, vaporization or release from adsorption. The gas-solid exchange rate was measured by observing the tracer concentrations in the inlet and outlet gas for the entire bed. This method, however, was not able to provide information on the spatial dependence of the tracer concentration along the bed. The method also relied on various assumptions and empirical relations associated with bubble flow and gas exchange between bubbles and the emulsion phase. Additionally, the preparation and conduct of these experiments were extremely tedious and time-intensive. Moreover, no reported work of which we are aware has been found that measures both the bubble-emulsion and emulsion-solid exchange rates simultaneously.

Our experimental approach uses the NMR technique to non-invasively measure the mass exchange rates among the different phases, including the bubble, emulsion and adsorption phases in a gas-fluidized bed. The fast method developed in this study enables us to probe the exchange behavior between the emulsion phase and multiple, naturally generated bubbles, without assuming constant bubble diameter or homogeneous tracer concentration inside the bubble. It also allows us to simultaneously measure the exchange rate between the emulsion gas and the solid phase, which is distinguished by the large chemical shift due to the adsorption of xenon atoms.

103

5.2.7 The NMR Model

If we use spin magnetization, instead of injected gas concentration, the exchange behavior may be equivalently described through the dynamics of the longitudinal spin magnetization. Exchange occurs between bubbles and the emulsion phase, and between the emulsion and adsorption phases. There is no direct exchange between the bubbles and the adsorption phase, since the layer of gas around any single particle belongs to the emulsion phase, and hence the gas molecules in bubbles need to traverse the emulsion phase before they can be adsorbed. The gas flow and particle motions were in the steady state. We minimized transient and unstable bed behavior by supplying a steady and homogeneous gas flow from the bottom of the column, and also by locating the RF coil at a high level up the bed so that the region from the bed bottom to the RF coil is as long as possible. Moreover, the steady state condition was guaranteed by extensive signal averaging, to smooth out the effects of any remaining oscillatory flow behavior.

Spin magnetization may be manipulated with RF pulses and prepared in an initial condition that can reveal their time-dependent motion in steady-state flow. The temporal and spatial dependence of magnetization in the three phases can be written as[4]

$$
\begin{aligned}
\frac{\partial M_b}{\partial t} + u_b \frac{\partial M_b}{\partial z} &= -k_{be}(M_b - M_e) - \frac{M_b - M_b^0}{T_1^b} \\
\frac{\partial M_e}{\partial t} + u_e \frac{\partial M_e}{\partial z} &= -\frac{\psi_b}{\psi_e} k_{be}(M_e - M_b) - k_{ea}(M_e - M_a) - \frac{M_e - M_e^0}{T_1^e} \quad (5.12) \\
\frac{\partial M_a}{\partial t} &= -\frac{\psi_e}{\psi_a} k_{ea}(M_a - M_e) - \frac{M_a - M_a^0}{T_1^a}
\end{aligned}
$$

Table (5.1) lists all the variables and their corresponding descriptions. These equations relate the material derivatives of spin magnetization in a fluid element along the gas flow to different factors causing changes in their values. As an example, from the equation for the dynamics of the emulsion magnetization, the term $-\frac{\psi_b}{\psi_e} k_{be}(M_e - M_b)$

---

[4]Clouds have been lumped into the emulsion phase.

104

Table 5.1: Descriptions of Variables Used in Eqn. (5.12)

Variable	Description
M_b	Bubble magnetization
M_e	Emulsion magnetization
M_a	Adsorption magnetization
M_b^0	Bubble magnetization at thermal equilibrium
M_e^0	Emulsion magnetization at thermal equilibrium
M_a^0	Adsorption magnetization at thermal equilibrium
u_b	Bubble velocity
u_e	Gas flow velocity in the emulsion phase
ψ_b	Ratio of bubble volume to total bed volume
ψ_e	Ratio of emulsion gas volume to total bed volume
ψ_a	Ratio of micropore gas volume to total bed volume
T_1^b	T_1 in bubble phase
T_1^e	T_1 in emulsion phase
T_1^a	T_1 in adsorption phase
k_{be}	Bubble-emulsion exchange rate
k_{ea}	Emulsion-adsorption exchange rate

originates from the bubble-emulsion exchange; $-k_{ea}(M_e - M_a)$ is due to the emulsion-adsorption exchange; while $-\frac{M_e - M_e^0}{T_1^e}$ arises from T_1 relaxation in the emulsion phase. The gas velocity in the adsorption phase is zero since there is no net particle flow in the steady state[5]. The volume ratios ψ_b, ψ_e, ψ_a are introduced to account for different gas volumes in the three phases. These three equations are extensions from Bloch's Equation (2.11) to accommodate the exchange behavior as well as convective gas flow.

The Xe NMR signal is sensitive to the volume integral of magnetization in the sensitive region of the RF coil. We define the total magnetization, $\mathfrak{M}_p$, corresponding to a phase labelled p as

$$\mathfrak{M}_p = \iiint M_p dV_p = \psi_p \iiint M_p dV = \psi_p A \int_{z_1}^{z_2} M_p dz, \qquad (5.13)$$

---

[5]The circulation of particles throughout the bed causes mixing of the adsorption magnetization along the bed axis. However, since the particles are much less mobile compared to gas flow with net particle flow being zero, we neglect the adsorption-phase flow term and considered the temporal and spacial dependence of M_a to be completely determined by the emulsion-adsorption exchange.

where ψ_p is volume ratio in phase p; A is the bed cross-sectional area; z_1 and z_2 are the starting and ending positions marking the sensitive region of the RF coil; V is total bed volume and V_p is the volume occupied by the phase. This representation is one-dimensional along the flow direction, since distributions of the phases are considered homogeneous in cross section [65]. Assuming the gas velocity in the bubbles and emulsion phase do not change, we have the volume integral $\iiint dV$ on both sides of Eqns. (5.12) as

$$
\begin{aligned}
\frac{1}{\psi_b}\frac{d\mathfrak{M}_b}{dt} + u_b(M_b|_{z_2} - M_b|_{z_1}) &= -k_{be}\left(\frac{\mathfrak{M}_b}{\psi_b} - \frac{\mathfrak{M}_e}{\psi_e}\right) - \frac{\mathfrak{M}_b - \mathfrak{M}_b^0}{T_1^b \psi_b} \\
\frac{1}{\psi_e}\frac{d\mathfrak{M}_e}{dt} + u_e(M_e|_{z_2} - M_e|_{z_1}) &= -\frac{\psi_b}{\psi_e}k_{be}\left(\frac{\mathfrak{M}_e}{\psi_e} - \frac{\mathfrak{M}_b}{\psi_b}\right) - k_{ea}\left(\frac{\mathfrak{M}_e}{\psi_e} - \frac{\mathfrak{M}_a}{\psi_a}\right) \\
&\quad - \frac{\mathfrak{M}_e - \mathfrak{M}_e^0}{T_1^e \psi_e} \qquad\qquad\qquad (5.14) \\
\frac{1}{\psi_a}\frac{d\mathfrak{M}_a}{dt} &= -\frac{\psi_e}{\psi_a}k_{ea}\left(\frac{\mathfrak{M}_a}{\psi_a} - \frac{\mathfrak{M}_e}{\psi_e}\right) - \frac{\mathfrak{M}_a - \mathfrak{M}_a^0}{T_1^a \psi_a}.
\end{aligned}
$$

In the NMR measurement of bubble-emulsion exchange, we initialized the magnetization so that at $t = 0$, polarized gas resided only in the region from the bottom of the RF coil to the center of the RF coil. We also made sure that the front of the gas flow did not reach the top of the coil during the measurement time. (See Section 6.3 for detail) Moreover, we used the phase-cycling NMR technique to cancel the effects due to the advance of polarized gas into the RF coil region during the measurement by averaging over multiple scans with alternating polarity in the freshly entering magnetization. In the emulsion-adsorption exchange measurement, the amount of gas flowing in or out of the RF coil only contributes to $\sim 0.2\%$ of the RF coil sensitive region during the measurement time. The inflow and outflow terms in the above equations can therefore be ignored.

We performed ^{129}Xe T_1 measurement on a valved glass cell of aluminum oxide particles, with the interstitial space filled by enriched ^{129}Xe to 3 bars. Emulsion and adsorption peaks were clearly resolved, and we were able to perform a T_1 measurement on them separately using the saturation recovery technique [90]. As a result, we

106

observed the same relaxation time in the two phases,

$$T_1^{obs} = 44.0 \text{ s,} \tag{5.15}$$

due to the fast exchange between them. The observed relaxation time is related to the intrinsic T_1's in these two phases, T_1^e in the emulsion and T_1^a in the adsorption phase, by

$$\frac{1}{T_1^{obs}} = \frac{\alpha}{T_1^e} + \frac{1-\alpha}{T_1^a}, \tag{5.16}$$

where α is the fraction of xenon in the emulsion phase. From Eqn. (5.16), we immediately get $T_1^e > \alpha T_1^{obs}$ and $T_1^a > (1-\alpha)T_1^{obs}$. The value of α was measured to be 0.612 (see section 6.4.2, where $\alpha = \psi_e/(\psi_e + \psi_a)$), and we therefore can define lower limits for T_1 in the emulsion and adsorption phases:

$$T_1^e > 26.9 \text{ s and } T_1^a > 17.1 \text{ s.} \tag{5.17}$$

T_1^b is not directly measurable but it should be comparable to that of bulk xenon, which is at least on the order of tens of minutes. Compared to exchange rates $k_{be} \sim 100 \text{ s}^{-1}$ and $k_{ea} \sim 1{,}000 \text{ s}^{-1}$, T_1 relaxation times for the three phases are much slower and may thus be safely neglected. Based upon the above conditions, the dynamics of the magnetization vectors $\mathfrak{M}$'s can be simplified as

$$\begin{aligned}
\frac{d\mathfrak{M}_b}{dt} &= -k_{be}\left(\mathfrak{M}_b - \frac{\psi_b}{\psi_e}\mathfrak{M}_e\right) \\
\frac{d\mathfrak{M}_e}{dt} &= -k_{be}\left(\frac{\psi_b}{\psi_e}\mathfrak{M}_e - \mathfrak{M}_b\right) - k_{ea}\left(\mathfrak{M}_e - \frac{\psi_e}{\psi_a}\mathfrak{M}_a\right) \\
\frac{d\mathfrak{M}_a}{dt} &= -k_{ea}\left(\frac{\psi_e}{\psi_a}\mathfrak{M}_a - \mathfrak{M}_e\right).
\end{aligned} \tag{5.18}$$

Bubble-Emulsion Exchange

Assuming time-independent ψ_b, ψ_e and ψ_a, with initial condition of

107

$$\mathfrak{M}_b(0) = \mathfrak{M}_b^0, \quad \mathfrak{M}_e(0) = \mathfrak{M}_a(0) = 0, \tag{5.19}$$

Eqn. (5.18) has the following solution for the bubble magnetization:

$$\mathfrak{M}_b(t) = Ae^{-\lambda_1 t} + Be^{-\lambda_2 t} + C, \tag{5.20}$$

where

$$\lambda_{1,2} = -\frac{1}{2}\left[k_{ea}(1 + \frac{\psi_e}{\psi_a}) - k_{be}(1 + \frac{\psi_b}{\psi_e})\right] \pm \frac{1}{2}K, \tag{5.21}$$

and

$$A = -\frac{k_{be}(1 + \frac{\psi_e}{\psi_a} - \frac{\psi_b}{\psi_e} + \frac{\psi_b}{\psi_a}) - k_{ea}(1 + \frac{\psi_e}{\psi_a})^2 - K(1 + \frac{\psi_e}{\psi_a})}{2K(1 + \frac{\psi_e}{\psi_a} + \frac{\psi_b}{\psi_a})}\mathfrak{M}_b^0$$

$$B = \frac{k_{be}(1 + \frac{\psi_e}{\psi_a} - \frac{\psi_b}{\psi_e} + \frac{\psi_b}{\psi_a}) - k_{ea}(1 + \frac{\psi_e}{\psi_a})^2 + K(1 + \frac{\psi_e}{\psi_a})}{2K(1 + \frac{\psi_e}{\psi_a} + \frac{\psi_b}{\psi_a})}\mathfrak{M}_b^0,$$

$$C = \frac{\psi_b}{\psi_b + \psi_e + \psi_a}\mathfrak{M}_b^0.$$

In the above equations, the symbol K is

$$K = \sqrt{\left[k_{ea}(1 + \frac{\psi_e}{\psi_a}) - k_{be}(1 + \frac{\psi_b}{\psi_e})\right]^2 + 4k_{be}k_{ea}\frac{\psi_b}{\psi_e}}.$$

If the exchange rate between the emulsion and adsorption phases is much faster than that between the bubble and emulsion phases and the following condition is true,

$$k_{ea}(1 + \frac{\psi_e}{\psi_a}) \gg k_{be}(1 + \frac{\psi_b}{\psi_e}), \tag{5.22}$$

a Taylor-expansion of K yields the first order approximation,

$$K \simeq k_{ea}(1 + \frac{\psi_e}{\psi_a}) - k_{be}(1 + \frac{\psi_b}{\psi_e}) + 2k_{be}\frac{\frac{\psi_b}{\psi_e}}{1 + \frac{\psi_e}{\psi_a}}. \tag{5.23}$$

Plugging the approximated K value into Eqn. (5.21), we have the following exponential decay rates,

$$
\begin{aligned}
\lambda_1 &= k_{be}(1 + \frac{\psi_b}{\psi_e + \psi_a}) \\
\lambda_2 &= k_{ea}(1 + \frac{\psi_e}{\psi_a}),
\end{aligned}
\tag{5.24}
$$

with $\lambda_2 \gg \lambda_1$, according to the assumption in Inequality (5.22), which was verified by experimental results presented in the next chapter. Moreover, the following coefficients are available for the solution given in Eqn. (5.20):

$$
A \simeq \frac{\psi_e + \psi_a}{\psi_b + \psi_e + \psi_a}\mathfrak{M}_b^0, \quad B \simeq 0 \text{ and } C \simeq \frac{\psi_b}{\psi_b + \psi_e + \psi_a}\mathfrak{M}_b^0.
\tag{5.25}
$$

If the bubble-emulsion exchange is measured over a time t that is long, so that $e^{-\lambda t} \ll 1$, the results can then be fitted to the following simple exponential

$$
\mathfrak{M}_b(t) = \left[\frac{\psi_e + \psi_a}{\psi_b + \psi_e + \psi_a} e^{-k_{be}(1 + \frac{\psi_b}{\psi_e + \psi_a})t} + \frac{\psi_b}{\psi_b + \psi_e + \psi_a} \right]\mathfrak{M}_b^0,
\tag{5.26}
$$

to extract the decay rate and k_{be}.

Emulsion-Adsorption Exchange

Emulsion-adsorption exchange may be treated similarly, under initial conditions of

$$
\mathfrak{M}_b(0) = 0, \quad \mathfrak{M}_e(0) = \mathfrak{M}_e^0 \quad \mathfrak{M}_a(0) = \mathfrak{M}_a^0.
\tag{5.27}
$$

By using the same assumption in Inequality (5.22), solution to Eqn. (5.18) can be simplified to

$$
\begin{aligned}
\mathfrak{M}_e(t) &= \frac{\psi_e(\mathfrak{M}_a^0 + \mathfrak{M}_e^0)}{\psi_a + \psi_e} + \frac{\psi_a\mathfrak{M}_e^0 - \psi_e\mathfrak{M}_a^0}{\psi_a + \psi_e}e^{-k_{ea}(1 + \frac{\psi_e}{\psi_a})t} \\
\mathfrak{M}_a(t) &= \frac{\psi_e(\mathfrak{M}_a^0 + \mathfrak{M}_e^0)}{\psi_a + \psi_e} - \frac{\psi_a\mathfrak{M}_e^0 - \psi_e\mathfrak{M}_a^0}{\psi_a + \psi_e}e^{-k_{ea}(1 + \frac{\psi_e}{\psi_a})t}
\end{aligned}
\tag{5.28}
$$

If proper initial conditions are generated as shown in Eqns (5.19) and (5.27), we are able to measure the exponential decay rates of the bubble and adsorption magnetization, from which the exchange rates k_{be} and k_{ea} may be calculated by fitting data to the above two groups of solutions.

5.3   Conclusion

In conclusion, gas-fluidization is a complicated process that has been widely applied in various industrial fields. The understanding of particle and gas dynamics in fluidized granular systems is still under development. Our approach is to probe flow and exchange dynamics by using hyperpolarized noble gas NMR, which has been successful in studying gas flow in fixed porous media but never in fluidized granular media before. The exchange behavior among the different phases has been described by using the dynamics of the longitudinal magnetization in different phases. We will use this description as an experimental model to measure the inter-phase exchange rates in next chapter.

Chapter 6

NMR Study of Gas Dynamics in Gas-Fluidized Granular Media

This chapter presents an NMR study of gas dynamics in a particle bed fluidized by laser-polarized xenon gas. Previous NMR measurement of granular systems primarily concentrated on the dynamics of the solid particles [91], which convey no direct information about the gas dynamics. Direct NMR detection of the flowing gas will reveal fundamental information about the gas dynamics, but the low signal-to-noise ratio (SNR) obtained from thermally-polarized gases has made such measurements unfeasible. To address the problem of low SNR in gas-phase NMR, we use the spin-exchange optical pumping method [92] to enhance the nuclear spin polarization of ^{129}Xe gas by 3 - 4 orders of magnitude (compared to that available from the Boltzman distribution), producing a magnetization which can be as high as water samples at magnetic field of ~ 1 tesla. Our group has shown that in such as system, detailed studies of gas flow dynamics in a variety of media is possible [21, 93, 94]. In this chapter, we report results of variation in granular bed behavior in different fluidization regimes. These are the first measurements to use NMR to non-invasively probe the emulsion gas and gas bubbles; and to measure the exchange rates between the bubble, emulsion, and adsorption phases.

Two important parameters, the inter-phase gas exchange rates, and the gas velocity distributions in the particle bed have been measured in our research. Aluminum
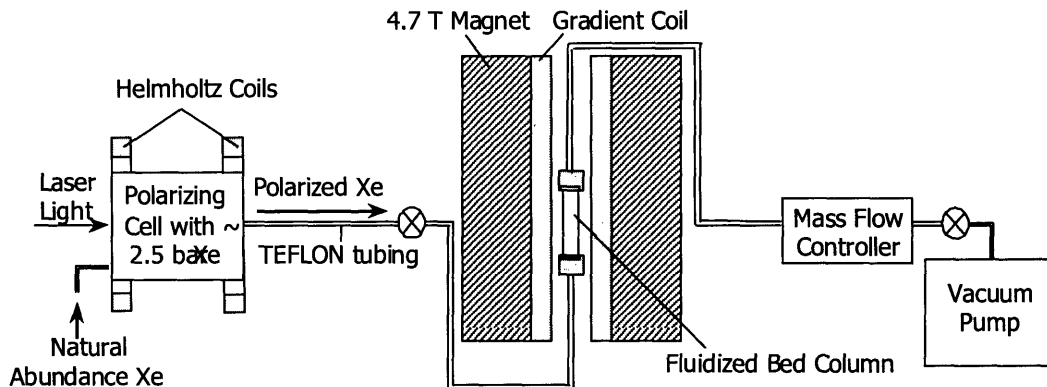
Figure 6-1: A schematic diagram of the Laser-polarized xenon - fluidized bed - NMR apparatus. Narrow 1/8 inch ID Teflon tubing connected the different sections of the apparatus, and provided the gas flow path. The tubing length was approximately 2.5 m from the polarizer to the sample, and 5 m from the sample to the mass flow controller. The mass flow controller moderated the effect of the pump and determined the gas flow in the particle bed.

oxide (Al_2O_3) powders have a microporous surface that promotes xenon adsorption, and this feature allows us to study the gas exchange between the emulsion and the adsorption phases, in addition to gas exchange between the bubbles and emulsion. The large magnetic susceptibility of the Al_2O_3 particles and their irregular shape allows us to differentiate xenon bubbles from the emulsion and adsorption phases in NMR spectroscopy using a T_2-contrast method. Additionally, the large ^{129}Xe chemical shift range allows the adsorption phase to be distinguished from the free gas. Our experimental results demonstrated that the contrast methodology was successful in distinguishing the various gas phases, and the exchange rates measured by this technique agree well with predictions from available models. We also measured the gas velocity distribution using the pulsed-field-gradient method, which yielded velocity distributions that clearly show the onset of bubbling and indirectly describe particle motion in the fluidized bed.

6.1 Experimental Apparatus

6.1.1 Overview

Fig. 6-1 shows a schematic of the complete experimental apparatus. Xenon gas (26.4% ^{129}Xe) was spin-polarized in a glass cell which contained a small amount of Rb metal. The total gas pressure was 2.5 bar, with the mixture consisting of 95% xenon and the remainder N_2. The cell was heated to 130°C to create an appropriate Rb vapor density to ensure spin polarization of the Rb vapor via optical pumping on the Rb D1 line ($\sim$ 795 nm). Circularly-polarized light for optical pumping was supplied from $\sim$ 30 W of broad-spectrum ($\sim$ 2 nm) light provided by a fiber-coupled laser diode array. In a few minutes Rb-Xe collisions boost the ^{129}Xe spin polarization to $\sim$ 1% according to the calibration measurement mentioned in Chap 2.

Xenon gas flows from the polarizer through 1/8" I.D. Teflon tubing to the gas-fluidized bed, with a pressure potential supplied by a vacuum pump located at the end of flow path. The gas flow rate was regulated by a mass flow controller placed just before the vacuum pump, which was capable of regulating steady flows ranging from 10 to 1000 cm^3/s. A continuous supply of polarized xenon gas, at a controlled flow rate of 50-200 cm^3 per minute (sccm), fluidizes the particle bed which is located in an NMR magnet. The xenon gas pressure in the particle bed was measured to be $\sim$ 2.0 bar.

6.1.2 Fluidized Bed

As shown in Fig. 6-2, the fluidized bed setup used in the experiments consisted of an 6 mm I.D. cylindrical Pyrex column, a windbox and two gas diffusers made of porous Polyethylene (Porex Corp.) with a pore size of 2 micron. The windbox, with its large volume, provided a buffer for the gas flow from the polarizer and the column. On top of the windbox is the first gas diffuser, which ensures the vertical gas flow is homogeneous in cross-section. The Pyrex column, located above the diffuser, served as the container of the bed particles. A second diffuser covered the top of the column

113
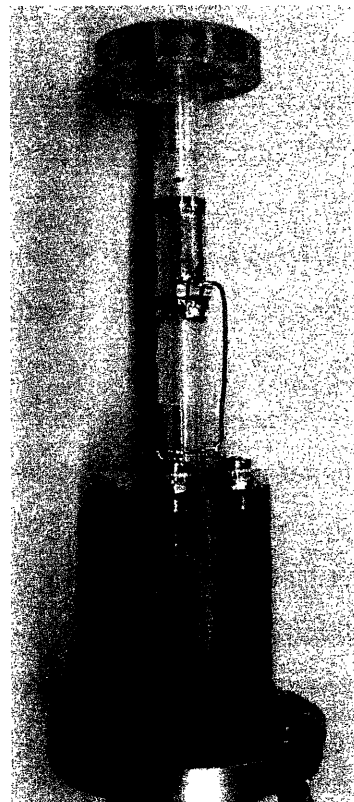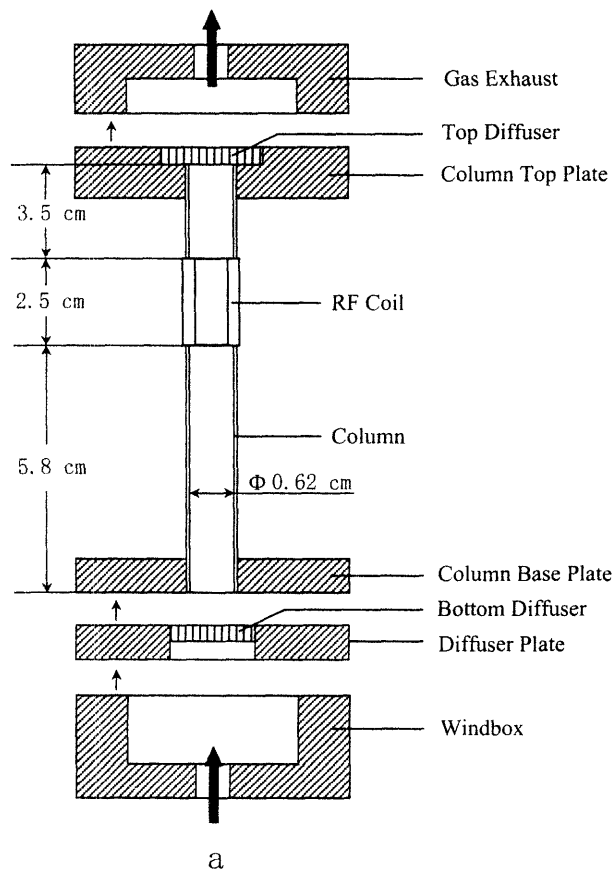
Figure 6-2: Complete assembly of the fluidized bed apparatus. a) Schematic drawing; b) Photo of the actual assembly without the exhaust region in place. The connections between the different plates are sealed by O-rings. The bottom diffuser is mounted with a retention ring onto the diffuser plate, while the top diffuser is glued to the column top plate. At the bottom of the plate, the mounting of the apparatus onto the NMR micro-imaging probe body is visible.

a   b
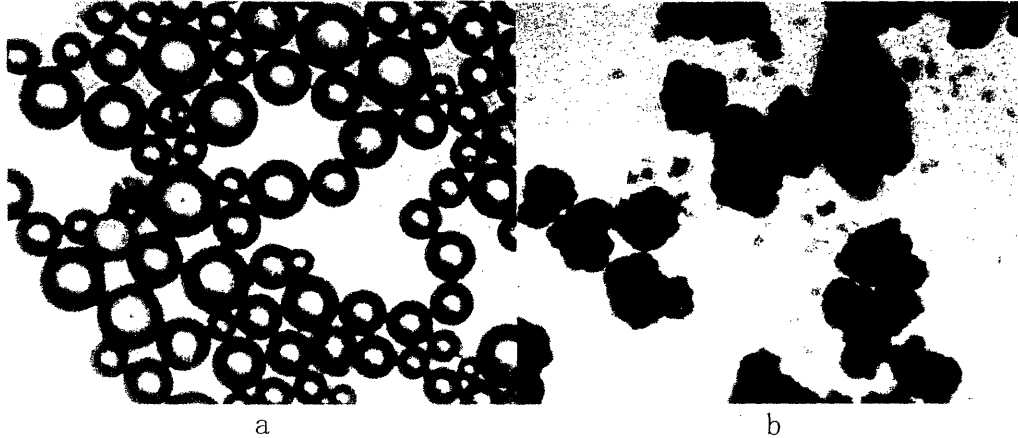
Figure 6-3: Photos of the particles used in the fluidized-bed experiments, taken with 100x microscope. a) Transparent glass beads sized between 45 and 70 μm, which results in them being classed as Geldart Group A particles. The beads are highly spherical in shape. b) Opaque Al_2O_3 particles, sized between 75 and 104 μm, by passing through appropriate sieves. These particles are classed as Geldart Group B and their shape is highly irregular.

to stop particles being carried out with the gas. The whole apparatus was assembled with non-metallic materials to minimize spin depolarization of the laser-polarized xenon gas transport. The fluidized bed apparatus was built on a standard vertical-bore NMR micro-imaging probe body, to ensure accurate placement in the NMR magnet. The probe body and connecting gas transport tubing was then positioned in a 4.7 T vertical bore magnet, interfaced to a Bruker AMX2-based NMR console.

6.1.3 Particles

We chose two types of particles for this work: 45 $\sim$ 70 μm glass beads and 75 $\sim$ 104 μm aluminum oxide (Al_2O_3) powders[1]. Photo-micrographs of these particles are shown in Fig. 6-3.

The glass beads are spherical while the shape of the Al_2O_3 particles is highly irregular. The magnetic susceptibility of diamagnetic aluminum oxide is -37×10^{-6}

---

[1] The vendor of the glass beads is Jaygo Inc. The aluminum oxide powders were manufactured by EM Science, with a part number of AX0612-1, and CAS number of 1344-28-1.
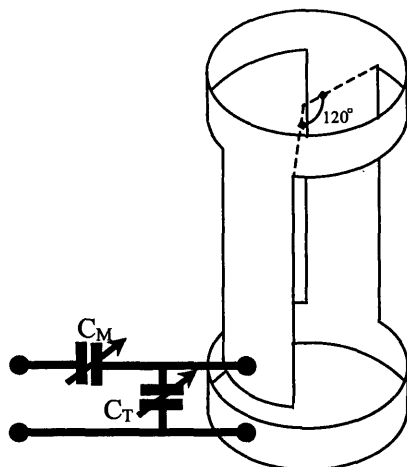
Figure 6-4: Alderman-Grant RF Coil. The 120° RF windows were chosen for optimal field homogeneity. C_T and C_M are tuning and matching capacitors which can be adjusted for optimal sensitivity at the ^{129}Xe Lamor frequency.

cm^3/mol, 25% larger than the value of magnetic susceptibility of glass. However, the measured NMR linewidths of ^{129}Xe flowing through the interstitial spaces of the two types of particles are contrastingly different, with that from Al_2O_3 particles being 650 Hz (11.7 p.p.m.) while that from glass beads is on the order of 100 Hz (1.8 p.p.m.). The irregularity in the shape of Al_2O_3 powders, which tends to introduce a stronger heterogeneity in the magnetic field surrounding the particles, is likely the origin of the broad linewidth.

6.1.4 Radio-Frequency Coil

Around the column is a homebuilt Alderman-Grant style RF coil [95], the design of which is shown in Fig. 6-4. Copper foil tape was glued onto a 1/2" o.d. Teflon tube to form the shape of the coil, and the tube made a tight fit around the fluidized bed column. Although Alderman-Grant coils are not the best choice in terms of field homogeneity across their total volume, since only their 60% is uniform, they are sufficient for our experiments because the inner radius of the fluidized bed column is less than 50% of the coil radius. The total sensitive length of the coil is 2.4 cm, which
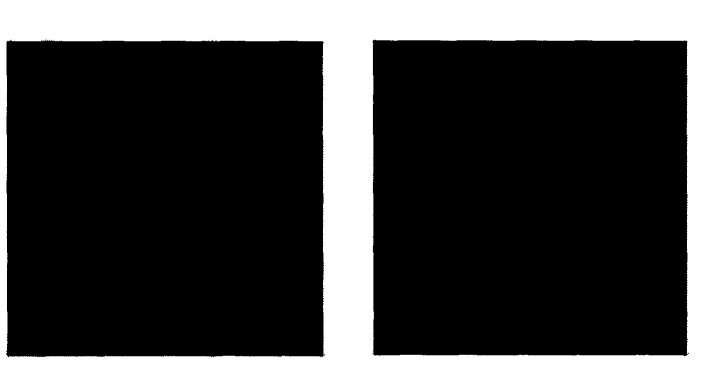
Figure 6-5: 2D slice-selective images of a cylindrical water phantom 3 mm in diameter and 18 mm in length. a. X-Y plane image of a 1 mm thick slice, with a resolution of 0.156 mm; b. Z-Y plane image of 2 mm-thick slice, with a resolution of 0.469 mm.

covers only a portion of the particle bed, without any free gas space beyond the two diffusers or at the top of the column. This configuration eliminates possible artifacts in NMR signals due to the inclusion of free gas in the sensitive region of the coil.

Fig. 6-5 shows 2D slice-selective images taken in both the X-Y and Z-Y planes, the sample being a doped-water phantom inserted into the column. These images demonstrate the good field homogeneity inside the column.

A similar fluidization apparatus has been designed for a horizontal-bore magnet with the same field strength. Both the inflow and outflow tubings were bent 90° to fit into the horizontal geometry. The RF coil was of solenoid type and capable of generating decent homogeneous field. The figure of this setup is in Appendix B-1. This first version of fluidization and NMR apparatus had two major problems. First, the filling factor of the solenoid coil was only ~ 6%, which resulted in fairly poor SNR. Secondly, the sensitive region of the coil covered not only the particle bed, but also the windbox below it, which generated a predominant narrow gas peak in the spectrum and led to complications to data analysis. We therefore designed the second

system discussed above, with subsequent improvements on the two issues.

6.2 Optimizing Fluidized Bed Performance

6.2.1 Verification of Fluidization Apparatus

In a static bed without gas flow, solid particles experience no motion and the packing pattern of these particles may be either random or ordered, depending on how these particles were placed in the container. The shear stress among the particles originating from particle weight keeps the system in a balance that is difficult to break without external forces. The large bulk modulus of the solid particles results in a distribution of the stress over distances much greater than the particle diameter, forming a force chain that contributes to several interesting signatures in particle behavior during fluidization. For example, the height of a bed of Geldart A particles exhibits hysteresis as gas flow is cycled up and down across the homogeneous fluidization regime [96]. The phenomenon occurs because the particles are tightly jammed together in a fixed bed, and in transition into fluidization, the force chain does not easily break without large gas flow velocity in excess of that necessary for producing drag forces to support the particle weight. Conversely, the inter-particle stress has been removed during defluidization, and hence the gas velocity required to suspend the bed at the same height is smaller.

Measurement of the hysteresis behavior in particle height was used to assess the quality of the fluidization apparatus. A poorly designed fluidized bed, e.g., slightly tilted (non-vertical) column, an ineffective windbox or a nonuniform diffuser, can cause significant cross-sectional heterogeneity in gas flow and result in unpredictable particle bed behavior. As a result, the hysteresis in particle height may disappear under these circumstances. We therefore checked the column performance for problems by observing hysteresis in the fluidization of glass beads.

Fig. 6-6 shows the measured particle bed height, observed visually, as a function of gas flow rate[2] at a constant gas pressure of 6.3 bar. Hysteresis was clearly observed

---

[2]Flow rate is measured in the unit "sccm", or standard cubic centimeter per minute, which is
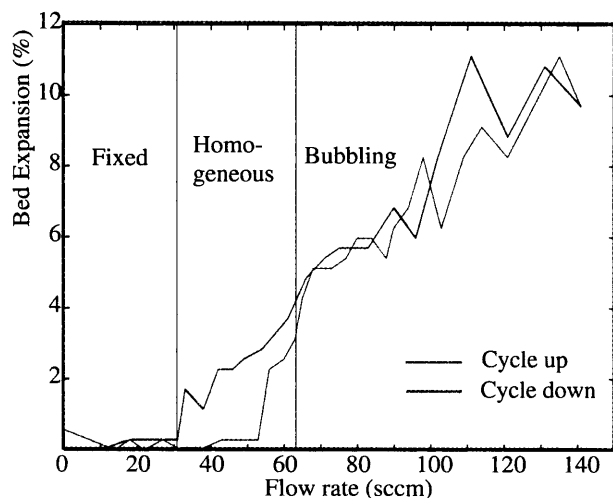
Figure 6-6: Hysteresis in bed expansion, measured as a function of gas flow rate. Dry N$_2$ gas was used in this measurement. The particles are the glass beads with good sphericity, and are classed as Geldart Group A particles. Homogeneous fluidization was therefore observable for these particles, with hysteresis apparent in this range of flow rates.

between the cycle-up and cycle-down tracks in the flow-rate range of 31 $\sim$ 64 sccm, where the bed operated in the homogeneous fluidization regime. The results are similar to those measured by Ojha *et al.* [96], and qualitatively verifies that our experimental apparatus is capable of providing a reliable fluidization process.

6.2.2 Xenon Gas Pressure

As xenon is moderately expensive ($\sim$ \$8 - 10 per liter), optimizing xenon consumption was a critical design consideration for these experiments . For some experiments, despite the enhancements gained by optical pumping, several hours of NMR signal averaging was required. During this time, the polarization system is ran in a continuous flow mode. It was found that the amount of xenon required could be significantly reduced by operating at the lowest possible gas pressure that still maintained the fluidization state.

Fluidization of particle beds is only weakly dependent on gas pressure. For par-

---

the volume flow rate at STP.
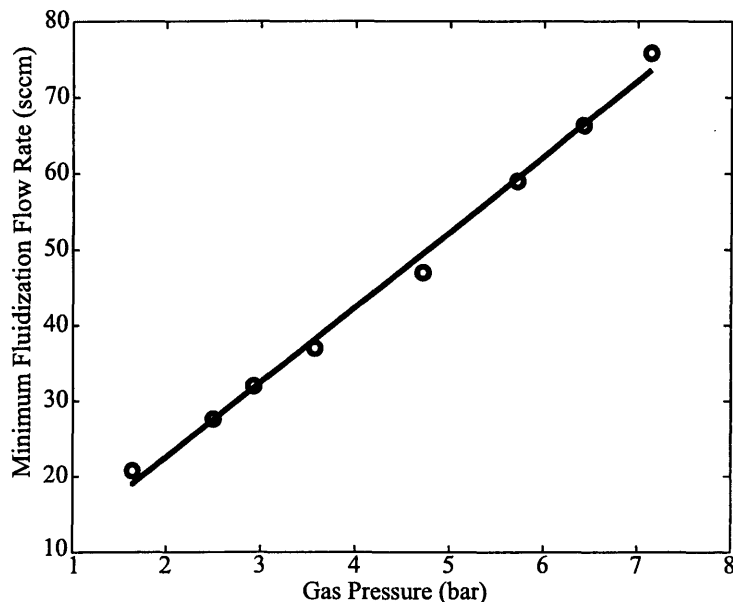
Figure 6-7: Dependence of minimum-fluidization flow rate U_{mf} on gas pressure. The uncertainty on the measured flow rates is 0.1 sccm. N_2 gas was used to fluidize the glass beads. Data points were measured flow rates. The solid line is a linear fit.

ticles with diameter less than 100 μm, the minimum gas velocity that results in fluidization, U_{mf}, is independent of gas density [97, 1]. To verify this on our fluidized bed setup, we measured gas flow rates corresponding to minimum fluidization at different gas pressures. The results are shown in Fig. 6-7. The flow rate measured is the mass flow rate, which is proportional to gas density, the tube cross-sectional area, and the flow velocity, U_{mf}. The very good linear fit implies that U_{mf} is independent of gas pressure. The most significant parameter that controls which fluidization regime the bed operates in is the gas flow velocity. Moreover, all the fluidization regimes are found to be equivalently approachable with low pressure settings, and only insignificant changes in fluidization parameters have been observed as pressure was increased [98]. It is therefore preferable to use reasonably low gas pressure so that the mass flow rate, or the rate of gas consumption, is reduced, while the bed operates in the same fluidization regime.

It is also important to account for the effect of xenon gas pressure on [129]Xe spin magnetization generated in the polarizer. The magnetization (and hence signal-to-

noise ratio) increases slowly with pressure[3], placing a lower limit on an applicable pressure value. We performed most NMR experiments with a gas pressure of 2.5 bar in the polarization cell, which provided adequate signal strength and relatively light xenon usage.

The pressure drop across the particle bed and the two gas diffusers was measured by two pressure gauges (26PC series by Honeywell, 100 psi maximum pressure) mounted at the inlet and outlet of the bed. ΔP increased linearly with the gas flow rate between 10 and 150 sccm. The pressure drop across a fluidized bed should be independent of flow rate [1], and thus the measured ΔP is hence primarily due to the two diffusers which provide a resistance to gas flow. The maximum pressure drop was $\Delta P = 0.04$ bar at flow rate of 150 sccm, only 5% of the average pressure in the bed. Therefore, pressure variations throughout the particle bed could be neglected at the 5% level.

6.3 Contrast Between Bubble and Emulsion Phases

In order to measure the exchange rate between the bubble phase and the emulsion phase using NMR technique, the two phases need to be clearly differentiated. The obvious difference between the bubble and emulsion phases is the concentration of solid particles: the emulsion has a large particle number density (the total volume of particles is $\sim 40\%$) while more than 99% of bubble volume is occupied by gas [1]. The gas in close contact with solid particles tends to experience faster longitudinal and transverse relaxation, and should therefore be distinguishable with NMR methods via T_1 or T_2 contrast. Our experiments rely on the enhanced spin polarization to acquire information on gas dynamics, and it is therefore implausible to use particles containing T_1 contrast agents that quickly diminish the spin polarization, resulting in significantly reduced signal-to-noise ratio. We hence searched for methods that utilize available T_2 contrast.

---

[3]Magnetization is the product of density and spin polarization. In the case of laser-polarized xenon, polarization decreases with xenon pressure due to the enhanced spin-rotation interaction between xenon and rubidium atoms [29].

Due to their high density, the magnetic susceptibility of solid particles is generally three orders of magnitude larger than that of xenon gas. When both materials are placed in a magnetic field of $\sim$ 1 T, magnetic susceptibility variations generate a considerable magnetic field gradient at the boundary between the solid and gas phases. The xenon gas spins in the emulsion phase thus tend to experience a much larger field inhomogeneity than those in bubbles. Moreover, gas bubbles are almost spherical in shape, and the resulting field inside the bubble will have a much higher homogeneity than that in the emulsion phase. The NMR spectral line from the bubble thus should be significantly narrower than that of the emulsion, providing a "contrast" between the bubble and emulsion so that a measurement of the exchange rate between them is possible.

Fig. 6-8 shows ^{129}Xe spectra measured in an aluminum oxide particle bed, with eleven different gas flow rates ranging from 15 to 125 sccm. The broad peak ($\sim$ 650 Hz FWHM) at lower frequency is from xenon gas in the emulsion phase, and is the result of the large field gradient in the interstitial spaces of the emulsion. There is a slight shift in frequency of this peak away from that of free xenon gas. A second broad peak with roughly the same width, but shifted 2.3 kHz, was identified as the adsorption phase peak.

We measured the spectra at different gas flow rates in order to identify the narrow peak ($\sim$ 75 Hz FWHM) located on the shoulder of the emulsion peak. The peak amplitude in Fig. 6-8 increased as the gas flow rate was raised from 15 to 125 sccm. It is known that more bubbles appear, and they increase in size, as the gas flow rate increases [99]. Based on the reasoning above that the magnetic field inside the bubbles will be more homogeneous, due to lower magnetic susceptibility variations, we identify the narrow peak as being from xenon in the bubbles. As the emulsion peak is over an order of magnitude broader than the bubble peak, we predict that it will be possible to differentiate the two phases unambiguously using NMR methods to highlight the T_2 contrast.

The spectrum was then acquired using the standard spin-echo pulse sequence [12] with an echo time $T_E = 8$ ms. The spectrum is shown in Fig. 6-9. Both the
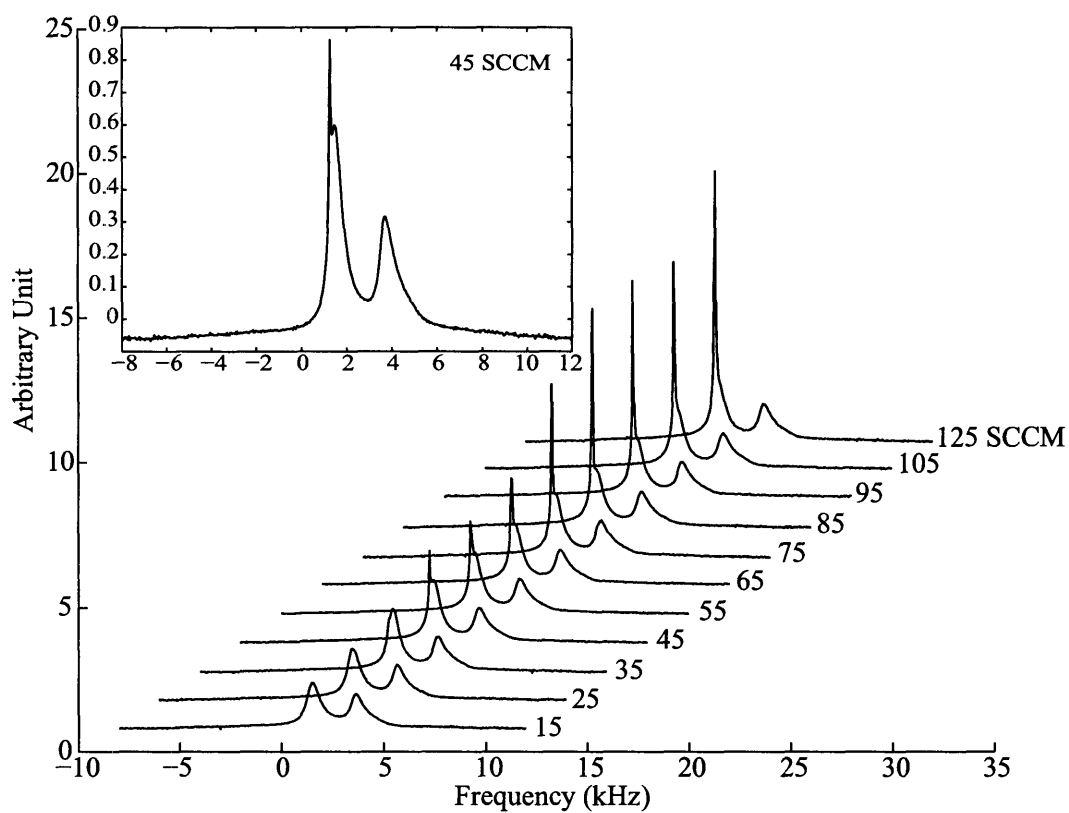
Figure 6-8: Spectra of ^{129}Xe in an Al$_2$O$_3$ particle bed, measured at 11 different gas flow rates (Fourier Transform of the acquired free-induction decays (FID) after a 90° hard pulse). The spectra were obtained by increasing the gas flow rate from 15 to 125 sccm at gas pressure of 2.0 bar. The narrow peak is believed to originate from the bubble phase.

123
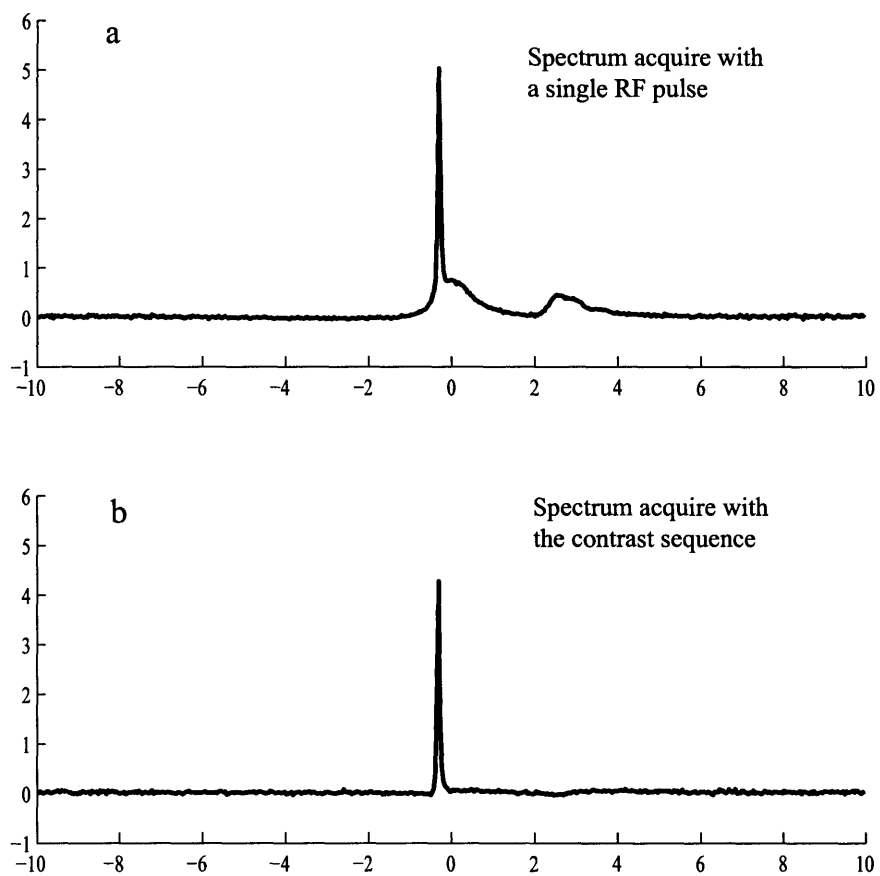
Figure 6-9: Spectra obtained from ^{129}Xe gas fluidizing a bed of Al_2O_3 particles. a) The complete spectrum, acquired from a single RF pulse. b) The spectrum acquired with a spin-echo sequence, with an echo time of 8 ms. The spin-echo spectrum clearly shows only the bubble peak, after removal of the emulsion and adsorption signals due to spin decoherence during the echo time.

Contrast
Generation   Exchange   Acqusition

$\frac{\pi}{2}$ π $\frac{\pi}{2}$ $\frac{\pi}{2}$

RF

τ_1 τ_2 τ_3
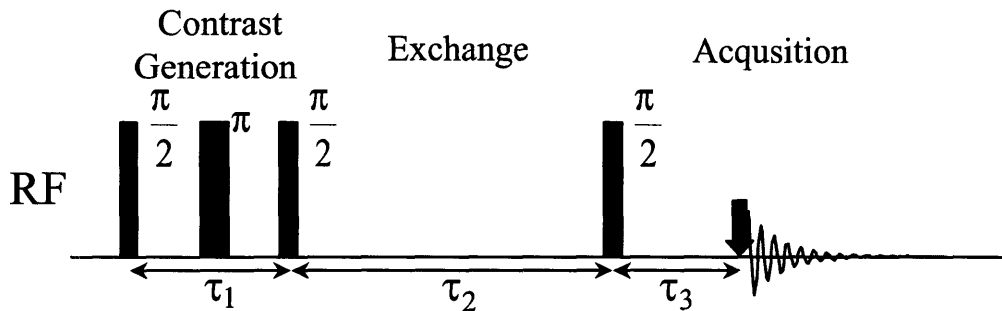
Figure 6-10: The NMR pulse sequence used in bubble-emulsion exchange rate measurements. A $\pi/2$ hard RF pulse non-selectively flips spins into the transverse plane. After application of a π pulse, a spin-echo is generated after time τ_1. τ_1 was chosen to be 8 ms, long enough for emulsion and adsorption magnetizations to decohere. The bubble magnetization is then stored along the z direction following the second $\pi/2$ pulse. Gas exchange between the bubble and emulsion phases occurs during the subsequent delay τ_2. The third $\pi/2$ RF pulse then returns the remaining magnetization back to the transverse plane, and the FID signal is acquired after a delay time τ_3 of 0.7 ms, which eliminates emulsion and adsorption magnetization that may have migrated from bubbles during τ_2. Therefore, only ^{129}Xe in the bubble phase contributes to the FID signal, which can be used to acquire useful exchange data.

emulsion and adsorption phase peaks disappear, due to gas diffusion in the presence of the strong background gradient in these two phases. It is clear that the spin-echo sequence worked effectively in suppressing the NMR signal from xenon in the emulsion and adsorption phases.

Fig. 6-10 shows a pulse sequence that employs T_2 contrast to remove the emulsion and adsorption peaks from the spectrum, leaving only the bubble peak, so that we can observe the time-dependence of the bubble magnetization and determine the bubble-emulsion exchange rate. The experiment is a three-stage process: contrast generation, exchange and acquisition.

Two factors may affect the bubble-emulsion exchange measurement. Bubbles are continuously generated from the bottom of the particle bed and pass through the bed with a velocity of $\sim$ 10 cm/s, corresponding to a time of 0.24 s for bubbles to rise from the bottom to the top of the RF coil. During the exchange time τ_2, more bubbles may enter the coil region from below with freshly polarized ^{129}Xe, and some

bubbles already in the RF coil region may exit the region at the top. The gas that is entering and exiting gas have approximately equal volume but may have differing spin polarization, resulting in a net accumulation of bubble magnetization during τ_2. This accumulation corresponds to the flow terms in Eqns. (5.14). To avoid this problem, we phase-cycled the first $90°$ pulse and the receiver phase together, which alternatively changed the polarity of the signal from the newly entering bubbles, and added together the signals from all the scans. This resulted in the effective cancellation of NMR signals from the newly arriving bubbles. (See Appendix D for details). A short pre-acquisition delay (75 ms) was used before starting the sequence each time and 64 dummy scans were applied, so that the length of the particle bed region containing polarized gas was approximately the product of the bubble velocity and the pre-acquisition delay, or 7.5 mm. The maximum length of exchange time, τ_2, was ~ 100 ms, during which the polarized gas region moved 10 mm upward. Therefore, the maximum length of the polarized gas region during the pulse sequence is 17.5 mm, which is less than the RF coil length (25 mm). Thus, the bubbles containing polarized gas will stay inside the coil during the measurement. The implementation of the experiment in this manner removes the flow terms in the differential equations depicting magnetization dynamics (Eqn. (5.14)), significantly simplifing their solution and making the comparison to experimental results much easier.

6.4 Measurement of the Bubble-Emulsion Exchange Rate

6.4.1 Prediction of Bubble-Emulsion Exchange Rate

The estimation of the exchange rate between the bubble and emulsion phases requires knowledge of the bubble sizes, as shown in Eqn. (5.8). Since the controllable experimental parameter is the gas flow rate, we need to understand how the average bubble size depends on gas flow rate. The size of a bubble size is directly related to its velocity, as given by Eqn. (5.7), and we therefore used a two-phase flow model to
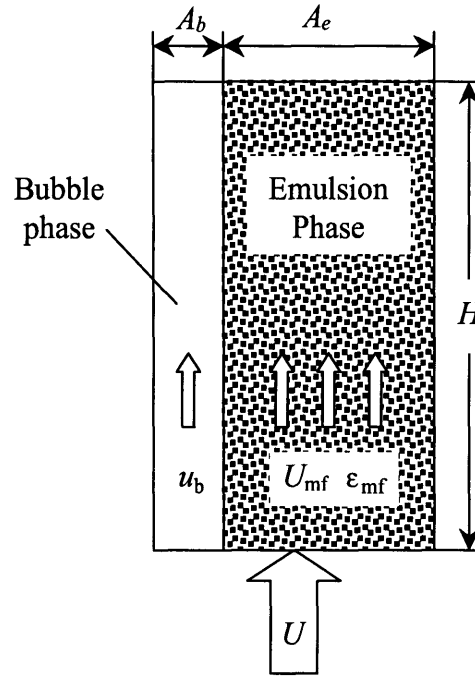
Figure 6-11: Two-phase flow model for gas flow in the bubble and emulsion phases. A_b and A_e are cross-sectional area of bubble phase and the emulsion phase, respectively. H is the height of the particle bed. U is the total empty-tube gas flow velocity. ϵ_{mf} is the void fraction in the emulsion phase.

determine the relation between bubble velocity and gas flow rate.

The flow velocity in the bubble phase is u_b. The emulsion phase is assumed to stay in the homogeneous fluidization state since changes in void fraction and interstitial gas velocity in the emulsion are negligible as gas flow rate increases [65]. The void fraction in the emulsion is therefore approximated by ϵ_{mf}, and the gas velocity by U_{mf}/ϵ_{mf}. The total gas flow velocity U is related to the flow rate q by the equation

$$U = \frac{T}{T_0} \frac{q}{AP}, \tag{6.1}$$

where T is the gas temperature, which was $24°$ C for our experiment; $T_0 = 273.15$ K; A is particle bed cross-sectional area which equals 0.302 cm^2; and P is the gas pressure measured to be 2.0 bar. We therefore have $U_{mf} = 0.541$ cm/s, calculated from Eqn. (6.1), given our experimental observation of $q_{mf} = 18$ sccm.

Fig. 6-11 schematically depicts a model where inflowing gas is distributed into the two phases. Given that the total volume flow rate should be equal to the sum of the flow rates in the two phases, we have

$$UA = u_b A_b + U_{mf} A_e,$$ (6.2)

where A is cross-sectional area of the whole bed; A_b and A_e are cross-sectional areas taken up by the bubble phase and emulsion phase respectively. Obviously $A = A_b + A_e$. The fraction of bed taken up by bubbles is

$$\delta = \frac{V_b}{V} = \frac{A_b H}{A H} = \frac{A_b}{A},$$ (6.3)

where V_b and V are bubble volume and total bed volume respectively; H is the bed height. We hence relate the bubble volume fraction, δ, to the bubble velocity, u_b, as

$$\delta = \frac{U - U_{mf}}{u_b - U_{mf}},$$ (6.4)

From Eqn. (5.7) and (6.4), we can determine the bubble diameter by measuring the bubble-induced bed expansion as a function of the gas flow rate, and then use Eqn. (5.8) to determine the dependence of the bubble-emulsion exchange rate on the gas flow rate. The expansion of the fluidized bed, E, is related to bubble fraction, δ, by

$$E = \frac{\delta}{1 - \delta}.$$ (6.5)

The emulsion phase also expands as flow rate increases, exhibiting increased inter-particle distance, but this expansion is minimal compared to that due to bubble formation, and can be neglected, especially for Geldart Group B particles [65]. This approximation is consistent with the previous assumption that the emulsion phase may be considered to always be in a state equivalent to minimum fluidization [1]. Eqn. (6.4) has been verified by Orcutt, Davidson and Pigford, who used it to estimate the bubble diameter [100]. It has also been used by Menon and Durian [62] in their

128
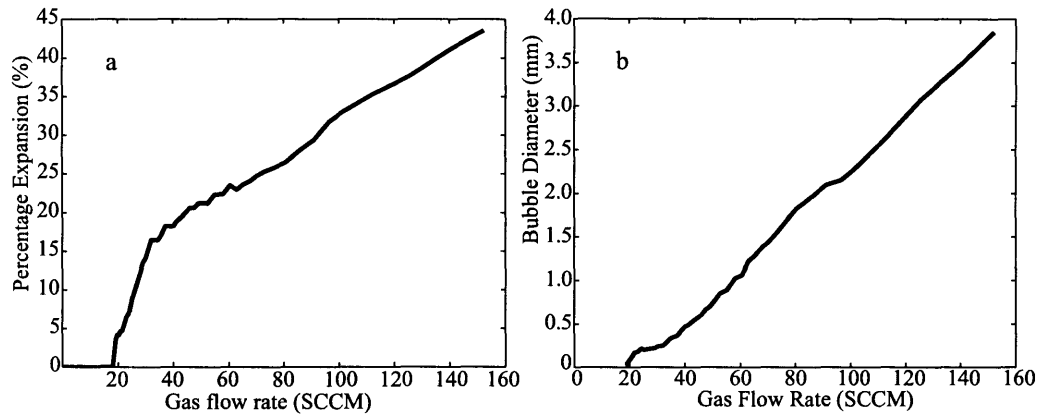
Figure 6-12: Measured particle bed expansion (a) and estimated bubble diameter (b) as functions of gas flow rates. The size of the bubbles increases monotonically with the flow rate. At 160 sccm, the bubble diameter is greater than 60% of the column inner diameter, indicating that the fluidization is approaching the slugging regime. This was confirmed by visual inspection of the bed at that flow rate.

experimental studies, where they used 96 μm glass beads, close to our particle size[4]. The approximation that the emulsion volume expansion negligible will be validated in section 6.4.2.

By visually studying the particle bed surface, we measured the percentage expansion of the aluminum oxide bed as the gas flow rate was increased from 0 to 150 sccm, at which point the bed started to demonstrate slugging behavior. Fig. 6-12 shows the result of this measurement. The total volume of the particle bed occupied by bubbles varies even at a constant gas flow rate, since both the number of bubbles and average bubble size fluctuate. We therefore measured the average value of the expansion by observing the top of the particle bed for 30 seconds, a time much longer than the time scale for the fluctuation. The average bubble diameter was then calculated by using the equations (6.4), (6.5), (5.7) and $U = q/AP$. Similarly U_{mf} is related to the flow rate corresponding to the onset of fluidization.

Using Eqn. (5.8) and the calculated bubble diameters, we predicted the bubble-emulsion exchange rate k_{be}, as shown in Fig. 6-13. As the flow rate increases, the

---

[4]Menon and Durian used approximation $E \approx \delta$, based on the experimental condition that bubble volume was much smaller than that of the whole bed, i.e. $\delta \ll 1$. Moreover, u_b was considered much larger than U_{mf} and therefore $u_b - U_{mf} \approx u_b$.
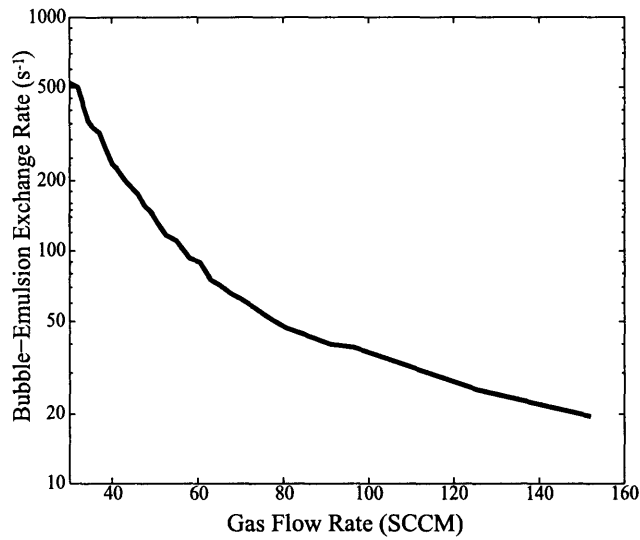
Figure 6-13: Predicted bubble-emulsion exchange rate. Since 35 sccm was the point where we started to observe a bubble peak in the ^{129}Xe NMR spectra, it was the lowest flow rate where bubble-emulsion exchange could be measured. Thus the prediction curve does not extend to flow rates below 30 sccm. The exchange rate is plotted on a logarithmic scale.

average size of the bubbles gets larger, since more inflowing gas enters the bubble phase and the coalescence of adjacent bubbles is enhanced. The exchange rate for larger bubbles is expected to be smaller, since it takes longer to replenish gas in a larger bubble. The exchange rate was found to be strongly dependent on the flow rate, for the range 30 and 75 sccm, but weakly dependent when the flow rate is faster than 75 sccm.

6.4.2 Determining Ratios of Void Fractions in Different Phases: ψ_b/ψ_a and ψ_e/ψ_a

Eqn. (5.26) relates the bubble-emulsion exchange rate to the decay rate of bubble magnetization measured with the pulse sequence shown in Fig. 6-10, giving

$$k = k_{be}(1 + \frac{\psi_b}{\psi_e + \psi_a}), \tag{6.6}$$

130
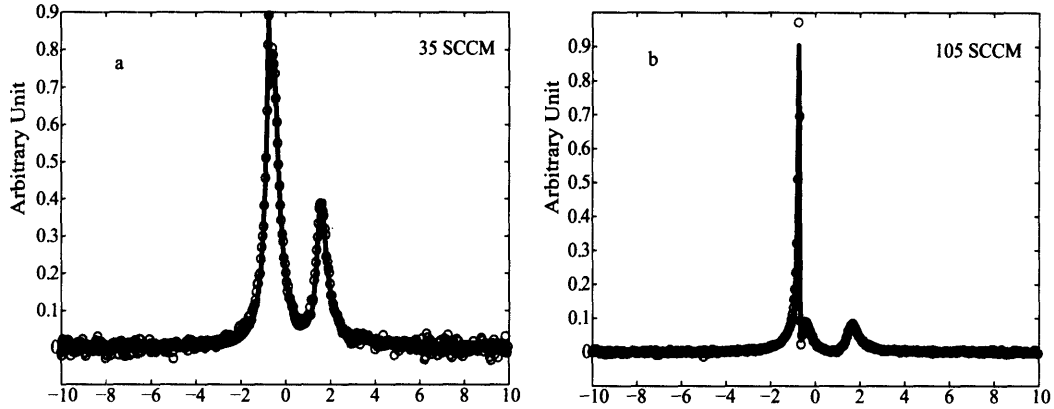
Figure 6-14: Peak deconvolution in ^{129}Xe spectra obtained from xenon gas fluidizing Al$_2$O$_3$ particles. Deconvolution was achieved by fitting to three independent Lorentzians. a) spectrum measured at flow rate of 35 sccm, with a small bubble volume. b) spectrum at flow rate of 105 sccm, with a large fraction of the gas in the bubble phase. The circles in the two plots label the measured spectra, and the lines are fitting results.

where k is the exponential decay rate of the bubble magnetization. We determined the coefficients ψ_e and ψ_a, respectively, the volume percentage occupied by emulsion and adsorption phases, before calculating the value of k_{be} from k.

ψ_e/ψ_a is equivalent to the ratio of the emulsion and adsorption magnetization, which are given by integrals of the two peaks in ^{129}Xe spectra. However, direct integration of the emulsion and adsorption peaks was difficult due to the overlap of the two broad peaks. Moreover, the bubble peak was on the shoulder of the emulsion peak, resulting in fairly complicated spectra. To address this problem, we fitted the spectra to the sum of three Lorentzian curves to separate the contributions from the different components. Fig. 6-14 shows the results of the curve fitting on the spectra measured at 35 and 105 sccm respectively.

We integrated the emulsion and adsorption peaks in each spectrum, and calculated the ratio between them to yield ψ_e/ψ_a, as shown in Fig. 6-15. When these spectra were acquired, a dead time was used between the end of the RF excitation pulse and the start of data acquisition, to allow for coil ring down. The emulsion and adsorption magnetization were both attenuated during the dead time, the amount of attenuation being related to their transverse decoherence times T_2^*. Since the observed

131
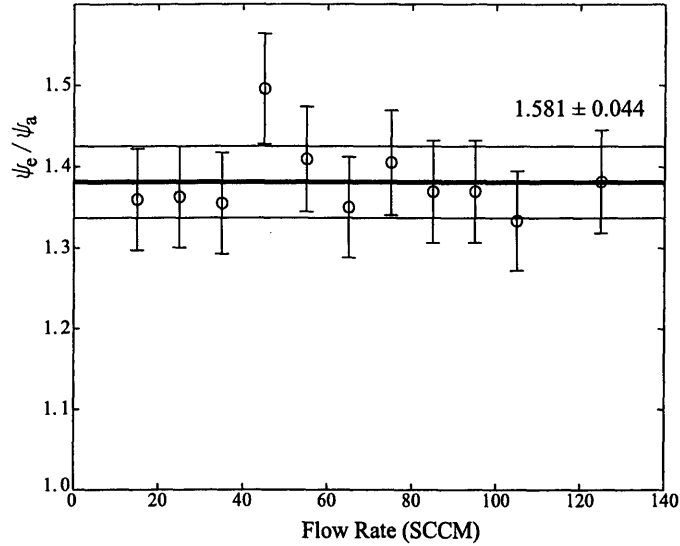
Figure 6-15: Plot of the ratio of emulsion phase to adsorption phase volume, ψ_e/ψ_a as a function of gas flow rate. ψ_e/ψ_a was seen to be independent of flow rate, and determined to be 1.581 ± 0.044. The error bars were estimated from the noise level in the spectra.

T_2^*'s associated with the two peaks were the same based on linewidth measurements, their attenuations were of the same amount and did not affect the calculation of ψ_e/ψ_a.

No dependence of ψ_e/ψ_a on the flow rate has been observed, even though the measured variations around the average value, 1.581 ± 0.044, were observed. The volume of the adsorption phase is directly related to the micropore volume of the particles, which is flow-independent given a constant temperature and gas pressure. ψ_a is hence proportional to the volume of the solid phase and the porosity of the particles. The ratio ψ_e/ψ_a therefore reflects the ratio of interstitial volume to solid volume, and is a measure of the expansion of the emulsion phase as a function of flow rate. This result confirms that expansion in the emulsion phase is negligible for the Geldart Group B particles used in our measurement.

We therefore conclude that the ratio of emulsion gas volume to adsorption gas volume is independent of the gas flow rate and simply use the average value

132
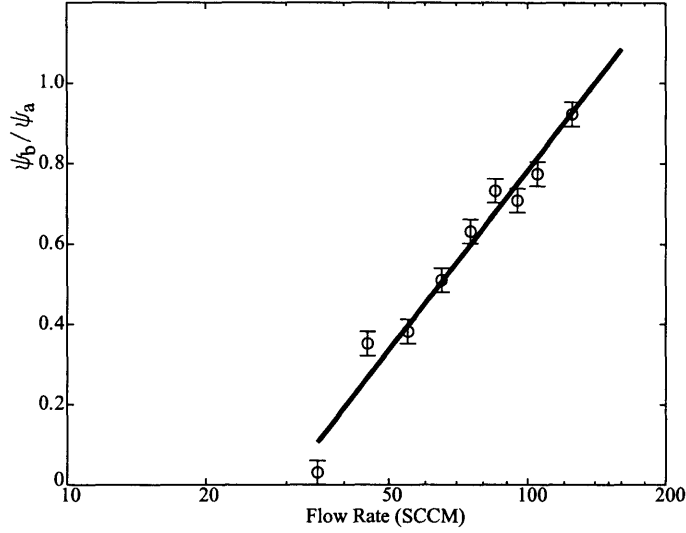
Figure 6-16: Plot of the dependence of ψ_b/ψ_a on gas flow rate, which is plotted here on a logarithmic scale. The ratio steadily increases with flow rate, consistent with the knowledge that bubble volume increases steadily with gas flow rate. The error bars were estimated from the noise level in the spectra.

$$\frac{\psi_e}{\psi_a} = 1.581 \pm 0.044 \tag{6.7}$$

for the rest of the thesis.

Calculation of the exchange rates also requires knowing the ratio ψ_b/ψ_a, which can also be determined available from the spectra of gas-phase ^{129}Xe fluidizing the Al_2O_3 particles. Using the same peak deconvolution from Fig. 6-14, we integrated the bubble and adsorption peaks and calculated the ratio R_{ba}. Accounting for the dead time, $\tau = 0.5$ ms, between the end of the $\pi/2$ pulse and the beginning of data acquisition, and the transverse relaxation times in the two phases, $T_{2b}^* = 4.4$ ms and $T_{2a}^* = 0.50$ ms measured with the CPMG sequence, we calculated ψ_b/ψ_a

$$\frac{\psi_b}{\psi_a} = \frac{e^{-\frac{\tau}{T_{2a}^*}}}{e^{-\frac{\tau}{T_{2b}^*}}} R_{ba}. \tag{6.8}$$

R_{ba} was determined from nine different spectra acquired at flow rates throughout the bubbling fluidization regime, and the resultant ψ_b/ψ_a values are given in Fig. 6-

133

16. The flow rate is plotted on a logarithmic scale, and a linear fit of the data points gives the following relationship between the two parameters:

$$\frac{\psi_b}{\psi_a} = -2.1862 + 0.6446 \log q, \qquad (6.9)$$

which is a useful empirical relation for finding the value of ψ_b/ψ_a at any flow rate. The correlation coefficient R^2 (see Appendix E for definition) associated with the linear fitting was found to be 0.962, representing a good linear relationship. Fig. 6-16 indicates the volume fraction occupied by bubbles in the bed increased as flow rate went up.

Note that the measurement of bubble volume by the spectroscopy method was not accurate when the bed was just above the minimum fluidization condition, i.e., at flow rates between 18 and 35 sccm. The bubble-emulsion contrast mechanism is not effective when the bubble size is similar to the particle size. From Fig. 6-12, we can see that the bubble diameter at such flow rates is < 0.2 mm, or less than two times the particle diameter. In this case, the contrast in field homogeneity is weak and the bubble peak may not be observable. This explains the extremely low bubble peak amplitude at flow rate below 35 sccm, even though a significant amount of bubbles were seen by visual inspection.

The ψ_e/ψ_a and ψ_b/ψ_a values at different flow rates were then used in relating the experimental data to the actual exchange rates, with interpolation or extrapolation applied if necessary.

6.4.3 NMR Results

We measured the xenon exchange rate between the emulsion and bubble phases using the pulse sequence shown in Fig. 6-10, with a series of values for the exchange time, τ_2, ranging from 1 to 50 ms. Nine different gas flow rates between 35 and 150 sccm were used. Fourier-Transformation of the FID signals yield post-exchange ^{129}Xe spectra containing only the bubble peak, which was integrated to determine the bubble magnetization. The time-dependence of the bubble magnetization, together
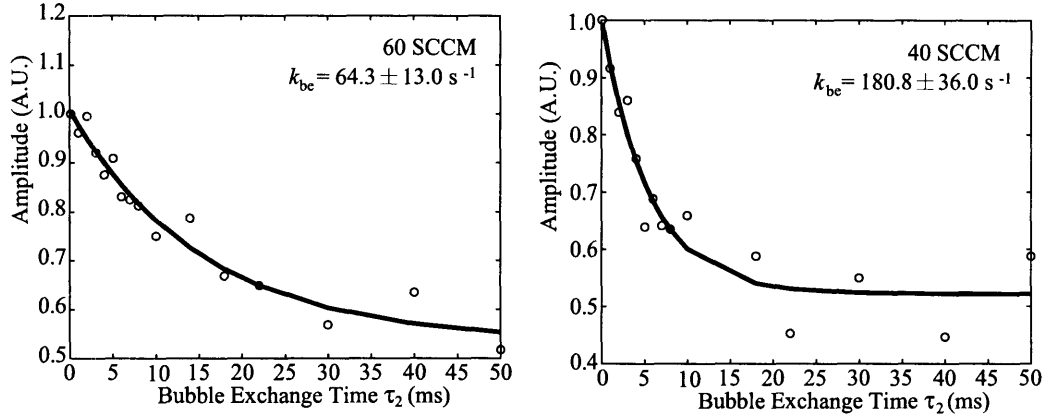
Figure 6-17: Decay of bubble magnetization at 15 different exchange times, τ_2, and two different flow rates: 60 and 40 sccm. The exponential fits yield decay rates that were related to bubble-emulsion exchange. 256 signal-averaging scans were used for each acquisition, and the resulting signals coherently added to reduce variations in the bubble amplitude. The delay times used in the sequence were: contrast delay time, $\tau_1 = 8$ ms, exchange time, τ_2, varied between 1 and 50 ms, pre-acquisition delay $\tau_3 = 0.7$ ms.

with a fitted exponential curve, is plotted in Fig. 6-17 for two selected flow rates. At both flow rates, the data fit to a single-exponential, indicating no evidence of recirculation of gas between the bubbles and their surrounding cloud. The variation in the results measured at 40 sccm was due to statistical errors resulting from small number of detectable bubbles. The number of bubbles in the coil-sensitive region of the particle bed was estimated to be about 30. The generation and coalescence of bubbles are uncontrollable random processes, resulting in variations in the number of bubbles in the particle bed at any instant of measurement. When the bed is initially fluidized, fewer bubbles exist and more significant variations are expected. This statistical error is the major contributor to the uncertainties in the exchange rate measurements.

The exponential decay rate of bubble magnetization is related to the exchange rate according to Eqn. (6.6), and can be equated to:

$$k = k_{be}(1 + \frac{\psi_b}{\psi_e + \psi_a}) = k_{be}(1 + \frac{\psi_b/\psi_a}{1 + \psi_e/\psi_a}). \qquad (6.10)$$

135
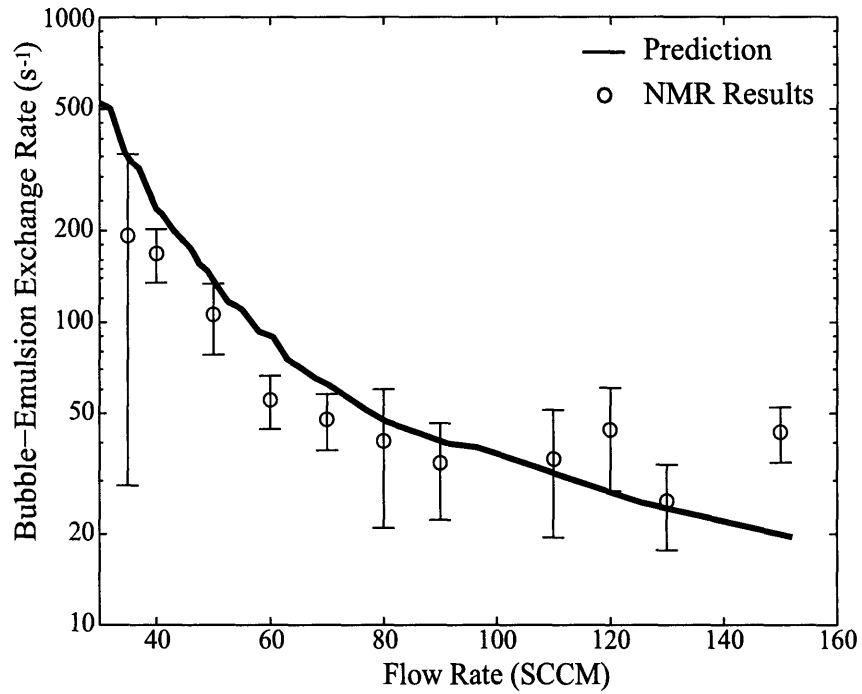
Figure 6-18: Measurements of the bubble-emulsion exchange rate. The predicted curve from Fig. 6-13 is included for comparison. 256 signal averaging scans were summed in each measurement to reduce statistical errors. The exchange rate is plotted on a logarithmic scale.

By using the values of ψ_b/ψ_a and ψ_e/ψ_a determined in the last section, we found the following correlation between k, k_{be} and flow rate q

$$k = (0.1530 + 0.2497 \log q)k_{be},$$ (6.11)

which allows the bubble-emulsion exchange rate to be calculated as a function of flow rate. A plot of this data is shown in Fig. 6-18.

The measured exchange rates agree well with the prediction curve, which was derived in section 6.4.1 and was based on limited information and several assumptions. The large uncertainty in the data at 35 sccm is due to statistical errors resulting from the small number of bubbles found in the bed at this flow rate. The measured rates are smaller than the prediction for flow rates below 60 sccm, and the discrepancy may be explained by the presence of the cloud phase. In the development of the model

136

used to derive the predicted curve, we included the cloud phase in the emulsion, assuming the exchange between the two is much faster than that between bubbles and their clouds. Recirculation of polarized gas back into the bubbles, which would effectively reduce the exchange between the cloud and the emulsion, resulting in the lowered overall exchange rate. Therefore, the neglected cloud phase is one possible reason for the discrepancy.

Aside from the minor discrepancy, the prediction based on Davidson's model agrees well with the experimental data. The measurement verifies that this model may be safely used in predicting bubble-emulsion exchange rates in the design of fluidized beds.

6.5 Measurement of the Emulsion-Adsorption Exchange Rate

The bubble-emulsion exchange was measured assuming the exchange between the emulsion and adsorption phases is much faster and the two phases were indistinguishable. Conversely, emulsion-adsorption exchange can also be measured if we consider k_{be} to be very slow, and therefore negligible. The exchange is limited by gas diffusion in the interstitial spaces of the emulsion, and in Section 5.2.4, the time scale for this diffusion was estimated to be ~ 1 ms.

We designed a pulse sequence, that is similar to teh standard saturation-recovery experiment, to undertake this measurement of emulsion-adsorption exchange. The sequence is shown in Fig 6-19.

The selective saturation pulses only cover the frequency range of the adsorption peak, but leaves the magnetization in the emulsion phase unperturbed. The selective pulses were not expected to completely spoil the adsorption magnetization since the length of the pulse itself is ~ 1 ms, which is on the same order as the expected emulsion-adsorption exchange time. A certain amount of adsorption magnetization remains after the selective pulses, but the balance between the two phases has been
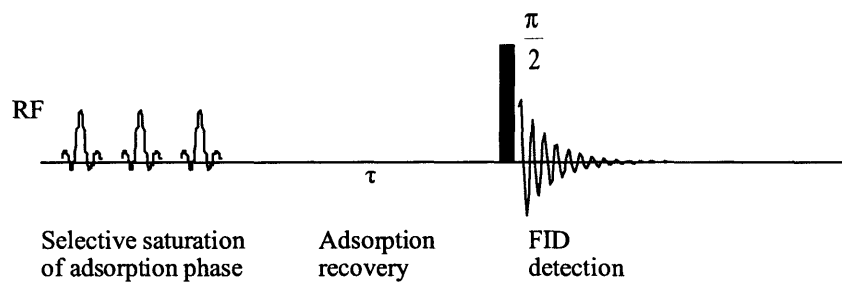
Figure 6-19: NMR pulse sequence used to measure the emulsion-adsorption exchange rate. Three $\pi/2$ selective pulses were used to rotate the adsorption magnetization into the transverse plane repeatedly, so that the magnetization balance between the two phases was disturbed. The separation between any two soft-pulses is 1.0 ms, of the same order as the transverse relaxation time of the adsorbed phase, T_2^a. A delay time, τ, was then used to allow exchange to occur between the adsorbed and emulsion phases. Spins exchanging in from the emulsion phase retain their high spin polarization. τ was varied in our experiments from 0.1 to 10 ms. Finally a non-selective $\pi/2$ RF pulse allowed sampling of magnetization components in all phases, after exchange.

disturbed. We were able to measure the exchange rate by observing the rate at which the adsorption magnetization was recovered from this perturbation.

We used a similar curve fitting and peak deconvolution technique mentioned in previous section to resolve overlapping peaks, and performed an integration over the adsorption peak to retrieve adsorption magnetization after different delays, τ. Fig. 6-20 shows one of the spectra, measured at 60 sccm. The spectral line was fitted to three Lorentzians, and then the bubble and emulsion peaks were subtracted. Next an exponential fitting was applied to find the adsorption peak decay rate k'. According to Eqn. (5.28), k' is related to the emulsion-adsorption exchange rate k_{be} by

$$k' = k_{ea}(1 + \frac{\psi_e}{\psi_a}), \qquad (6.12)$$

where $\frac{\psi_e}{\psi_a} = 1.581$. The resultant k_{ea} values measured as a function of gas flow rate are shown in Fig. 6-21. The value of k_{ea} scatters around an average value of 388 s^{-1}, and no obvious dependence on gas flow rate is observed. k_{ea} is related to the gas diffusion in the interstitial space only, as the Peclet number is much less than one for all flow rates used. Additionally, as we showed in Section 6.4.2, the expansion of the emulsion phase is negligible and as such the inter-particle distance in the emulsion is considered independent of flow rate. Therefore, the time for a gas molecule to traverse the interstitial space in the emulsion remains constant, and hence k' should be independent of flow rate. The experimental results are in agreement with this theoretical understanding.

The apparent decay rate $k_{be}(1 + \frac{\psi_b}{\psi_a + \psi_e})$ for bubble-emulsion exchange is an order of magnitude slower than the rate $k_{ea}(1 + \frac{\psi_e}{\psi_a})$ for emulsion-adsorption exchange. This verifies the assumption of Inequality (5.22), made in the last chapter, for decoupling the two exchange processes and considering them isolation.

6.6 Error Analysis

We estimated uncertainties in the NMR measurements of the exchange rates by error propagation of the uncertainties in the NMR signal amplitudes and their integrations,

a

Amplitude (A.U.)

0.8
0.6
0.4
0.2
0

Bubble
Emulsion
Adsorption

−10 −8 −6 −4 −2 0 2 4 6 8 10

Frequency (Hz)

b

Amplitude (A.U.)

3
2
1
0

5 ms

1.1 ms

0.5 ms

$\tau = 0.1$ ms

−5 0 5 10 15 20 25 30 35

Frequency (Hz)
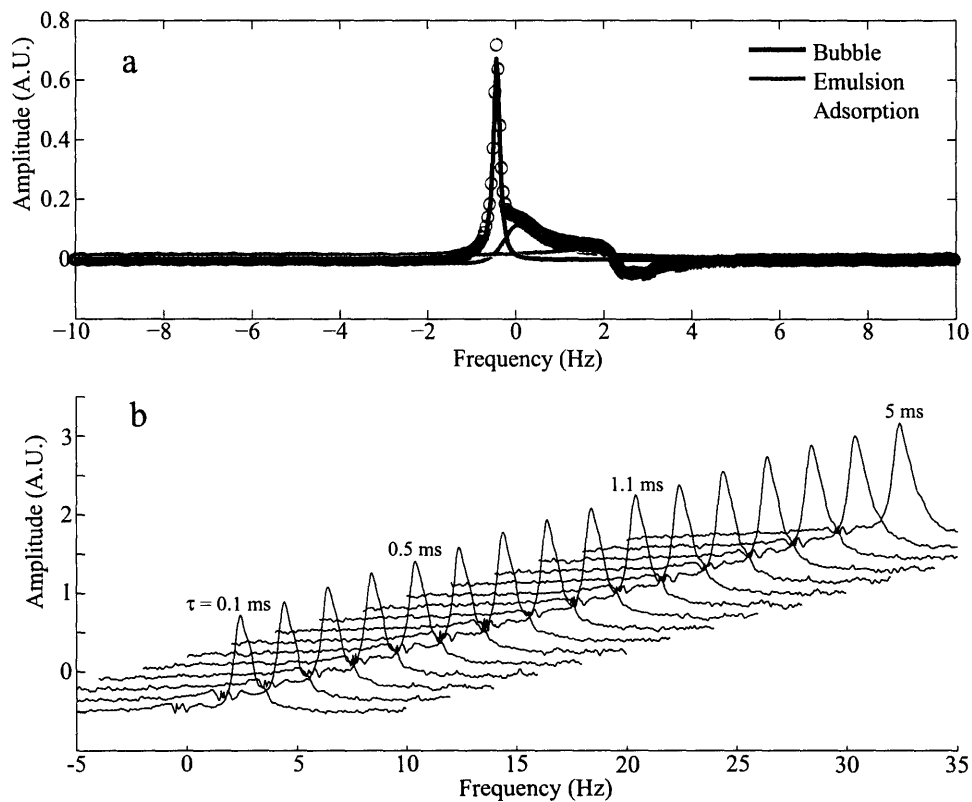
Figure 6-20: (a) A single ^{129}Xe spectrum measured at a gas flow rate of 60 sccm, along with deconvoluted spectra for each component derived from fitting the main spectra with three Lorentzians. (b) The derived spectra for the adsorption peak only, after subtraction of the fitted bubble and emulsion components measured at 16 different exchange times, τ. The ripples around zero frequency are the result of imperfect subtraction of the much larger bubble peak. The amplitude of the adsorption peak increases slowly with the exchange time, τ, which was used to find the exchange time.

140
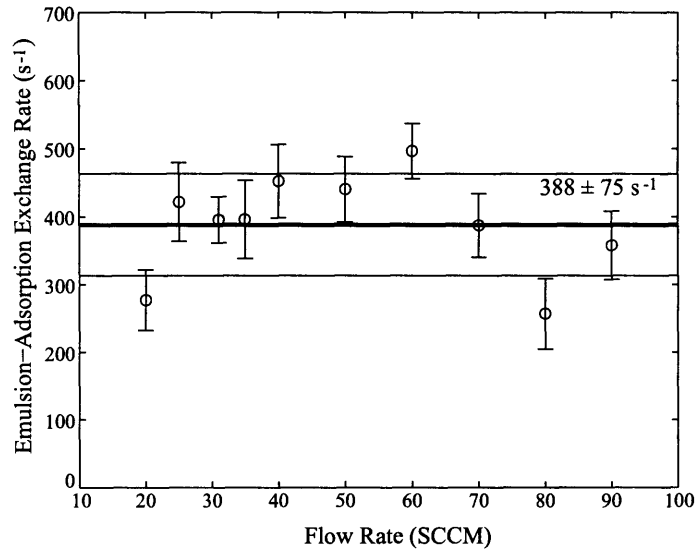
Figure 6-21: The emulsion-adsorption exchange rate measured at nine different gas flow rates. Each data point was result of exponential fitting of the adsorption magnetization recovery to delay time, τ, as shown in Fig. 6-20 for 60 sccm. k_{ea} was then calculated with Eqn. (6.12). The exchange rate is considered independent of flow rate.

I. To calculate the standard deviation in the signal amplitude, ΔS, we measured the standard deviation of the intensity of n consecutive data points representing pure noise in the spectrum where no ^{129}Xe signal was present. ΔS is equal to this standard deviation. Then, if the number of data points used to calculate the integration, I, of the spectrum is N, the uncertainty in I is

$$\Delta I = \sqrt{N}\Delta S,$$

since the noise-induced fluctuations are not statistically correlated.

We determined the decay rate of the bubble magnetization, k, given in Eqn. (6.6), by first integrating the bubble peak in the spectrum, and then fitting the integral, I, to an exponential. I is related to the delay time, t, by the exponential function $I = Ae^{-kt} + B$, and k is determined from least-square fitting of the data to the following linear relation,

$$\ln\frac{I - B}{A} = -kt,$$

and the uncertainty of the fitted k value is given by (see Appendix E or [53])

$$\Delta k = T_2^2 \sqrt{\frac{1}{\Delta} \sum_{i=1}^{n} \frac{1}{\sigma_i^2}},$$

where σ_i and Δ are

$$\sigma_i = \frac{\Delta I_i}{I_i - B},$$

$$\Delta = \sum_{i=1}^{n} \frac{1}{\sigma_i^2} \sum_{i=1}^{n} \frac{t_i^2}{\sigma_i^2} - \left(\sum_{i=1}^{n} \frac{t_i}{\sigma_i^2}\right)^2,$$

in which I_i is the integral of the spectrum measured after the delay time, t_i. The uncertainty in the bubble-emulsion exchange rate, k_{be}, is therefore given by

$$\Delta k_{be} = k_{be} \sqrt{\left(\frac{\Delta k}{k}\right)^2 + \left[\frac{\Delta\left(\frac{\psi_e}{\psi_a}\right)}{1 + \frac{\psi_e}{\psi_a}}\right]^2 + \left[\frac{\Delta\left(\frac{\psi_b}{\psi_a}\right)}{\left(\frac{\psi_b}{\psi_a}\right)}\right]^2}, \qquad (6.13)$$

where $\Delta\left(\frac{\psi_e}{\psi_a}\right)$ is given in Eqn. (6.7) and $\Delta\left(\frac{\psi_b}{\psi_a}\right)$ is determined by calculating the standard deviation of the data points shown in Fig. 6-16, subtracted from the fitting result given in Eqn. (6.9).

The uncertainty in the emulsion-adsorption exchange rate was calculated using the same method.

6.7   Gas Velocity Measurement

We have also measured the gas flow velocity in a fluidized bed with the pulsed-gradient stimulated echo (PGSTE) sequence. Seven different gas flow rates were used to observe the effect of flow rate changes on gas velocity distribution. Glass beads of 50 μm in diameter were used in this measurement. They provide a higher NMR
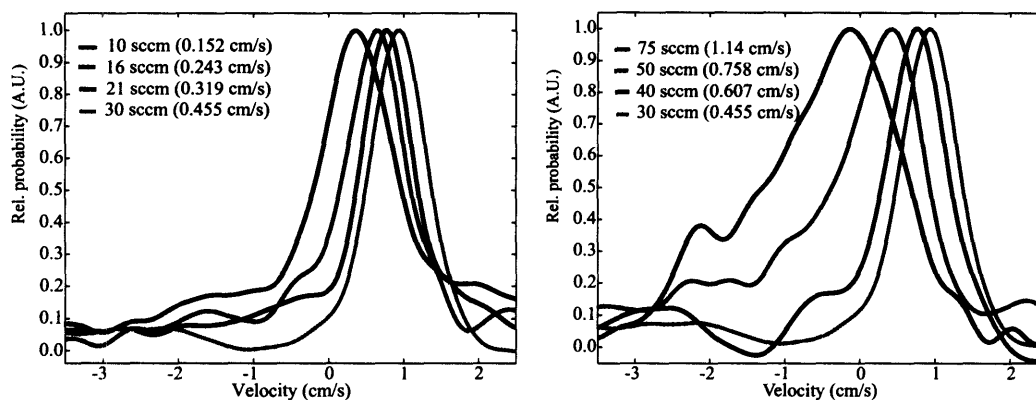
Figure 6-22: Xenon gas velocity distributions measured in two fluidization regimes. 50 μm glass beads were fluidized by laser-polarized xenon. Velocity spectra were measured by the pulsed field gradient stimulated echo technique, in which the gradient pulse duration, d = 1 ms, the flow encode time D = 10 - 1000 ms and the maximum gradient pulse strength was 20 G/cm. a). Four different gas flow rates: 10, 16, 21 and 30 sccm were used, all of which ensured the particle bed was in the homogeneous fluidization regime. b). Similar measurements made at three higher gas flow rates: 40, 50 and 75, corresponding to the bubbling fluidization regime. Also included is the data for 30 sccm, the transition point between homogeneous and bubbling fluidization. The superficial gas velocities corresponding to the flow rates are given in parentheses.

signal since the Xe spectral peak is an order of magnitude narrower with the alumina particles. The results of the measurement are shown in Fig. 6-22. When the gas flow rate was below 30 sccm, the particle bed was in the homogeneous fluidization regime, in which our previous measurements show that the movement of particles is minimal and the gas percolates through the interstitial spaces in the laminar flow regime. This is verified by the results shown in Fig. 6-22 a), where the average velocity increases with gas flow rate but the broadness of the distribution, a measure of random dispersion, is independent of flow rate.

Fig. 6-22 b) shows the velocity distributions at flow rates above 30 sccm, where the particle bed is in the bubbling fluidization regime. As as result of bubble formation and movement, particle motion now occurs. This motion changes the flow paths continuously, and therefore increases gas dispersivity. The velocity distribution corresponding to 30 sccm is also included for comparison. The width of the peaks increased with gas flow rate, indicating more random gas flow patterns related to

bubble-agitated particle motion. Surprisingly, the average gas velocity was seen to decreased at higher gas flow rates in this regime. We believe the reason for this is that the bubble velocity was larger than the maximum velocity detectable with this method. A larger portion of gas entered the bed in form of bubbles at a higher gas flow rate, and left the bed without being detected, resulting in a decreased observed average gas velocity.

Chapter 7

Discussion of Fluidized-Bed Experiments

7.1 Verification of Assumptions

The experimental study presented in Chapter 6 attempted to characterize the complex gas-phase dynamics of a gas-fluidized bed. The underlying theoretical model and the execution of the experiments were based on several assumptions that helped reduce the complexity of the problem but still captured the essence of the complex flow. In this chapter we review the main assumptions made in the earlier two chapters and assess their justification.

7.1.1 Merging Cloud and Emulsion Phases

The clouds exist around every single bubble, between the bubble and emulsion phases. In development of the model described in Section 5.2.5, we assumed that the gas exchange rate between clouds and the emulsion phase is much faster than the bubble-cloud exchange so that the recirculation of gas immediately back into bubbles is negligible, owing to the substantive gas adsorption and fast exchange between interstitial gas and adsorbed atoms. We hence lumped clouds into the emulsion phase, with the additional justification that they are both particle-dense phases.

145
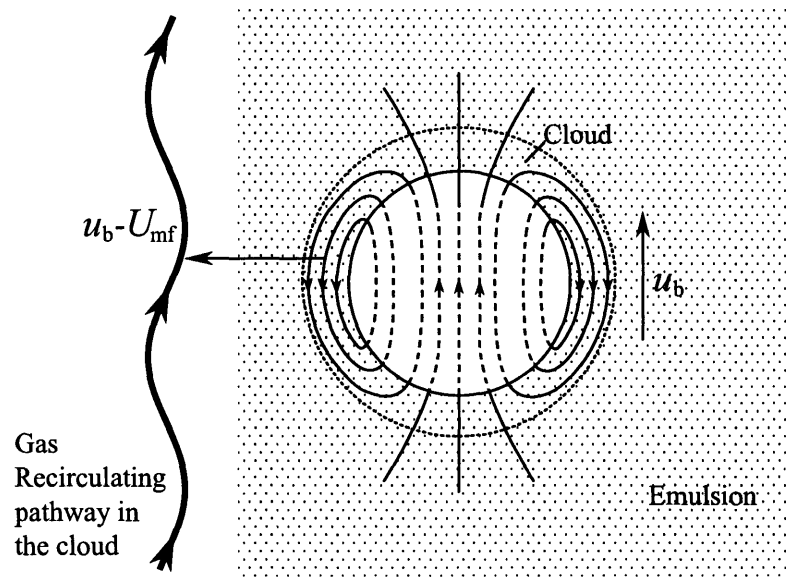
Figure 7-1: Recirculation of gas through a bubble. The circulating gas penetrates the dense cloud around the bubble. The particles surrounding the bubble are assumed to have negligible velocity compared to the bubble rising velocity u_b, according to Davidson's bubble model. The thick curve on the left shows the flow path of the recirculating gas which moves with velocity $u_b - U_{mf}$, relative to the emulsion phase.

Fig. 7-1 depicts the gas flow patterns around a bubble rising upwards in the fluidized bed with a velocity u_b, through the emulsion phase. According to Davidson's bubble model [71], the rising bubbles push aside the particles which behave like an incompressible inviscid fluid, and the velocity of the particles is therefore negligible compared to u_b. Moreover, the recirculating gas flows with a velocity $\sim U_{mf} \ll u_b$ relative to the quasi-static emulsion, so we estimate the gas flow velocity in the cloud to be $u_b - U_{mf} \simeq u_b$. In the measurement of the bubble-emulsion exchange, the initial xenon magnetization in both the emulsion and adsorption phases was zero, so the recirculating gas continuously encountered the emulsion and adsorption phases with no hyperpolarization. As a result, the ratio of decrease in magnetization of gas reentering the bubble is estimated to be

$$e^{-\frac{d_b}{u_b \tau}} \simeq 0, \tag{7.1}$$

where d_b is the bubble diameter and τ is the exchange time between the interstitial gas and adsorption phase, being on the order of 1 ms. The approximation was based on the condition of the typical bubble diameter of 2 mm and the corresponding u_b of 10 cm/s. To summarize, the reentering gas has zero polarization and the exchange between the cloud and the emulsion phase outside the cloud is fast enough so that the cloud layer places no impedance on the bubble-emulsion exchange. It is therefore justified to use the bubble-cloud exchange rate k_{bc} to approximate the exchange rate between the bubble and emulsion phases.

Fig. 7-2 shows the predicted time-dependence of spin magnetization within the bubble phase with and without adsorption of gas on the particles. In the case of no adsorption, the recirculation of hyperpolarized gas results in a later increment of the bubble magnetization [83]. On the other hand, the increment is not expected in the case of strong adsorption. The experimental results shown in Fig. 6-17 clearly confirm that the recirculation of polarized gas is not observable in our experiments so we are justified to treat the clouds and the emulsion as a single phase.

147
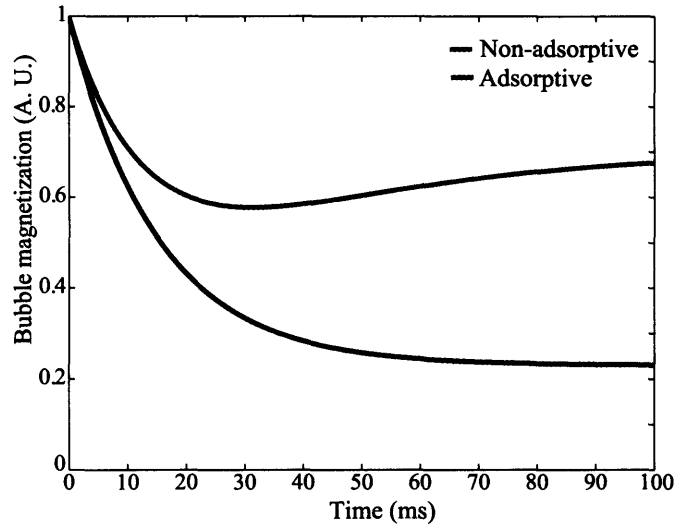
Figure 7-2: The expected bubble-emulsion exchange curve corresponding to the presence or absence of adsorption.

7.1.2 Bubble-Emulsion Exchange Much Slower than Emulsion-Adsorption Exchange

We assumed that the bubble-emulsion exchange (where cloud is grouped with emulsion) is much slower than the emulsion-adsorption exchange, as expressed in Inequality (5.22). Fig. 7-3 shows the measured values of $k_{be}(1 + \frac{\psi_b}{\psi_e + \psi_a})$.

The average value of $k_{ea}(1 + \frac{\psi_e}{\psi_a})$ was calculated to be 1001.8 s^{-1}, very close to the estimated value based on molecule diffusion in the interstitial space under the adsorptive chemical potential. When the gas flow rate was about 50 sccm, $k_{be}(1 + \frac{\psi_b}{\psi_e})$ was less than 100 s^{-1}, an order slower than $k_{ea}(1 + \frac{\psi_e}{\psi_a})$. At lower gas flow rates, the ratio between the two rates ranges from 4.7 to 7.1, which is less significant. The simplification of the model by assuming an infinitive exchange rate between the emulsion and adsorption may result in some systematic error at the low gas flow rates. The actual bubble-emulsion exchange rate is given by Eqn. (5.10), which is smaller than the value predicted from Davidson's equation (5.8) which only accounts for the bubble-cloud exchange. The experimental results in Fig. 6-18 confirm this observation and show that the measured bubble-emulsion exchange rates are smaller
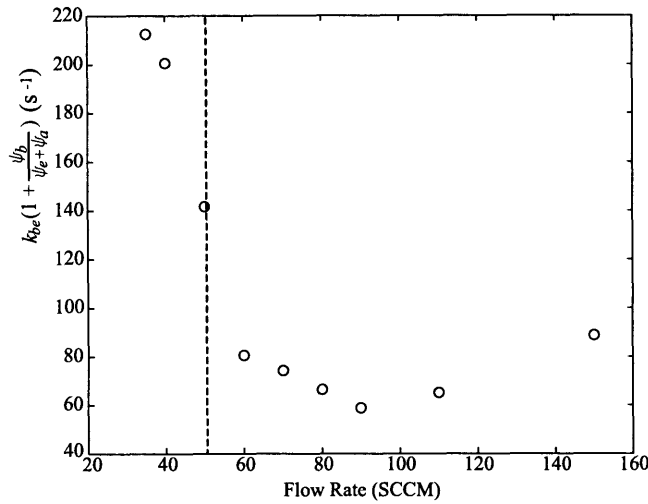
Figure 7-3: $k_{be}\left(1 + \frac{\psi_b}{\psi_e+\psi_a}\right)$ measured corresponding to two exchange behaviors.

than the prediction.

In conclusion, our assumption is generally correct since the observed emulsion-adsorption exchange is more than an order of magnitude faster than the bubble-emulsion exchange in vigorous bubbling regime. At lower gas flow rates, the assumption still roughly applies with the ratio between the two rates being larger than 4.7 for experiment.

7.1.3 Removing Effects of Inflow and Outflow of Spin Magnetization

The inflow and outflow terms in Eqn. (5.14) have been removed in the implementation of the experiments. We now justify this procedure with the actual experimental data.

Inflow of Bubbles

The effect of incoming freshly polarized xenon in the form of bubbles was eliminated by phase-cycling the acquisition pulse sequence, as described in the last chapter. The performance of the sequence is demonstrated in Fig. 7-4 where two groups of data are included: one with and the other without the phase-cycling.

149

a) With phase-cycling   50 sccm

Bubble Magnetization (A. U.)

Delay Time (ms)

b) Without phase-cycling   50 sccm

Bubble Magnetization (A. U.)

Delay Time (ms)
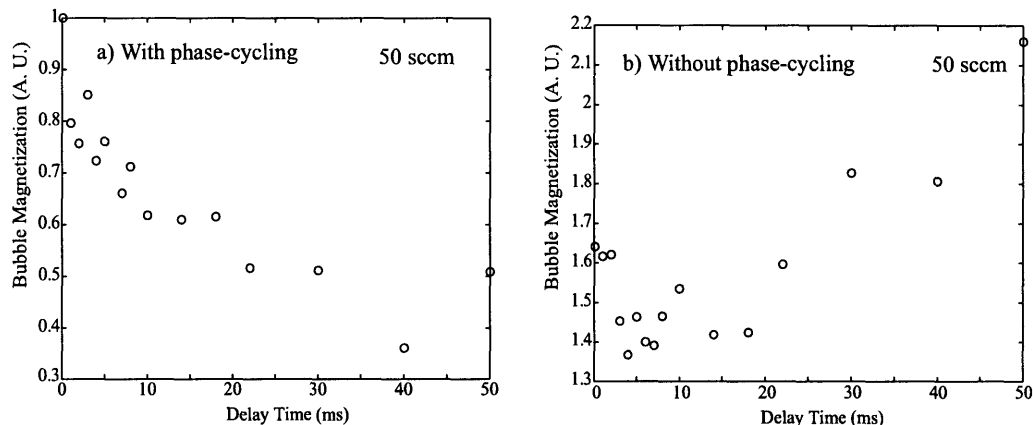
Figure 7-4: The effectiveness of phase-cycling in removing the incoming bubble magnetization during exchange time τ_2. a) The time-dependence of the bubble magnetization at 50 sccm measured with the phase-cycling. b) Same measurement made at 50 sccm without phase-cycling.

In the data measured with the phase-cycling technique, the bubble magnetization decayed following an exponential curve, from which exchange time was extracted corresponding to the flow rate of 50 sccm. However, without phase-cycling, steady increment in spin magnetization was found following an initial decay by a small amount, demonstrating the effect of incoming freshly polarized bubbles. We conclude that this measurement scheme effectively suppressed the effect of the inflow gas on the exchange measurement.

Outflow of bubbles

In order to remove the effect of the bubble outflow, we applied 64 dummy scans with 75 ms delay time before each scan, so that only a partial region of the coil was filled with polarized gas. We estimated in the last chapter that no bubbles were able to escape the bed during the exchange time τ_2, which was less than 100 ms. However, a broad distribution of bubble velocity existed, in which a certain amount of bubbles traversed the bed with higher than the mean velocity. As a consequence, we observed an abrupt decrease in the bubble magnetization at the flow rate of 100 ms, as shown in Fig. 7-5. We carefully identified this artifact in the spectrum before carrying
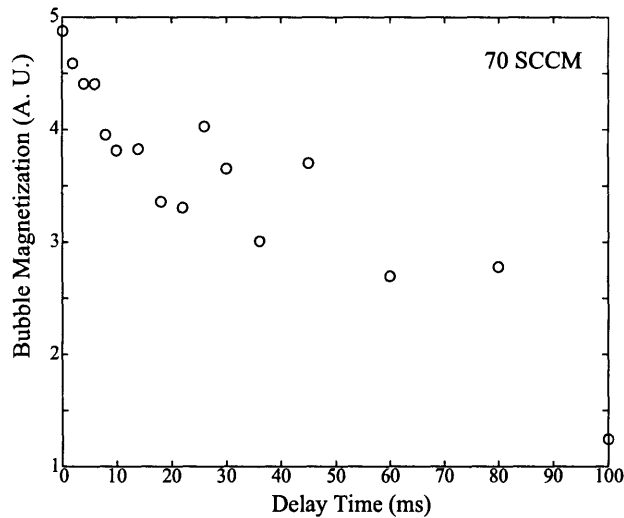
Figure 7-5: The effect of the outflow of bubbles exiting the bed from the top. A sudden decrease in bubble magnetization was found at a delay time of 100 ms.

out data analysis by using delay times before the occurrence of the bubble outflow, signalled by a sudden decrease in the bubble magnetization.

7.1.4 Expansion in the Emulsion Phase

Since the aluminum oxide particles we used in the experiments belong to Geldard Group B, we assumed that the volume expansion of the emulsion phase was negligible compared to that due to bubbles. This assumption needs to be verified since emulsion expansion will result in a systematic error in the estimated bubble diameter based on the bed expansion data, which was considered to be solely from the bed volume holdup by bubbles. Moveover, the two-phase flow model described in Section 6.4 will need modification since the void fraction, as well as the gas flow velocity in the emulsion phase was assumed to be constant for the range of gas flow rates used in the measurement.

The measured ratio ψ_e/ψ_a shown in Fig. 6-15 demonstrates that the gas fraction in the emulsion phase remains constant as the flow rate was increased. This result justifies the assumption.

Table 7.1: Time Scales in the Fluidized Bed

Process	Time scale
Bubble flow through the coil region	240 ms
Emulsion gas flow through the coil region	4.8 s
T_1 relaxation in bubbles	> 10 min
T_1 relaxation in the emulsion	> 10 s
Duration for measuring the bubble-emulsion exchange	100 ms
Duration for measuring the emulsion-adsorption exchange	10 ms
Bubble-cloud exchange through coherent flow	60 ms (Eqn. 5.8)
Bubble-cloud exchange through diffusion	15 ms (Eqn. 5.8)
Overall bubble-cloud exchange	12 ms
Cloud-emulsion exchange through gas adsorption	1 ms
Cloud-emulsion exchange through diffusion	10 ms (Eqn. 5.9)
Overall cloud-emulsion exchange	1 ms
Emulsion-adsorption exchange	1 ms

7.2 Different Time Scales in the Exchange Processes

Table 7.1 summarizes the time-scales of various processes studied in our fluidized-bed experiments.

The exchange rates between the different phases can be easily compared based on this table. It also includes the durations of different NMR measurements, as well as the lifetimes of the phases in the coil region. Note that during the bubble-emulsion measurement, which is on the order of 100 ms, the coherent flow ($\sim$ 60 ms) through a bubble only experiences 1 - 2 recirculations, in agreement with the fact that it is dominated by the diffusive exchange.

7.3 Conclusion

We have demonstrated the capability of NMR technology in measuring gas exchange rates among the three different phases in gas-fluidized granular media. The result of this measurement has significance in industrial fluidized-bed applications since the particles chosen were representative of many categories of catalyst particles. The

152

contrasting values of transverse spin relaxation time in the bubble and dense phases allowed us to differentiate the phases effectively by using NMR T_2-weighted RF pulse sequences. The results of the bubble-emulsion exchange measurement were in agreement with predictions made based on existing models and bed expansion data available from phenomenological observation. We also measured the emulsion-adsorption exchange rate with a simple NMR method, yielding results that are not available elsewhere.

In contrast to other methods, our polarized gas NMR technique is able to probe deep into 3D fluidized beds non-invasively. For a bed without ferromagnetic particles, all the physical and chemical properties will be intact if probed with NMR technology in the presence of the strong magnetic field. Moreover, we performed measurements on natural bubbles generated at the bottom of the bed, instead of artificial bubbles from gas injection, which not only eliminated the efforts of building the injection apparatus but represented the real phenomenon occurring in typical industrial fluidized beds. Another advantage of our method is that we are able to probe bubbles with diameters of a few millimeters, while other methods only work on much larger bubbles on the order of centimeters, limited by the bubble-detection technology. This work therefore verifies that Davidson's exchange model also applies to small bubbles where bubble-emulsion exchange is fast. In addition, our approach is capable of measuring the exchange rate between the emulsion and multiple bubbles, providing the capability of studying the effects of bubble coalescence and splitting on the exchange rate. Our results are in good agreement with the prediction based on the single-bubble model, which implies that the interaction between multiple bubbles does not significantly affect the bubble-emulsion exchange, at least for the parameter space we have studied.

Another significance of our method is that it is based on observation of the spatial integration of spin magnetization, which is sensitive to the total laser-polarized gas in bubbles. Hence we do not need to assume a homogeneous tracer concentration in the bubbles, as in earlier methods where tracer concentration only at a single point in a bubble was detectable. Additionally, our measurement is not affected by changes in bubble diameter, based on the experimental technique to limit the exchange time

τ_2 so that no bubbles escape the detection region during the measurement.

Our method may be applied to fluidized beds with various categories of powders, with a large range of particle sizes operable in the bubbling regime. The key requirement is the availability of sufficient magnetic susceptibility contrast between the solid and gas phases, which is easy to achieve for irregular powders. The aluminum oxide powders used in our measurement have a moderate value of magnetic susceptibility, compared to other types of solid materials. However, spherical particles are not good candidates for such a study since distribution of the interstitial magnetic field is significantly narrowed and T_2 contrast is not available. This is usually not an issue since almost all natural powders are irregularly shaped. The second limitation of this method is that it is not capable of probing the inter-phase exchanges in a bed with particles of the following categories: metals, paramagnetic substances, or ferromagnetic materials. Metals tend to interfere with the RF radiation and detection. Xenon T_1 in the presence of paramagnetic materials is significantly shortened, resulting in an extremely poor SNR. Ferromagnetic materials are not able to fluidize in a high magnetic field due to the presence of strong magnetic forces.

We also measured the velocity distribution of gas flow through particle interstitial spaces. Results from this measurement reveal interesting gas and particle behaviors that clearly show the transition from homogeneous to bubbling fluidization. It has also been confirmed that particles are statically suspended in homogeneous fluidization and the vigorous movement of particles starts only when the bubbles appear.

7.4 Future Studies

The measurement of mass exchange rates between the different phases may be easily extended onto particles of different types and sizes, belonging to either Geldart Group A or B. We plan to continue this work by testing the method on more particle samples. A bed of Geldart A particles, when fluidized, demonstrates significant amount of expansion in the emulsion phase. It is hence difficult to determine the average bubble size by measuring the bed expansion, and to predict the exchange rate as a function

of the gas flow rate, as demonstrated in this thesis. However, the contrast mechanism and exchange measurement are not affected and will work with both Geldart A and B particles.

Potential studies also include investigation of gas flow dynamics in the homogeneous fluidization regime, where debates exist regarding whether or not the particles are completely suspended by the fluidizing gas and behave like a fluid. Our current unique experimental set-up will allow us to attack this problem by looking at gas flow instead of particle motions. Pulsed field gradient NMR may be used to probe the coherent and dispersive motions of the gas phase. It may be possible to verify the two particle motion regimes, observed by Valverde *et al.* [63] for homogeneous fluidization, because the removal of inter-particle stresses implies stronger drag forces from the gas, possibly resulting in observable changes in gas flow at the transition. This measurement will provide experimental evidence aiding understanding of particle and gas behavior in homogeneously fluidized granular media.

Appendix A

Fluidized Bed Design

The assembly for gas-fluidized bed design consists of four different pars: windbox, diffuser plate flange, mounting flange and gas exhaust flange, as shown in the following pages.
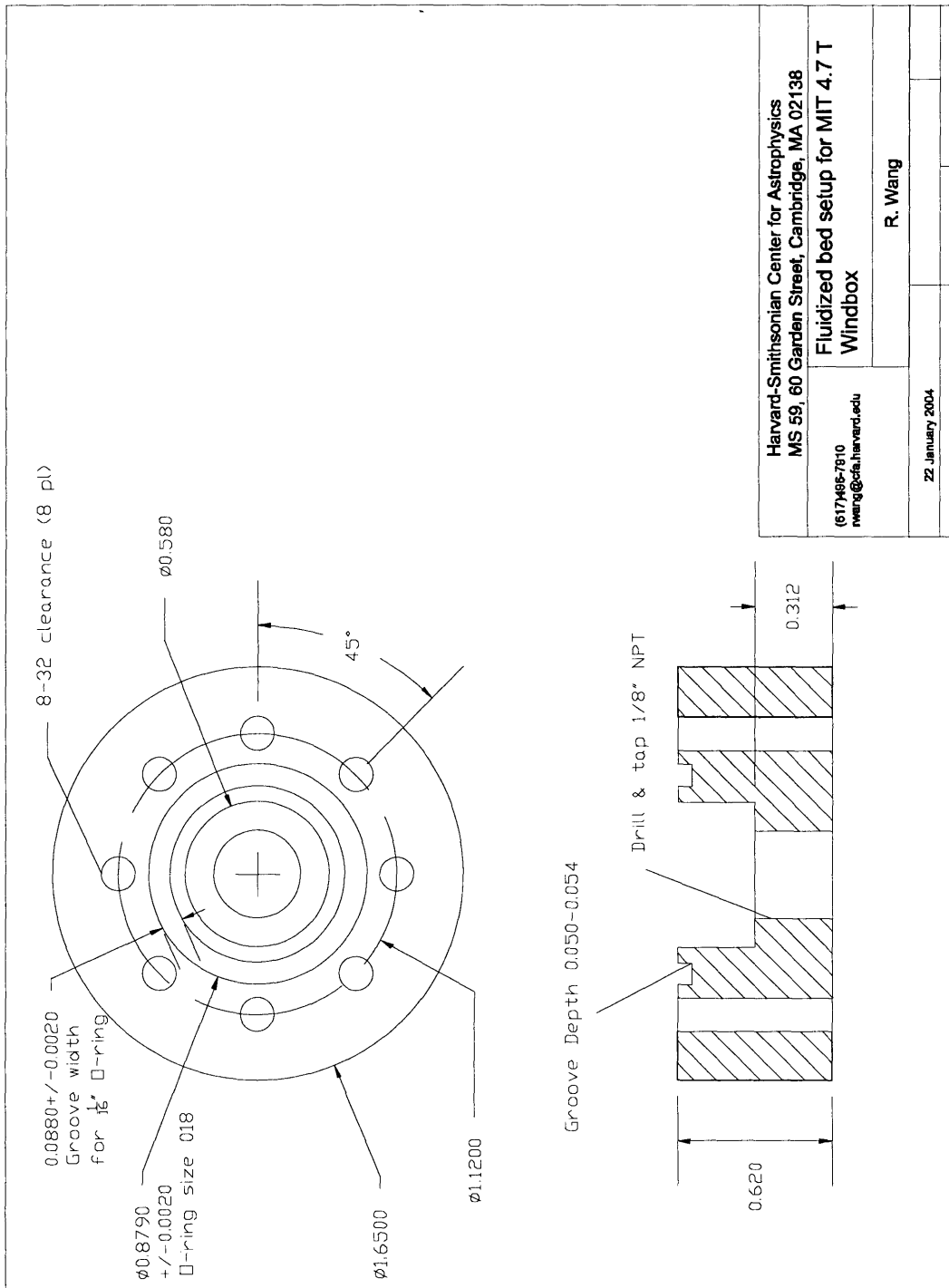
Figure A-1: Fluidized bed windbox design.
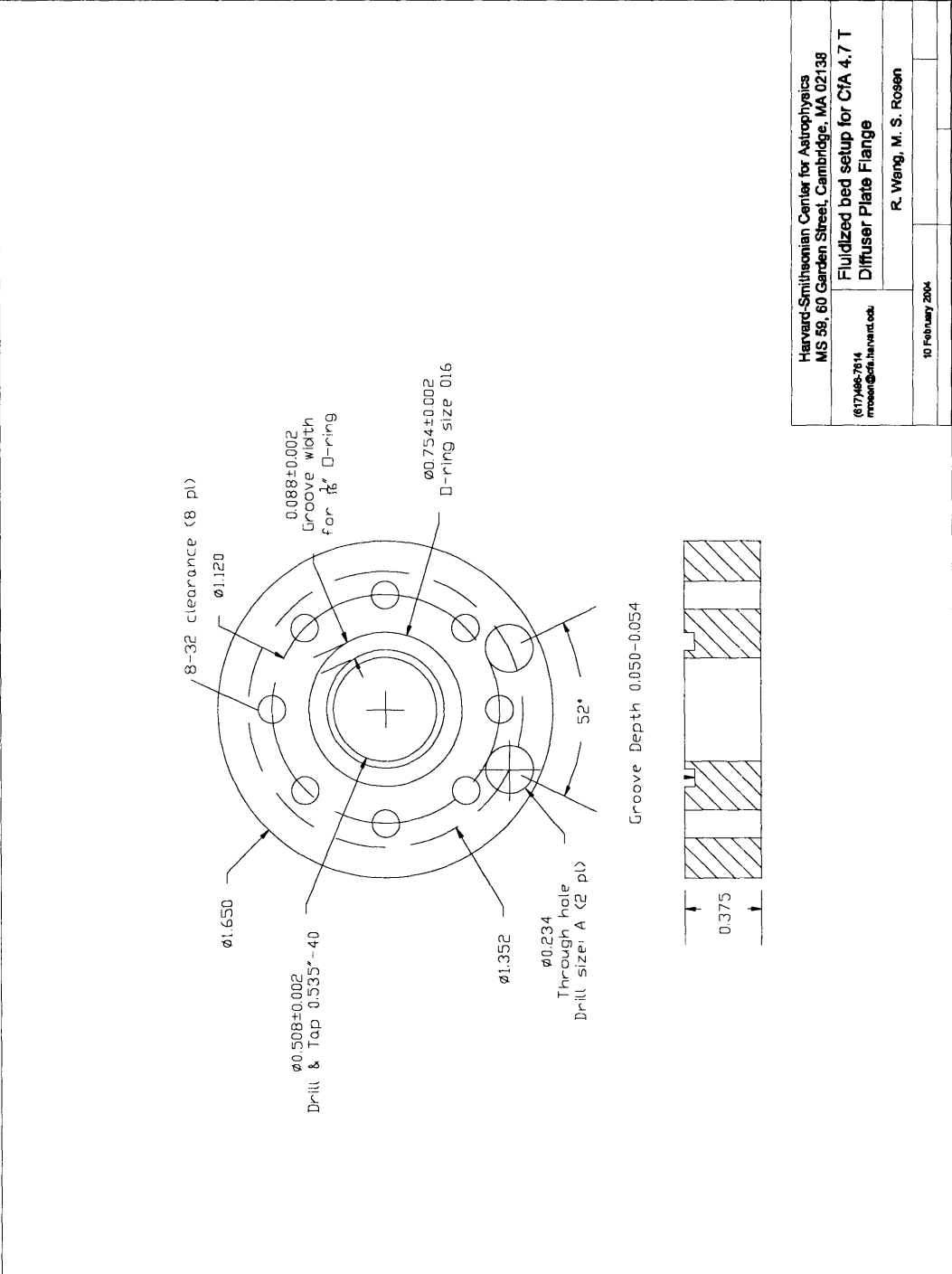
Figure A-2: Fluidized bed bottom diffuser plate flange design.
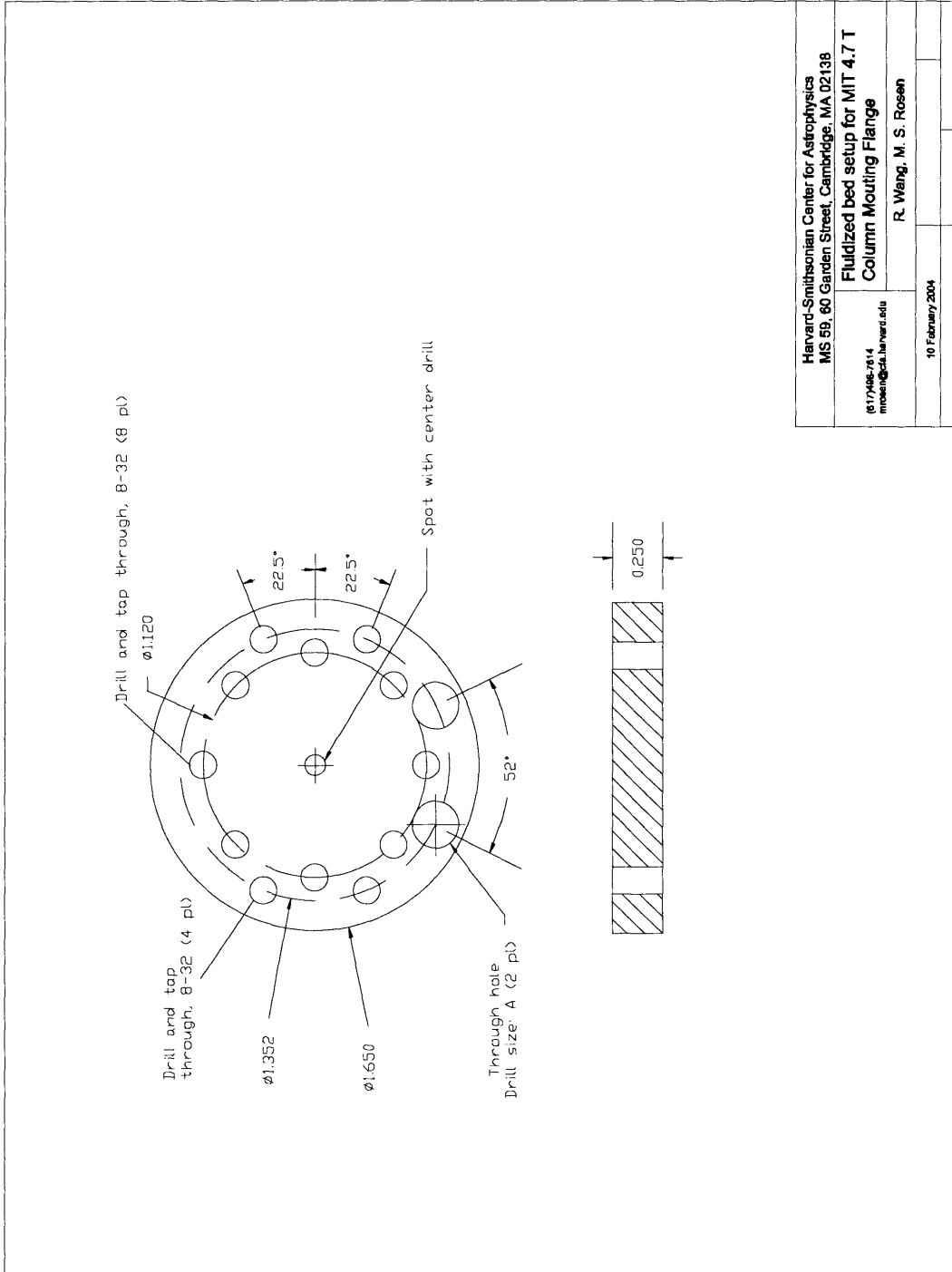
Figure A-3: Fluidized bed column mounting flange design.
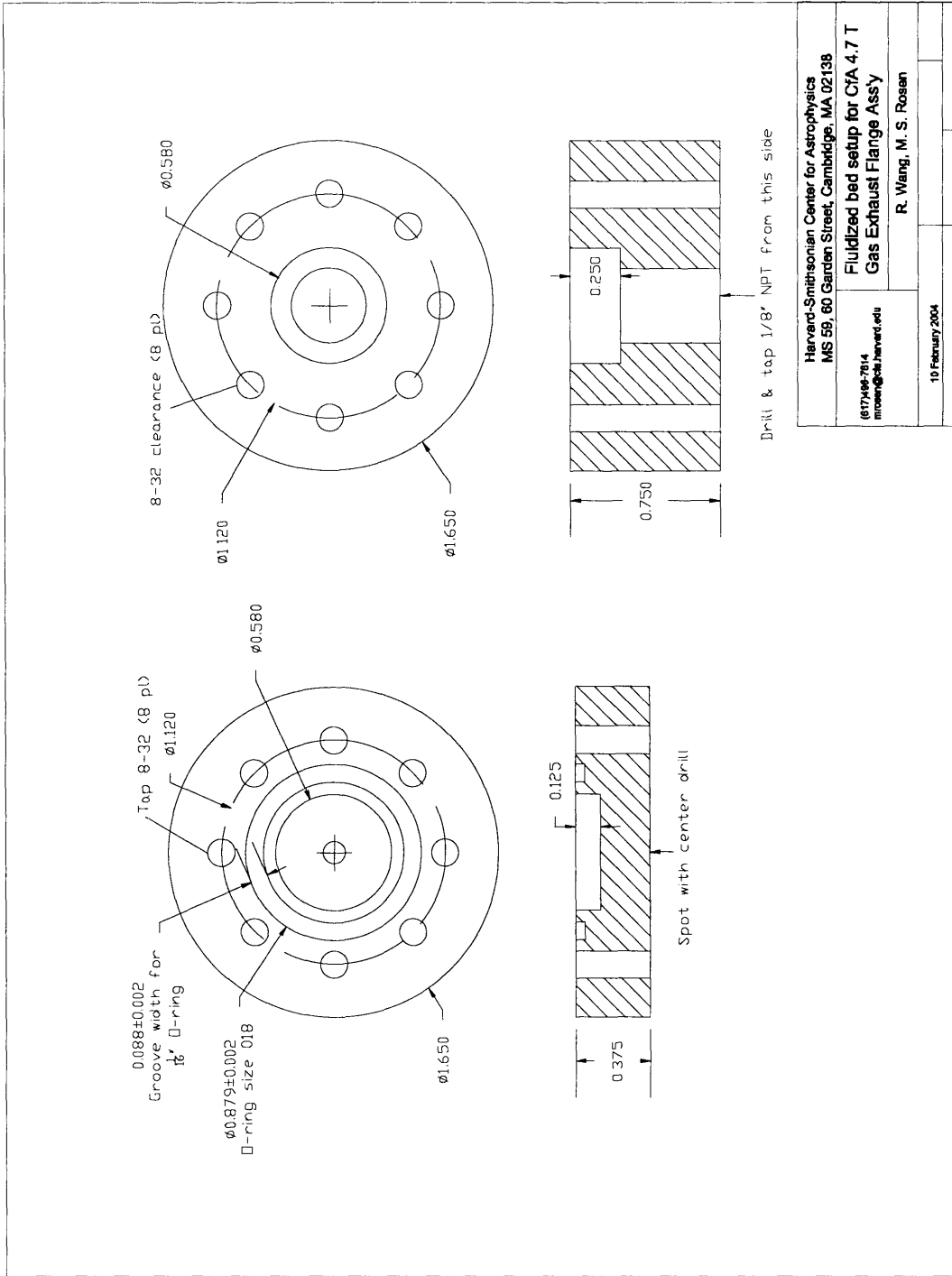
Figure A-4: Fluidized bed gas exhaust flange design.

Appendix B

Fluidization Apparatus for a Horizontal-Bore Magnet
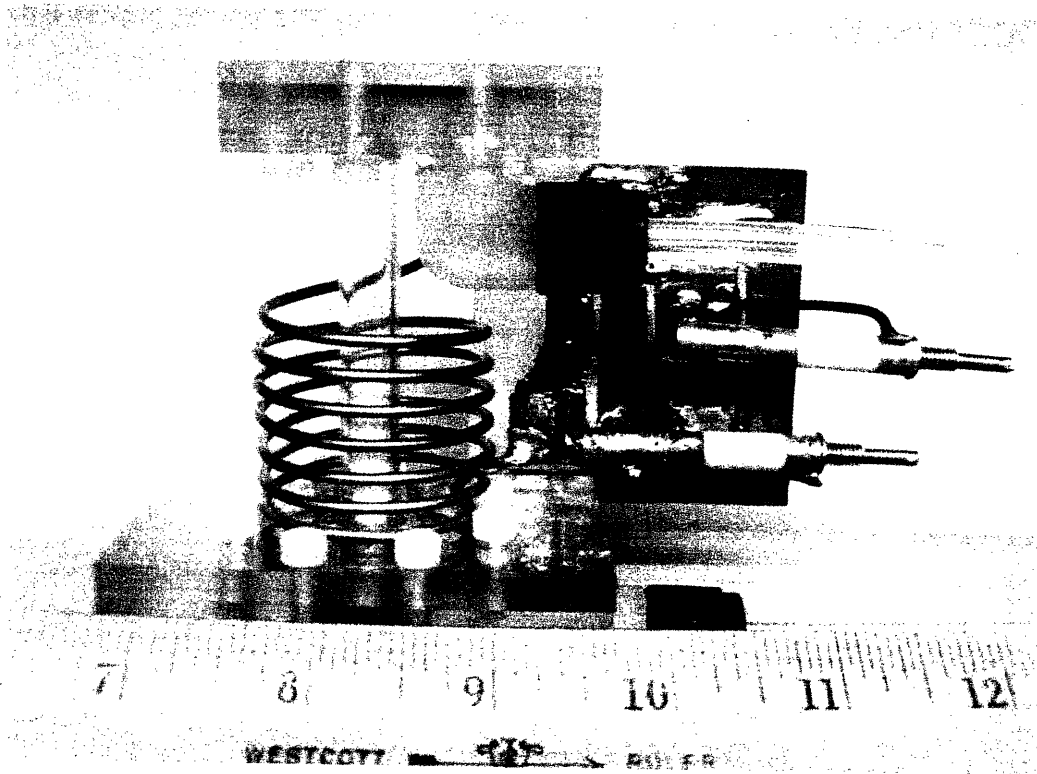
Figure B-1: A Second Fluidization Apparatus.

Appendix C

Parameters Characterizing Fluidized Beds

Table C.1: Fluidized-Bed Parameters

Variable	Description
V	Volume of the whole bed ($V = V_e + V_b + V_s$)
V_e	Volume of the emulsion phase
V_b	Volume of the bubble phase
V_a	Volume of the adsorption phase
V_s	Volume of the solid phase, $V_s > V_a$
ϵ	Void fraction of the whole bed
ϵ_e	Void fraction in emulsion (void volume divided by emulsion volume)
ϵ_{mf}	Void fraction of the emulsion phase corresponding to minimum fluidization
ψ_e	Ratio of void space volume in emulsion to the whole bed volume, $\psi_e = \frac{V_e}{V}\epsilon_e$
ψ_b	Ratio of bubble volume to the whole bed volume, $\psi_b = \frac{V_b}{V}$
ψ_a	Ratio of adsorption volume to the whole bed volume, $\psi_a = \frac{V_a}{V}$
q	Volumetric gas flow rate
U	Superficial gas flow velocity
U_{mf}	Superficial gas flow velocity corresponding to minimum fluidization
U_{mb}	Superficial gas flow velocity corresponding to minimum bubbling
u_e	Gas flow velocity in the emulsion phase
u_b	Bubble rising velocity

Appendix D

Phase-Cycling in Measurement of the Bubble-Emulsion Exchange

In order to remove the effect of inflow gas on the measurement of the bubble-emulsion exchange rate, we applied phase-cycling on the first 90° RF pulse and receiver phase, as shown in Table D.1. The pulse sequence is shown here again for ease to read.

Two different phase sequences were used in the measurement. Their effects on both the exchanged and inflow magnetizations are shown under the lines of the corresponding phase sequences, in terms of magnetization orientations. The acquired data had the same phase after the two scans for exchanged magnetization, while 180° difference in the inflow magnetizations. Summation of the two group of data yielded coherent addition of exchanged magnetization while the inflow term was cancelled.
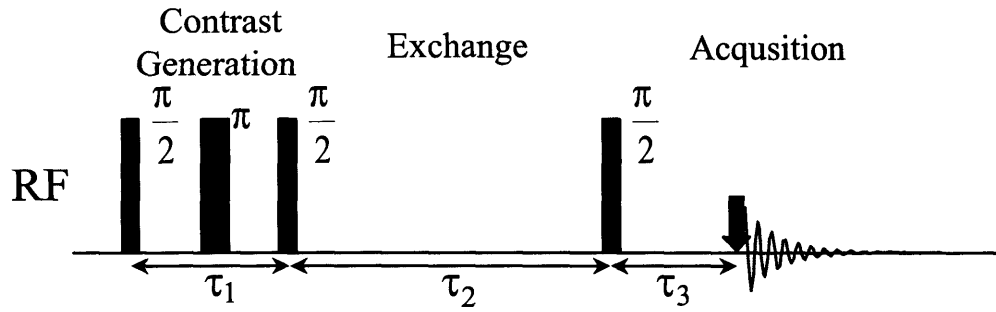
Figure D-1: The pulse sequence.

Table D.1: Phase-Cycling in the Sequence

Sequence	$\frac{\pi}{2}$	π	$\frac{\pi}{2}$	$\frac{\pi}{2}$	Receiver
Phase	0	0	0	0	0
Exchange Magn.	+Y	-Y	+Z	+Y	+Y
Inflow Magn.	N/A	N/A	N/A	+Y	+Y
Phase	2	0	0	0	2
Exchange Magn.	-Y	+Y	-Z	-Y	+Y
Inflow Magn.	N/A	N/A	N/A	+Y	-Y

Appendix E

List of Rules Used in Error Analysis

E.1 Error Propagation

Suppose y is a function of n variables labelled by x_i $(i = 1, \cdots, n)$ as

$$y = f(x_1, x_2, \cdots, x_n). \tag{E.1}$$

If we designate the standard deviations in x_i values by σ_i and assume x_i's are independent of each other, the standard deviation in y is then given by

$$\Delta y = \sqrt{\sum_{i=1}^{n} \sigma_i^2 \left(\frac{\partial f}{\partial x_i}\right)^2}. \tag{E.2}$$

This is the representation of the error propagation.

E.2 Error Analysis in Least-Square Linear Fittings

Suppose we have two data vectors:

$$X = (x_1, x_2, \cdots, x_n) \text{ and } Y = (y_1, y_2, \cdots, y_n), \tag{E.3}$$

we want to fit them to a linear relationship given by

$$y = ax + b, \tag{E.4}$$

where a and b are fitting parameters to be determined. The principle is to find a and b that minimize the so-defined Chi-square:

$$\chi = \sum_{i=1}^{n} \frac{[y_i - (ax_i + b)]^2}{\sigma_i^2}, \tag{E.5}$$

where σ_i is the standard deviation of y_i. According to Bevington [53], we have the following fitting results

$$
\begin{aligned}
a &= \Delta \left[\sum_{i=1}^{n} \frac{x_i^2}{\sigma_i^2} \sum_{i=1}^{n} \frac{y_i}{\sigma_i^2} - \sum_{i=1}^{n} \frac{x_i}{\sigma_i^2} \sum_{i=1}^{n} \frac{x_i y_i}{\sigma_i^2} \right] \text{ and} \\
b &= \Delta \left[\sum_{i=1}^{n} \frac{1}{\sigma_i^2} \sum_{i=1}^{n} \frac{x_i y_i}{\sigma_i^2} - \sum_{i=1}^{n} \frac{x_i}{\sigma_i^2} \sum_{i=1}^{n} \frac{y_i}{\sigma_i^2} \right],
\end{aligned} \tag{E.6}
$$

where

$$\Delta = \sum_{i=1}^{n} \frac{1}{\sigma_i^2} \sum_{i=1}^{n} \frac{x_i^2}{\sigma_i^2} - \left(\sum_{i=1}^{n} \frac{x_i}{\sigma_i^2} \right)^2. \tag{E.7}$$

The standard deviation of the fitting results a and b are

$$
\begin{aligned}
\sigma_a &= \frac{1}{\Delta} \sum_{i=1}^{n} \frac{x_i^2}{\sigma_i^2} \text{ and} \\
\sigma_b &= \frac{1}{\Delta} \sum_{i=1}^{n} \frac{1}{\sigma_i^2}.
\end{aligned} \tag{E.8}
$$

The goodness of the linear fitting is evaluated by the correlation coefficient defined by

$$R^2 = \frac{\left[\sum_{i=1}^{n} (x_i - \bar{x})(y_i - \bar{y}) \right]^2}{\sum_{i=1}^{n} (x_i - \bar{x})^2 \sum_{i=1}^{n} (y_i - \bar{y})^2}. \tag{E.9}$$

When the value of R^2 is larger than 0.9, a linear relationship is considered to exist between the two vectors.

If the data are to be fitted to any function, instead of a line, the function needs to be reorganized into linear dependence so that the above formulations can be used. These formula have been used in analyzing the experimental results in this thesis.

Bibliography

[1] D. Kunii. *Fluidization Engineering*. Butterworth-Heinemann, 1991.

[2] R. Jackson. *The Dynamics of Fluidized Particles*. Cambridge University Press, 2000.

[3] A. Kastler. Quelques questions concernant la production optique du ingalit du population des niveaux de qualification spatiale des atomes. Application a l'exprience de Stern et Gerlach et la resonance magnetique. *J. Phys. Radium*, 11, 1950.

[4] S. Suzuki, T. Akahori, N. Miyazawa, M. Numata, T. Okubo, and J. P. Butler. Alveolar surface area-to-lung volume ratio in oleic acid-induced pulmonary edema. *J. Appl. Physiol*, 80, 1996.

[5] A. Seidel, F. Rittner, and B. Boddenberg. ^{129}Xe NMR Chemical Shifts and Linewidths of Xenon in Zeolites ZnY. *J. chem. Soc. Faraday Trans*, 92(493), 1996.

[6] K. Sperling-Ischinsky and W.S. Veeman. ^{129}Xe-NMR of Carbon Black Filled Elastomers. *J. Braz. Chem. Soc*, 10(4), 1999.

[7] K W Miller, N V Reo, A J Schoot Uiterkamp, D P Stengle, T R Stengle, and K L Williamson. Xenon NMR: chemical shifts of a general anesthetic in common solvents, proteins, and membranes. *Proc. Natl. Acad. Sci*, 78(8), 1981.

[8] N. Kato, T. Ueda, H. Omi, K. Miyakubo, and Taro Eguchi. Characterization of adsorbed xenon in Zeolite-A, X, and Y by high-pressure ^{129}Xe NMR spectroscopy. *Phys. Chem. Chem. Phys*, 6(23), 2004.

[9] D. J. Griffiths. *Introduction to Electrodynamics.* Prentice Hall, Inc, 1989.

[10] C. P. Slichter. *Principles of Magnetic Resonance.* Harper & Row, 1963.

[11] F. Bloch. Nuclear Induction. *Phys. Rev*, 70, 1946.

[12] E. L. Hahn. Nuclear Induction Due to Free Larmor Precession. *Phys. Rev*, 77, 1950.

[13] A. Abragam. *Principles of Nuclear Magnetism.* Oxford University Press, 1961.

[14] A. Bifone, Y.-Q. Song, R. Seydoux, R. E. Taylor, B. M. Goodson, T. Pietrass, T. F. Budinger, G. Navon, and A. Pines. NMR of laser-polarized xenon in human blood. *Proc Natl Acad Sci U S A*, 93(23), 1996.

[15] R. W. Mair, C.-H. Tseng, D. G. Cory G. P. Wong, and R. L. Walsworth. Magnetic Resonance Imaging of Convection in Laser-Polarized Xenon. *Phys. Rev. E*, 61, 2000.

[16] B. Audoly, P. N. Sen, S. Ryu, and Y. Q. Song. Correlation functions for inhomogeneous magnetic field in random media with application to a dense random pack of spheres. *J. Magn. Reson*, 164(1), 2003.

[17] A. Fick. *Ann. Physik, Leipzig*, 170, 1855.

[18] P. T. Callaghan. *Principles of Nuclear Magnetic Resonance Microscopy.* Oxford University Press, 1995.

[19] E. O. Stejskal and J. E. Tanner. Spin Diffusion Measurements: Spin Echoes in the Presence of a Time-Dependent Field Gradient. *J. Chem. Phys.*, 42, 1965.

[20] G. P. Wong, C.-H. Tseng, V. R. Pomeroy, R. W. Mair, D. P. Hinton, D. Hoffmann, R. E. Stoner, F. W. Hersman, D. G. Cory, and R. L. Walsworth. A

system for low field imaging of laser-polarized noble gas. *Journal of Magnetic Resonance*, 141, 1998.

[21] R. W. Mair, C.-H. Tseng, G. P. Wong, D. G. Cory, and R. L. Walsworth. Magnetic Resonance Imaging of Convection in Laser-Polarized Xenon. *Phys. Rev. E*, 61, 2000.

[22] K. W. Miller, N. V. Reo, A. J. Uiterkamp, D. P. Stengle, T. R. Stengle, , and K. L. Williamson. Xenon NMR: Chemical Shifts of a General Anesthetic in Common Solvents, Proteins, and Membranes. *Proc Natl Acad Sci U S A*, 78(8), 1981.

[23] P. T. Callaghan, A. Coy, D. MacGowan, K. J. Packer, and F. O. Zelya. Diffraction-Like Effects in NMR Diffusion Studies of Fluids in Porous Solids. *Nature*, 351, 1991.

[24] P. P. Mitra, P. N. Sen, and L. M. Schwartz. Short-Time Behavior of the Diffusion Coefficient as a Geometrical Probe of Porous Media. *Phys. Rev. B*, 47, 1993.

[25] R. W. Mair and R. L. Walsworth. Novel MRI Applications of Laser-Polarized Noble Gases. *Appl. Magn. Reson*, 22, 2002.

[26] W. Happer. Optical Pumping. *Rev. Mod. Phys*, 44(2), 1972.

[27] S. Aplett, A. B. Baranga, and C. J. Erickson et al. Theory of spin-exchange optical pumping of ^{3}He and ^{129}Xe. *Phys. Rev. A*, 58(2), 1998.

[28] A. Oros and N. Shah. Hyperpolarized xenon in NMR and MRI. *Phys. Med. Biol*, 49, 2004.

[29] M. S. Rosen. Laser Polarized Xe-129 Magnetic Resonance Spectroscopy and Imaging; the Development of a Method for in vivo Perfusion Measurement. *Thesis*, 2001.

[30] M. A. Bouchiat, J. Brossel, and L. C. Pottier. Evidence for Rb-rare-gas molecules from the relaxation of polarized Rb atoms in a rare gas. Experimental Results. *J. Chem. Phys*, 56, 1972.

[31] G. D. Cates, R. J. Fitzgerald, and A. S. Barton et al. Rb-^{129}Xe spin-exchange rates due to binary and three-body collisions at high Xe pressures. *Phys. Rev. A*, 45, 1992.

[32] G. P. Wong. Nuclear Magnetic Resonance Experiments Using Laser-Polarized Noble Gas. *Thesis*, 2001.

[33] A. G. Richter, C. J. Yu, A. Datta, J. Kmetko, and P. Dutta. In situ and interrupted growth studies of the self-assembly of octadecyltrichlorosilane monlayers. *Phys. Rev. E*, 61, 2000.

[34] B. Driehuys, G. D. Cates, and W. Happer. Surface Relaxation Mechanisms of Laser-Polarized ^{129}Xe. *Phys. Rev. Lett.*, 74:4943–4946, 1995.

[35] N. Bloembergen, E. M. Purcell, and R. V. Pound. Relaxation effects in nuclear magnetic resonance absorption. *Phys. Rev*, 73, 1948.

[36] J. Bear. *Dynamics of Fluids in Porous Media*. Elsevier Inc., New York, 1972.

[37] S. Whitaker. A Theoretical Derivation of Darcy's Law. *Transport Porous Med.*, 1, 1986.

[38] R. Meyer and F. F. Krause. Experimental Evidence for Permeability Minima at Low-Velocity Gas Flow Through Naturally Formed Porous Media. *J. Porous Med.*, 1, 1998.

[39] M. D. Hrlimann, K. G. Helmer, L. L. Latour, and C. H. Sotak. Restricted Diffusion in Sedimentary Rocks. Determination of Surface-Area-to-Volume Ratio and Surface Relaxivity. *J. Magn. Reson. Series A*, 111, 1994.

176

[40] D. B. Stephens, K.-C. Hsu, M. A. Prieksat, M. D. Ankeny, N. Blandford, T. L. Roth, J. A. Kelsey, and J. R. Whitworth. A Comparison of Estimated and Calculated Effective Porosity. *Hydrogeol. J*, 6, 1998.

[41] P. Z. Wong. *Dynamics of Fluids in Porous Media*. Academic Press, London, 1999.

[42] M. Sahimi. Flow phenomena in rocks: from continuum models to fractals, percolation, cellular automata, and simulated annealing. *Rev. Mod. Phys*, 65, 1993.

[43] D. P. Ours, D. I. Siegel, and P. H. Glaser. Chemical dilation and the dual porosity of humidified peat bog. *J. Hydrol*, 196, 1997.

[44] T. G. Walker and W. Happer. Spin-exchange optical pumping of noble-gas nuclei. *Rev. Mod. Phys*, 69:629–642, 1997.

[45] J. P. Butler, R. W. Mair, D. Hoffmann, M. I. Hrovat, R. A. Rogers, G. P. Topulos, R. L. Walsworth, and S. Patz. Measuring Surface-Area-to-Volume Ratios in Soft Porous Materials using Laser-Polarized Xenon Interphase Exchange Nuclear Magnetic Resonance. *Phys. Rev. E*, 14, 2002.

[46] Y.-Q. Song. Determining Pore Sizes Using an Internal Magnetic Field. *J. Magn. Reson*, 143, 2000.

[47] M. S. Rosen, T. E. Chupp, K. P. Coulter, R. C. Welsh, and S. D. Swanson. Polarized Xe-129 optical pumping/spin exchange and delivery system for magnetic resonance spectroscopy and imaging studies. *Rev. Sci. Instrum*, 70, 1999.

[48] H. Y. Carr and E. M. Purcell. Effects of Diffusion on Free Precession in Nuclear Magnetic Resonance Experiments. *Phys. Rev*, 94, 1954.

[49] H. Huang, K. Wang, D. M. Bodily, and V. J. Hucka. Density Measurements of Argonne Premium Coal Samples. *Energ. Fuel*, 9, 1996.

[50] M. Bencsik and C. Ramanathan. Method for measuring local hydraulic permeability using magnetic resonance imaging. *Phys. Rev. E*, 63(065302), 2001.

[51] R. E. Jacob, S.W. Morgan, and B. Saam. Wall Relaxation of ^{3}He in Spin-Exchange Cells. *Phys. Rev. E*, 87(143004), 2001.

[52] R. W. Fox and A. T. McDonald. *Introduction to Fluid Mechanics*. John Wiley & Sons Inc., New York, 1998.

[53] P. R. Bevington and D. K. Robinson. *Data Reduction and Error Analysis for The Physical Sciences*. McGraw-Hill Science, 1991.

[54] C.-H. Tseng, G. P. Wong, V. R. Pomeroy, R. W. Mair, D. P. Hinton, D. Hoffmann, R. E. Stoner, F. W. Hersman, D. G. Cory, and R. L. Walsworth. Low-Field MRI of Laser Polarized Noble Gas. *Phys. Rev. Lett*, 81, 1998.

[55] M. J. Nicholl, H. Rajaram, and R. J. Glass. Factors controlling satiated relative permeability in a partially-saturated horizontal fracture. *Geophys. Res. Lett*, 27, 2000.

[56] M. Jamiolahmady, A. Danesh, D. H. Tehrani, and D. B. Duncan. Positive effect of flow velocity on gas-condensate relative permeability: Network modeling and comparison with experimental results. *Transport Porous Med*, 52, 2003.

[57] R. M. Nedderman. *Statics and Kinematics of Granular Materials*. Cambridge University Press, 1992.

[58] B. J. Ennis, J. Green, and R. Davies. The legacy of neglect in the U.S. *Chem. Eng. Prog*, 90:32–43, 1994.

[59] J. Z. Xue, E. Herbolzheimer, M. A. Rutgers, W. B. Russel, and P. M. Chaikin. Diffusion, Dispersion, and Settling of Hard Spheres. *Phys. Rev. Lett*, 69(11), 1992.

[60] K. Rietema. The effect of interparticle forces on the expansion of a homogeneous gas-fluidised bed. *Chem. Eng. Sci*, 28, 1973.

[61] S. C. Tsinontides and R. Jackson. The mechanics of gas fluidized beds with an interval of stable fluidization. *J. Fluid Mech*, 255, 1993.

[62] N. Menon and D. J. Durian. Particle Motions in a Gas-Fluidized Bed of Sand. *Phys. Rev. Lett*, 79(18), 1997.

[63] J. M. Valverde, A. Castellanos, and M. A. Quintanilla. Self-Diffusion in a Gas-Fluidized Bed of Fine Powder. *Phys. Rev. Lett*, 86(14), 2001.

[64] P. U. Foscolo and L. G. Gibilaro. A fully predictive criterion for the transition between particulate and aggregate fluidization. *Chem. Eng. Sci*, 39, 1984.

[65] D. Geldart. *Gas Fluidization Technology*. John Wiley & Sons Ltd, 1986.

[66] D. Geldart. Types of gas fluidization. *Powder Technol*, 7, 1978.

[67] P.C. Carman. Fluid flow through a granular bed. *Trans. Inst. Chem. Eng*, 15, 1937.

[68] C. Y. Wen and Y. H. Yu. A generalized method for predicting the minimum fluidization velocity. *AIChE J*, 21, 1966.

[69] D. Geldart and A. R. Abrahamsen. *Powder Technol*, 19, 1978.

[70] R. M. Davies and G. I. Taylor. The mechanics of large bubbles rising through extended liquids and through liquids in tubes. *Proc. Roy. Soc. London Ser. A*, 200, 1950.

[71] J. F. Davidson and D. Harrison. *Fluidized Particles*. Cambridge University Press, 1963.

[72] J. F. Davidson, D. Harrison, and J. R. F. Guedes de Carvalho. On the Liquidlike Behavior of Fluidized Beds. *Ann. Rev. Fluid Mech*, 9, 1977.

[73] R. R. Cranfield and D. Geldart. Large particle fluidisation. *Chem. Eng. Sci*, 29(4), 1974.

[74] A. Bifone, T. Pietrass, J. Kritzenberger, and A. Pines. Surface Study of Supported Metal Particles by ^{129}Xe NMR. *Phys. Rev. Lett*, 74(16), 1995.

[75] A. Gedeon, J. L. Bonardet, T. Ito, and J. Fraissard. Application of ^{129}Xe NMR to the Study of Ni^{2+} Y Zeolites. *J. Phys. Chem*, 93, 1989.

[76] I. L. Moudrakovski, A. Nossov, S. Lang, S. R. Breeze, C. I. Ratcliffe, B. Simard, G. Santyr, and J. A. Ripmeester. Continuous Flow NMR with Hyperpolarized Xenon for the Characterization of Materials and Processes. *Chem. of Materials*, 12(5), 2000.

[77] M. Mansfeld and W. S. Veeman. ^{129}Xe Nuclear Magnetic Resonance of Al_2O_3 fibers. *Microporous Materials*, 3, 1994.

[78] R. Higbie. The rate of adsorption of a pure gas into a still liquid during short periods of exposure. *Trans. Am. Inst. Chem. Eng*, 31, 1935.

[79] L. Davies and J. F. Richardson. Gas interchange between bubbles and the continuous phase in a fluidized bed. *Trans. Inst. Chem. Eng*, 44, 1966.

[80] G. K. Stephens, R. J. Sinclair, and O. E. Potter. Gas exchange between bubbles and dense phase in a fluidised bed. *Powder Technol*, 1, 1967.

[81] T. Chiba and H. Kobayashi. Gas exchange between the bubble and emulsion phases in gas-solid fluidized beds. *Chem. Eng. Sci*, 25, 1970.

[82] J. R. Grace. *Recent Advances in the Engineering Analysis of Chemcially Reacting Systems*. Wiley, New Delhi, 1984.

[83] D. J. Patil, M. S. Annaland, and J.A.M. Kuipers. Gas Dispersion and Bubble-to-Emulsion Phase Mass Exchange in a Gas-Solid Bubbling Fluidized Bed: A Computational and Experimental Study. *Int. J. of Chem. Reactor Eng*, 1(44), 2003.

[84] C. Chavarie and J. R. Grace. Interphase mass transfer in a gas-fluidized bed. *Chem. Eng. Sci*, 31, 1975.

[85] S. P. Sit and J. R. Grace. Interphase mass transfer in an aggregative fluidized bed. *Chem. Eng. Sci*, 33, 1977.

[86] W. E. Resnick and R. R. White. Mass transfer in systems of gas and fluidized solids. *Chem. Eng. Prog*, 45, 1949.

[87] K. N. Kettenring, E. L. Manderfield, and J. M. Smith. *Chem. Eng. Prog*, 46, 1950.

[88] J. C. Chu, J. Kalil, and W. A. Wetteroth. Mass transfer in a fluidized bed. *Chem. Eng. Prog*, 49, 1953.

[89] T. Kai, T. Imamura, and T. Takahashi. Hydrodynamic influences on mass transfer between bubble and emulsion phases in a fine particle fluidized bed. *Powder Technol*, 83, 1994.

[90] P. W. Percival and J. S. Hyde. Saturation-recovery measurements of the spin-lattice relaxation times of some nitroxides in solution. *J. Magn. Reson*, 23, 1976.

[91] R. Savelsberg, D. E. Demco, B. Blumich, and S. Stapf. Particle motion in gas-fluidized granular systems by pulsed-field gradient nuclear magnetic resonance. *Phys. Rev. E*, 65(020301), 2002.

[92] E. E. Ehrichs, H. M. Jaeger, G. S. Karczmar, Y. V. Kuperman J. B. Knight, and S. R. Nagel. Granular Convection Observed by Magnetic Resonance Imaging. *Science*, 267, 1995.

[93] R. W. Mair, M. S. Rosen, R. Wang, D. G. Cory, and R. L. Walsworth. Diffusion NMR Methods Applied to Xenon Gas for Materials Study. *Magn. Reson. Chem*, 40, 2002.

[94] R. W. Mair, R. Wang, M.S. Rosen, D. Candela, D.G. Cory, and R.L. Walsworth. Applications of Controlled-Flow Laser-Polarized Xenon Gas to Porous and Granular Media Study. *Magn. Reson. Imag*, 21, 2003.

[95] D. W. Alderman and D. M. Grant. An efficient decoupler coil design which reducesheating in conductive samples in superconducting spectrometers. *J. Magn. Reson*, 36, 1979.

[96] R. Ojha, N. Menon, and D. J. Durian. Hysteresis and packing in gas-fluidized beds. *Phys. Rev. E*, 62(3), 2000.

[97] S. C. Saxena and G. J. Vogel. The measurement of incipient fluidization velocities in a bed of coarse dolomite at temperature and pressure. *Trans. Inst. Chem. Eng*, 55(3), 1977.

[98] D. C. Chitester, R. M. Kornosky, L. Fan, and J. P. Danko. Characteristics of fluidization at high pressure. *Chem. Eng. Sci*, 39(2), 1984.

[99] X. Yang, C. Huan, D. Candela, R. W. Mair, and R. L. Walsworth. Measurements of Grain Motion in a Dense, Three Dimensional Granular Fluid. *Phys. Rev. Lett*, 88(044301), 2000.

[100] J. C. Orcutt, J. F. Davidson, and R. L. Pigford. Reaction time distributions in fluidized catalytic reactors. *Chem. Eng. Prog. Sym. Ser*, 58(387), 1962.